UNIVERSITY OF SOUTHAMPTON

FACULTY OF ENGINEERING AND THE ENVIRONMENT

Materials and Surface Engineering

Enhancing light absorption in silicon solar cells by fluorescent molecules

by

Liping Fang

Thesis for the degree of Doctor of Philosophy

August 2014

UNIVERSITY OF SOUTHAMPTON

ABSTRACT

FACULTY OF ENGINEERING AND THE ENVIRONMENT

Photovoltaics

Thesis for the degree of Doctor of Philosophy

Enhancing light absorption in silicon solar cells by fluorescent molecules

Liping Fang

This project aims to harness photon transport in planar solar converters via fluorescent molecules to enhance light absorption in silicon and hence reduce the material requirements and the cost of crystalline silicon solar cells. To accomplish this aim two approaches has been investigated: concentrating the far field radiation of the excited fluorescent molecules on a small area of silicon solar cell by using a fluorescent solar collector; directly injecting the excitonic energy of the excited fluorescent molecules to the waveguide modes in a proximal thin crystalline silicon solar cell via near field interactions.

An analytical model has been developed to characterise photon reabsorption in fluorescent solar collectors. This model is able to predict the spectrum of the incident photon flux on the optically coupled edge solar cell, which is not easy to measure experimentally. In the limit of high reabsorption, a useful simple expression has been found for the reabsorption probability limit, which only depends on the étendue of the photon flux emitted at the edge of the collector, the absorption coefficient of the dye molecule, and the refractive index of the collector matrix.

Perceiving the solar cell as a waveguide, the highly oscillating behaviour of the quantum efficiency of a 200 nm thick crystalline silicon solar cell has been linked to the waveguide modes supported by the thin solar cell, by studying the analytical properties of the solar cell absorbance in the complex plain of the wavenumber of light.

Efficient energy injection into a 25 nm thick thin crystalline silicon film has been demonstrated by studying molecular fluorescence and energy transfer of a carbocyanine dye deposited as Langmuir-Blodgett monolayers at different distance to the surface of copper, bulk crystalline silicon and 25 nm thick crystalline silicon films. Via the time correlated single photon counting technique, the dependence of fluorescence lifetime on the distance to the 25 nm thick crystalline silicon films has been found to fit quantitatively with an analytical expression for the injection rate of waveguide modes or simply the photon tunnelling rate from an excited molecule to a nearby thin waveguide obtained by a complex variable analysis.

Table of Contents

List of Figures

List of Figures

List of Tables

Declaration of Authorship

I, Liping Fang, declare that the thesis entitled “Enhancing light absorption in silicon solar cells by fluorescent molecules” and the work presented in the thesis are both my own, and have been generated by me as the result of my own original research. I confirm that:

- this work was done wholly or mainly while in candidature for a research degree at this University;
- where any part of this thesis has previously been submitted for a degree or any other qualification at this University or any other institution, this has been clearly stated;
- where I have consulted the published work of others, this is always clearly attributed;
- where I have quoted from the work of others, the source is always given. With the exception of such quotations, this thesis is entirely my own work;
- I have acknowledged all main sources of help;
- where the thesis is based on work done by myself jointly with others, I have made clear exactly what was done by others and what I have contributed myself;
- parts of this work have been published and these publications are listed in the following page.

Signed: ……..

Date:……

List of Publications

[1] **L. Fang**, T. S. Parel, L. Danos, and T. Markvart, "Modelling the performance of fluorescent solar collectors," in *Proceedings of the 7th Photovoltaic Science Application and Technology Conference*, pp.165-168, Heriot-Watt University, Edinburgh, UK, 2011.

[2] T. S. Parel, **L. Fang**, X. Chu, L. Danos, and T. Markvart, "Comparison of fluorescent down-shifting layers for increasing the efficiency of CdS/CdTe solar cells," in *Proceedings of the 7th Photovoltaic Science Application and Technology Conference*, pp.87-90, Heriot-Watt University, Edinburgh, UK, 2011.

[3] T. Markvart, L. Danos, **L. Fang**, T. S. Parel, and N. Soleimani, "Photon frequency management for trapping & concentration of sunlight," *RSC Advances*, vol. 2, no. 8, pp.3173-3179, 2012.

[4] **L. Fang**, T. S. Parel, L. Danos, and T. Markvart, "Photon reabsorption in fluorescent solar collectors," *Journal of Applied Physics*, vol. 111, no. 7, pp.076104-3, 2012.

[5] T. Markvart, L. Danos, N. Alderman, **L. Fang**, and T. Parel, "Harvesting sunshine: solar cells, photosynthesis and the thermodynamics of light," in *Proceedings of the 27th European Photovoltaic Solar Energy Conference*, Frankfurt, Germany, 2012.

[6] **L. Fang**, L. Danos, T. Markvart, "Solar cell as a waveguide: quantum efficiency of an ultrathin crystalline silicon solar," in *Proceedings of the 28th European Photovoltaic Solar Energy Conference*, Paris, France, 2013.

[7] T. Markvart, N. Alderman, L. Danos, **L. Fang**, T. Parel, "Enhancing light capture by silicon - with the help of molecules," in *Proceedings of the 40th IEEE Photovoltaic Specialists Conference*, Denver, Colorado, 2014.

[8] L. Danos, N. Alderman, **L. Fang**, T. Markvart, "Silicon sensitization using light harvesting layers," in *Proceedings of the 10th Photovoltaic Science Application and Technology Conference*, Loughborough University, Loughborough, UK, 2014.

[9] T. Parel, L. Danos, **L. Fang**, T. Markvart, "Modelling photon transport in fluorescent solar concentrators", accepted by *Progress in Photovoltaics: Research and Applications*, 2014.

Acknowledgements

First I would like to thank my main supervisor Professor Tom Markvart for his invaluable guidance through my PhD studies. It is him who leads me into the field of solar energy, it is him who broadens my horizon of knowledge, and it is him who always inspires me to carry on. Then I would like to thank my second supervisor Dr Liudi Jiang for her precious guidance and suggestions.

I wish to thank Dr Lefteris Danos, who taught me to conduct experiments from scratch. Also great thanks to the other members of Solar Energy Laboratory: Thomas S. Parel, Dr Nicolas Alderman, Dr Adib Ibrahim, Dr Nazila Soleimani, Dr Thomas J.J. Meyer and Dr Robert Greef, for their kind help and precious discussions regarding my work and life.

I would like to thank Dr Kian S. Kiang, Dr Owain Clark and Dr Jim Farmer for their help with using the facilities at Southampton Nanofabrication Centre, Dr Nick Hardy of Biolin Scientific for his advice on Langmuir-Blodgettry, Dr Peter Wright of Sartorius for his help with the DI water system, Professor Jiafu Lin of Beijing Institute Technology for his suggestions on numerical simulations, Mr Le Zhong for his help with sputtering, Miss Binyan He for her help with microscope and Professor Philippa Reed, Emma, Sue, Jackie, Sasha, Pavittar, Dave, Rob, Eric, Chris, Alistair, Keith and Carl for their administrative and technical support.

I would also like to thank all my friends at Southampton for their kind help and sharing happiness and sorrow with me.

I acknowledge the financial support from the University of Southampton and China Scholarship Council.

Finally, I would like to thank my families, especially my dear wife, for their endless love and support.

Nomenclature

A	Absorbance of light	-
B	Brightness of light	W/(m^2·sr)
b	Fluorescence damping rate	s^{-1}
c	Speed of light	m/s
D_e	Diffusion constant of electrons	m^2/s
D_h	Diffusion constant of holes	m^2/s
$\mathbf{E}$	Electric field vector	V/m
E	Electric field amplitude	V/m
F	Force applied on the balance	N
E_c	Lower conduction band edge energy of silicon	eV
E_v	Higher valence band edge energy of silicon	eV
F_s	Generation rate of electron-hole pairs	s^{-1}
F_c	Recombination rate of electron-hole pairs	s^{-1}
f_ω	Geometric factor	-
G	Generation function of electron-hole pairs	s^{-1}
g	Gravitational constant	m/s^2
H	Thickness of solar cell	µm
h	Planck constant	J·s
I	Current	A
I_l	Current generated by light	A
I_o	Dark saturation current of diode	A
I_{sc}	Short-circuit current	A
i	Unit imaginary number	-
J	Current density	A/m^2
$\mathbf{k}$	Wavenumber vector	m^{-1}
k	Wavenumber	m^{-1}
k_B	Boltzmann constant	J·K^{-1}
k_x	Wavenumber component in the x direction	m^{-1}
k_ρ	In-plane wavenumber	m^{-1}
k_{rad}	Radiative fluorescence decay rate	s^{-1}

Nomenclature

k_{nr}	Non-radiative fluorescence decay rate	s^{-1}
L	Length of fluorescent solar collector	m
m	Mode index number	-
n	Refractive index	-
$\dot{N}$	Photon flux	s^{-1}
N^*	Number of molecules in excited state	-
N_f	Number of fluorescent photons	-
N_A	Dopant concentration in p-type semiconductor	m^{-3}
N_D	Dopant concentration in n-type semiconductor	m^{-3}
N_c	Density of states in conduction band	m^{-3}
N_v	Density of states in valence band	m^{-3}
P	Fraction of fluorescent photons emitted in surface escape cone	-
Q_c	Collection efficiency of fluorescent photons	-
q	Charge of an electron; fluorescence quantum yield	C; -
R	Reflectance of light	-
R_S	Radius of Sun	m
R_{SE}	Distance of Sun and Earth	m
$\mathbf{r}$	Position vector	-
r	Reabsorption probability	-
$\mathbf{r_s}$	Position vector of dipole	-
r_p	Fresnel reflection coefficient of TM wave	-
r_s	Fresnel reflection coefficient of TE wave	-
S_e	Surface recombination velocity of electrons	$cm \cdot s^{-1}$
S_h	Surface recombination velocity of holes	$cm \cdot s^{-1}$
T	Transmittance of light	-
T_c	Temperature of solar cell	K
T_S	Temperature of Sun	K
t	Time	s
t_p	Fresnel transmission coefficient of TM wave	-
t_s	Fresnel transmission coefficient of TE wave	-
U_e	Recombination rate of electrons	s^{-1}

U_h	Recombination rate of holes	s^{-1}
u	Normalised in-plane wavenumber	-
V	Voltage; volume	V; m^3
V_{oc}	Open-circuit voltage	V
W	Width of solar cell depletion region	μm
x	Position scalar in cylindrical coordinates	-
X	Position scalar in cylindrical coordinates	-
α	Absorption coefficient	m^{-1}
γ	Surface tension	mN/m
ε	Permittivity of silicon	F/m
η	Efficiency	-
θ	Propagation angle of light	degree
θ_c	Critical angle for total internal reflection	degree
κ	Extinction coefficient of silicon	-
λ	Wavelength of light	nm
μ	Chemical potential of light	eV
μ_e	Chemical potential of electrons	eV
μ_h	Chemical potential of holes	eV
ν	Frequency of light	s^{-1}
$\mathscr{E}$	Étendue of light	$sr \cdot m^2$
Π	Surface pressure	mN/m
$\boldsymbol{\rho}$	Position vector in cylindrical coordinates	-
$\boldsymbol{\rho}_s$	Position vector of dipole in cylindrical coordinates	-
ρ	Position scalar in cylindrical coordinates	-
τ_e	Recombination lifetime of electrons	s
τ_h	Recombination lifetime of holes	s
τ_f	Fluorescence lifetime	s
τ_{rad}	Radiative fluorescence lifetime	s
τ_{nr}	Non-radiative fluorescence lifetime	s
ϕ	Photon flux	s^{-1}
ϕ_f	Fluorescence quantum yield	-
Ω	Solid angle	sr

Nomenclature

ω	Frequency of light	rad·s^{-1}
φ	Built-in potential of solar cell	eV

List of Abbreviations

Ag	Silver
Al	Aluminium
AM	Air Mass
Au	Gold
ARC	Anti-Reflection Coating
CdS/Se/Te	Cadmium Sulphide/ Selenide/ Telluride
CPS	Chance, Prock, Silbey
Cr	Chromium
DCM	4-Dicyanomethylene-2-Methyl-6-(P(Dimethylamino)Styryl)-4H-Pyran
DI	De-ionised
DiI	1,1'-Dioctadecyl-3,3,3',3'-Tetramethylindocarbocyanine Perchlorate
Dy	Dysprosium
EEC	Edge Escape Cone
ET	Energy Transfer
EQE	External Quantum Efficiency
Eu	Europium
FF	Fill Factor
FSC	Fluorescent Solar Collector/Concentrator
GaAs	Gallium Arsenide
Gd	Gadolinium
HED	Horizontal Electric Dipole
HMDS	Hexamethyldisilazane
Ho	Holmium
IQE	Internal Quantum Efficiency
LB	Langmuir-Blodgett
LED	Light Emitting Diode
LiF	Lithium Fluoride
lsw	lossy surface waves
Mn	Manganese
Nd	Neodymium
NIR	Near Infrared

List of Abbreviations

nm	nanometre
NP	Nano-Particle
NREL	National Renewable Energy Laboratory
PbS	Lead Sulphide
PECVD	Plasma Enhanced Chemical Vapour Deposition
(P)MMA	(Poly) Methyl Methacrylate
pt	photon tunnelling
PVC	Polyvinyl chloride
SA	Stearic Acid
sp	surface plasmons
Si	Silicon
SiO_2	Silicon Dioxide
Sm	Samarium
SNC	Southampton Nanofabrication Centre
SOI	Silicon On Insulator
STP	Standard Temperature and Pressure
S&Q	Shockley and Queisser
Tb	Terbium
TCSPC	Time Correlated Single Photon Counting
TE	Transverse Electric
TIR	Total Internal Reflection
TM	Transverse Magnetic
T&F	Trivich and Flinn
UO_2	Uranium Dioxide
UV	Ultraviolet
VAT	Value Added Tax
VASE	Variable Angle Spectroscopic Ellipsometry
VED	Vertical Electric Dipole
wg	waveguide
W&L	Weber and Lambe
Yb	Ytterbium

Chapter 1 Research Overview

1.1 Background

Climate concerns and dwindling fossil fuel resources are driving an increasing demand for renewable energy solutions, with solar energy arguably the cleanest and safest method of power generation. Around the globe, increasing number of businesses and homeowners are harnessing the power of sunlight, the earth's most abundant natural resource, to provide energy. Further progress, however, is hampered by either low efficiency or high cost of solar cells.

Currently, bulk crystalline silicon solar cell technology dominates the commercial market. However, in order to achieve efficient operation, such silicon solar cells need a few hundreds of micrometres thick of crystalline silicon material. This is due to the indirect bandgap nature of the silicon material, which renders it weak to absorb solar radiation. To significantly reduce silicon consumption while maintain the high efficiency of the solar cells, sunlight needs to be trapped in silicon to enhance its absorption. In this thesis, we show that fluorescent molecules can be used to harness sunlight in planar solar converts to enhance light absorption in silicon solar cells and hence reduce the use of semiconductor materials and the cost of crystalline silicon solar cells.

Dielectric waveguides are planar structures that can trap photons inside via Total Internal Reflection (TIR). By doping fluorescent dye molecules inside the waveguide, the incident solar radiation can be coupled to the trapped waveguide modes and concentrated to the waveguide edge without tracking the sun. A small area solar cell can be mounted to the waveguide edge to form a Fluorescent Solar Concentrator/Collector (FSC). The initial proposed structure of FSC [1] is shown in Fig. 1.1, where the remained three edges and the bottom surface are covered by mirrors.

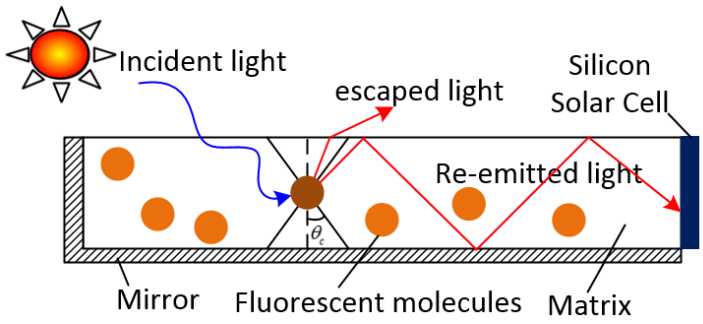

Figure 1.1: Cross-sectional view of a typical FSC.

Recent advances demonstrate that FSCs offer much potential to enhance the performance of solar cells [2]–[4]. The combination of solar cells with fluorescent photonic structures in

particularly bears the promise of reducing the amount of semiconductor by an order of magnitude or more [5]. Although the theoretical power conversion efficiency of a silicon solar cell with a FSC is believed to reach 90% of the maximum efficiency of an ideal silicon solar cell given by the Shockley and Queisser detailed balance limit [6], the practical efficiencies are significantly lower due to the lack of suitable dyes and several loss mechanisms of photon transport. The performance of FSCs still needs further study and improvements.

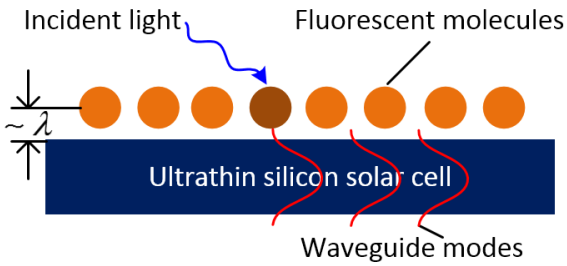

Figure 1.2: Photon tunnelling into an ultrathin silicon solar cell.

In FSCs the far field radiation of excited fluorescent molecules are coupled to the waveguide modes in the planar dielectric matrix. In this work we show that waveguide modes can also be injected to a thin planar silicon solar cell by proximal (distance in the order of light wavelength) excited fluorescent molecules via interactions in the near field. The working principle of such a process is shown in Fig. 1.2. The excited fluorescent molecules, which work as electric dipoles, can inject its excitonic energy to the underlying silicon solar cell as trapped modes via the evanescent waves of the dipole radiation.

This energy transfer process can be viewed as photon tunnelling through the same potential barrier which confines photons inside the high refractive index material by TIR [7] and it is analogous to photon tunnelling through an air gap between two prisms at an incident angle greater than the critical angle for TIR which was observed more than a century ago [8]. In the system shown in Fig. 1.2, we have simply replaced the exciting prism by fluorescent molecules. Preliminary theoretical calculation shows that the photon tunnelling probability can exceed 80% for a silicon film which is merely 34 nm thick [9], [10]. Thus this system bears substantial potential for photovoltaic applications.

1.2 Aims and objectives

This work aims to harness photon transport in planar solar converters via fluorescent molecules to enhance light absorption in silicon and hence reduce the material requirements and the cost of crystalline silicon solar cells. To accomplish this aim the following objectives have been pursued:

(1) Fabrication and characterisation of FSC samples doped with organic fluorescent dyes;

(2) Development of an analytical model to study photon transport and characterise photon reabsorption loss in FSCs;

(3) Development of an analytical model to study the quantum efficiency of a 200 nm thick crystalline silicon solar cell;

(4) Development of an analytical expression to quantify photon tunnelling from an excited fluorescent molecule to a proximal thin layer;

(5) Experimental investigation of molecular fluorescence and energy transfer near copper, bulk crystalline silicon and 25 nm thick crystalline silicon films via the Langmuir-Blodgett and time correlated single photon counting techniques.

1.3 Report outline

Chapter 1 gives the overview of this research project.

Chapter 2 reviews the basic concepts of light propagation in planar layered structures.

Chapter 3 reviews the basic knowledge of solar radiation, molecule fluorescence and the working principle as well as the efficiency limits of idealised crystalline silicon solar cells.

Chapter 4 is the literature review of FSCs, which comprises the recent development of materials and novel structures to enhance their performance.

Chapter 5 derives an analytical model to characterise photon reabsorption in FSCs. The details for fabrication and characterisation of FSC samples are given and the experimental measured results are compared with the modelling results.

Chapter 6 develops an analytical model to study the quantum efficiency of a 200 nm thick crystalline silicon solar cell by perceiving the solar cell as a waveguide.

Chapter 7 reviews fluorescence and energy transfer near metal and semiconducting interfaces and their application to the enhancement of solar cell performance.

Chapter 8 develops an analytical expression to quantify photon tunnelling from an excited fluorescent molecule to a thin layer which support a limited number of waveguide modes.

Chapter 9 summarises the experimental procedures and results of studying fluorescence and energy transfer near glass, metal, bulk crystalline silicon and 25 nm thick crystalline silicon films via the techniques of Langmuir-Blodgettry, variable angle spectroscopic ellipsometry and time-correlated single photon counting.

Chapter 10 concludes the whole work and suggests future work.

Chapter 2 Optical Waves in Layered Media

2.1 Introduction

Layered structures play an important role in many modern optical devices such as solar cells and fluorescent solar collectors. To design and optimise these devices, we need to understand light propagation inside these devices. This chapter reviews reflection, transmission and absorption of optical waves in layered structures. The bases of (frustrated) total internal reflection, evanescent waves, dipole emission, and optical modes such as Fabry-Perot and waveguide modes in layered structures are also reviewed.

2.2 Transverse waves and Fresnel coefficients

The material constitutes the layered structures in this chapter is limited to source free, homogeneous, isotropic and non-magnetic materials. The solution of Maxwell equations governing the electric and magnetic fields of the electromagnetic waves can be given by the monochromatic planar waves, the electric field of which is given by [11]

$$\mathbf{E} = \mathbf{E}_0 \exp\left[i\left(\mathbf{k}\cdot\mathbf{r} - \omega t\right)\right] \tag{2.1}$$

where $\mathbf{E}_0$ is a constant vectors giving the amplitude and direction of the related wave at position $\mathbf{r}$, $\mathbf{k}$ the wave vector with modulus given by

$$k = n\omega / c \tag{2.2}$$

where n is the refractive index, ω and c the frequency and the speed of light, respectively. It is convenient to decompose each wave vector into a component perpendicular (Transverse Electric (TE) wave, denoted by subscript s) and another component parallel (Transverse Magnetic (TM) wave, denoted by subscript p) to the plane of incidence, which is defined by the direction of the incident light and the normal of the tangential surface of the boundary. These two components are independent to each other and any polarisation light can be obtained by linear superposition of them.

When light incident on an interface between two media, part of the light is reflected and the rest penetrates to the second medium, as shown in Fig. 2.1.

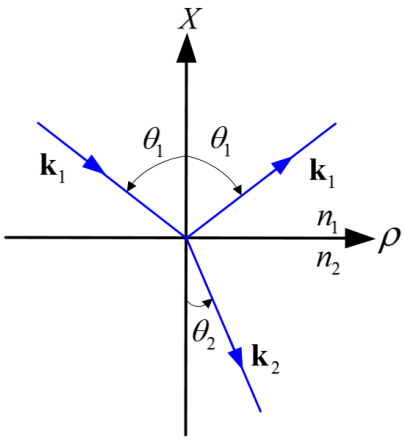

Figure 2.1: Light propagation near an interface.

The ratios of the amplitude of the reflected light and transmitted light to that of the incident light are given by Fresnel's coefficients for the TM and TE polarised light in the form of [11]

$$r_p = \frac{n_2 \cos\theta_1 - n_1 \cos\theta_2}{n_2 \cos\theta_1 + n_1 \cos\theta_2} \tag{2.3}$$

$$t_p = \frac{2n_1 \cos\theta_1}{n_1 \cos\theta_2 + n_2 \cos\theta_1} \tag{2.4}$$

$$r_s = \frac{n_1 \cos\theta_1 - n_2 \cos\theta_2}{n_1 \cos\theta_1 + n_2 \cos\theta_2} \tag{2.5}$$

$$t_s = \frac{2n_1 \cos\theta_1}{n_1 \cos\theta_1 + n_2 \cos\theta_2} \tag{2.6}$$

where $n_i, i = 1,2$ are the refractive index of the two media, and $\theta_i, i = 1,2$ the angles of the incident light and the refracted light, respectively. The above equations are still valid when the media is absorbing, provided that the refractive index of the media is represented by a complex number, the imaginary part of which is the extinction coefficient of the medium [12]. Then the angles given by the Snell's law, i.e. $n_1 \sin\theta_1 = n_2 \sin\theta_2$, will no longer represents the direction of light propagation. It is convenient to express the Snell's law as [12]

$$k_{1\rho} = k_{2\rho} \tag{2.7}$$

where $k_{1\rho}$ and $k_{2\rho}$ are the wave vector components in the ρ direction. It is seen that Snell's law is equivalent to the conservation of the in-plane wavenumber. The Fresnel coefficients can also be given by the wavenumber components as [12]

$$r_p = \frac{n_2^2 k_{1x} - n_1^2 k_{2x}}{n_2^2 k_{1x} + n_1^2 k_{2x}} \tag{2.8}$$

$$t_p = \frac{2 n_1 n_2 k_{1x}}{n_1^2 k_{2x} + n_2^2 k_{1x}} \tag{2.9}$$

$$r_s = \frac{k_{1x} - k_{2x}}{k_{1x} + k_{2x}} \tag{2.10}$$

$$t_s = \frac{2 k_{1x}}{k_{1x} + k_{2x}} \tag{2.11}$$

where k_{1x} and k_{2x} are the wavenumber components in the X direction.

2.3 Reflectance, transmittance and absorbance

The fraction of incident energy reflected from the interface and transmitted into the second medium are given by the reflectance and transmittance defined by

$$R = |r|^2 \tag{2.12}$$

$$T = \frac{n_2 \cos\theta_2}{n_1 \cos\theta_1} |t|^2 \tag{2.13}$$

where r and t are the Fresnel reflection and transmission coefficients, respectively. For an absorbing medium the absorbance can be obtained by

$$A = 1 - R - T \tag{2.14}$$

2.4 Total internal reflection and evanescent waves

Now we consider light incident from a large refractive index medium n_1 to a small refractive index medium n_2 ($n_1 > n_2$). If the incident angle θ_1 equals to a critical angle θ_c given by $n_1 \sin\theta_c = n_2$, then the angle of refraction equals to 90 degrees. This means that the refracted light propagates along the interface, no energy flows across the interface and all the incident light are reflected back into medium 1. This phenomena is called Total Internal Reflection (TIR).

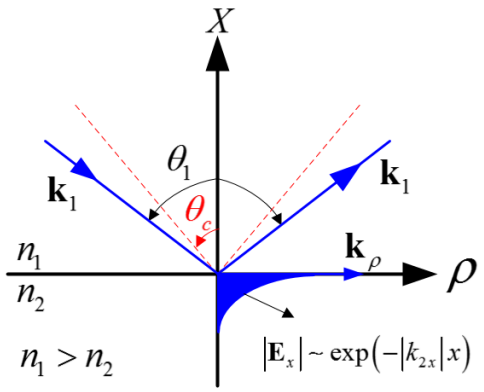

Figure 2.2: Total internal reflection at an interface.

When $\theta_i > \theta_c$ the wavenumber component k_{2x} becomes pure imaginary due to the conservation of the in-plane wavenumber component across the interface. At this condition, the Fresnel equations for reflection can be written as

$$r_p = \frac{n_2^2 k_{1x} - i n_1^2 |k_{2x}|}{n_2^2 k_{1x} + i n_1^2 |k_{2x}|} = 1 \cdot \exp\left(-2\phi_{21}^p\right) \tag{2.15}$$

$$r_s = \frac{k_{1x} - i|k_{2x}|}{k_{1x} + i|k_{2x}|} = 1 \cdot \exp\left(-2\phi_{21}^s\right) \tag{2.16}$$

where ϕ_{21}^p and ϕ_{21}^s are the phase angles given by

$$\phi_{21}^p = \arctan \frac{n_1^2 |k_{2x}|}{n_2^2 k_{1x}} \tag{2.17}$$

$$\phi_{21}^s = \arctan \frac{|k_{2x}|}{k_{1x}} \tag{2.18}$$

It is seen that the modulus of the Fresnel reflection coefficient for both TM and TE waves are unity when TIR happens. Thus the incident waves are totally reflected. The amplitude of the reflected waves is only different from that of the incident wave by a phase factor. However, the electric field in medium 2 is non-zero and it is given by

$$E_2 = E_t \exp\left[i\left(k_\rho \rho - \omega t\right)\right] \exp\left(-|k_{2x}| x\right) \tag{2.19}$$

where E_t is the amplitude of the transmitted wave. It is seen that the transmitted wave decreases exponentially along the X direction and cannot be observed in this direction when far away from the interface. So this kind of wave is called evanescent wave. It is seen from Eq. (2.19) that this wave has real wavenumber component in the ρ direction, so it is a surface wave

propagating along the interface. In the next section, we show that the radiation of excited fluorescent molecules contains such evanescent waves.

2.5 Dipole radiation near interface

Many excited atoms or molecules can be modelled as electric dipoles since the electronic transitions that produce photons are electric dipoles in nature [13]. In a homogeneous medium with refractive index n_1 the electromagnetic radiation field of an electric dipole is given by a scalar Green's function [14]

$$g(\mathbf{r},\mathbf{r}_S)=\frac{\exp\left(ik_1\left|\mathbf{r}-\mathbf{r}_s\right|\right)}{4\pi\left|\mathbf{r}-\mathbf{r}_s\right|} \tag{2.20}$$

where $\mathbf{r}$ and $\mathbf{r}_s$ are the locations of the observing point and the dipole, respectively, and $k_1=n_1\omega/c$ the wavenumber.

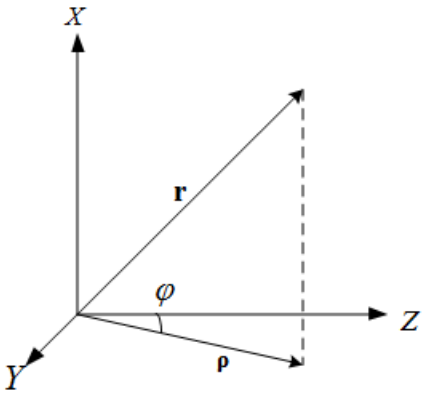

Figure 2.3: Conversion from Cartesian coordinates to cylindrical coordinates.

It is seen from Eq. (2.20) that the scalar Green's function represents a spherical wave attenuated by the distance to the source point. This spherical wave can be converted to planar waves via the use of the Sommerfeld identity given by [15]

$$g(\mathbf{r},\mathbf{r}_S)=\frac{i}{4\pi}\int_0^\infty dk_\rho\frac{k_\rho}{k_x}J_0(k_\rho\left|\boldsymbol{\rho}-\boldsymbol{\rho}_S\right|)\exp\left(ik_x\left|x-x_S\right|\right) \tag{2.21}$$

In Eq. (2.21) the zero-order Bessel function and cylindrical coordinates are introduced, where $k_\rho^2+k_x^2=k_1^2$, k_ρ and k_x are the in-plane and vertical wavenumbers, respectively, $\boldsymbol{\rho}=y\hat{y}+z\hat{z}$, and $\hat{x}$, $\hat{y}$, $\hat{z}$ are the unit vectors in the X, Y, Z directions, respectively. The conversion from Cartesian coordinates to cylindrical coordinates is shown in Fig. 2.3. The Sommerfeld identity converts the spherical wave into an integral of planar waves in the x direction multiplied with cylindrical wave in the ρ direction over all the available in-plane wavenumbers.

When bringing the dipole close to the surface of a medium with larger refractive index n_2 ($n_2 > n_1$), the in-plane wavenumber components of the dipole radiation, which satisfies $k_1 < k_\rho < k_2$ where $k_2 = n_2\omega / c$, are evanescent waves propagating along the interface between the two media and penetrate to medium 2 as propagating waves; the low wavenumber components $k_\rho < k_1$ are still freely propagating waves in medium 2 and they are called the far field radiation of the dipole; the high wavenumber components $k_\rho > k_2$ cannot propagate in both of the two media and they are called the near field radiation of the dipole.

To illustrate these waves more clearly, MATLAB is used to evaluate the Sommerfeld identity given by Eq. (2.21) and the electromagnetic field of a dipole emitting in layered structures can be obtained by applying related boundary conditions near the interfaces. The spatial distribution of the electric field generated by a vertical electric dipole emitting at different distances to the interface of air and crystalline silicon (located at $x = 0$) are shown in Fig. 2.4. The observation plane of the electric field is at $y = 0$. The wavelength of light in consideration is 600 nm and the related refractive index of silicon is from [16].

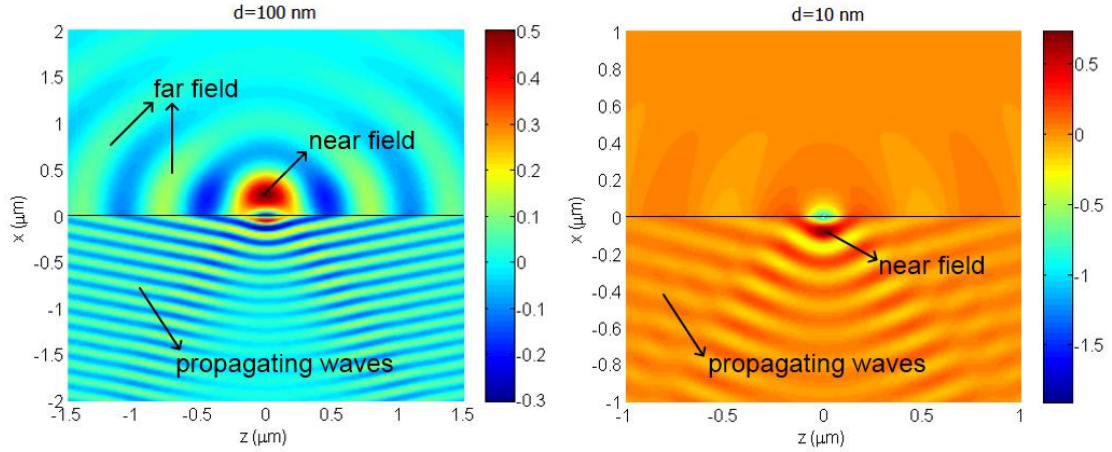

Figure 2.4: Electric field distribution of a vertical electric dipole emitting near silicon.

It is illustrated in Fig. 2.4 that at $d = 100\ \text{nm}$, the far field radiation propagates away from the dipole emitting centre, while the near field counterpart stays near the dipole emitting centre with limited expansion over space. The propagating waves in silicon (below $x = 0$) are penetrated from the evanescent waves of the dipole radiation. We return to this point after the introduction of photon tunnelling. At $d = 10\ \text{nm}$, the maximum of the electric field which is effectively the near field moves to the silicon side. And the far field radiation in air nearly disappears. This phenomenon signifies energy transfer from the dipole to silicon at close distance.

2.6 Frustrated total internal reflection and photon tunnelling

The evanescent wave discussed in the previous two sections can also be converted to propagating waves in the evanescent direction when it acts with nearby matters. This phenomenon is called Frustrated Total Internal Reflection (FTIR) and it was noticed in the times of Newton [17]. The most notable experiment was conducted by Bose more than a century ago [8], who brought two prisms at close distance but without contact, as shown in Fig. 2.5 (a). The evanescent wave from the incident prism penetrates the air gap and transmitted into the second prism. This phenomenon is analogous to quantum (with energy E) tunnelling through the same potential barrier V ($V > E$) which confines photons inside the exciting prism by TIR. The form of the Helmholtz equation for the optical waves resembles the time-independent Schrödinger equation for the wave function of the quantum, and the transmittance of photons is identical to the quantum tunnelling probability given by the solution of the Schrödinger equation [18].

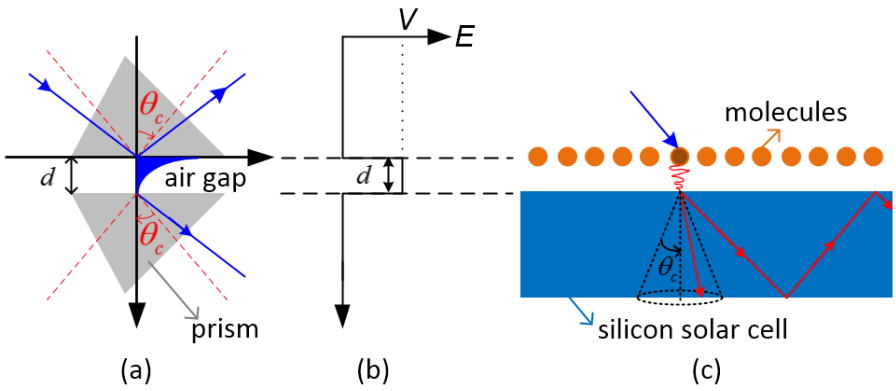

Figure 2.5: (a) Photon tunnelling through an air gap between two prisms; (b) quantum tunnelling through a barrier; (c) photon tunnelling into a silicon solar cell.

Due to the conservation of the in-plane wavenumber, the propagation angle of the tunnelled light in Fig. 2.5 (a) is also larger than the critical angle for TIR. Thus, if the second prism is replaced by a planar waveguide such as a silicon solar cell, the incident light on the first prism can be coupled to the trapped modes in the silicon solar cells, in other words, the waveguide modes, which is discussed in Sec. 2.8.3. As illustrated in Fig. 2.5 (c), our approach to inject waveguide modes into silicon solar cells is simply by replacing the exciting prism with fluorescent molecules, which are effectively working as electric dipoles when excited by incident light. The evanescent waves radiated by these excited molecular dipoles can tunnel to the underlying silicon solar cell as trapped modes. Thus via the use of fluorescent molecules the incident light can be injected to the trapped modes in the silicon solar cell to enhance the capture of light in silicon. We show in Chapter 8 and Chapter 9 that this energy injection process is efficient: the energy transfer probability is larger than 70% even when the underlying silicon is merely 25 nm thick.

2.7 Transfer matrix method and its applications

A convenient way to model light reflection, transmission and absorption of optical waves in layered structures is the transfer matrix method introduced by Yeh [12]. This section reviews this method and its applications in optical devices.

2.7.1 Characteristic matrices

The amplitude of the incident, reflected and transmitted waves surrounding a single layer medium can be related via a simple 2×2 matrix. As shown in Fig. 2.6, a single layer medium with refractive index n_2 is placed between two different media with refractive indices n_1 and n_3, respectively.

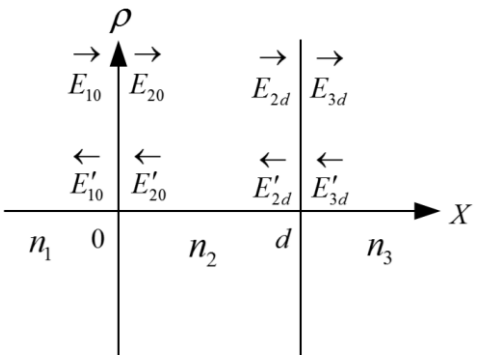

Figure 2.6: Optical waves propagating near a single dielectric layer.

The planar waves in each layer has the form of $E = E(x)\exp\left[i(k_\rho \rho - \omega t)\right]$. As denoted by the arrows in Fig. 2.6, the waves in each layer consists a right-travelling and a left-travelling wave and $E(x)$ is the sum of these two waves

$$E(x) = E_1 \exp(k_x x) + E_1' \exp(-k_x x) = \left[\exp(k_x x) \quad \exp(-k_x x)\right]\begin{bmatrix} E_1 \\ E' \end{bmatrix} \tag{2.22}$$

where E_1 and E_1' are the amplitudes and are constants in each layer. The 2×2 transfer matrix which links the waves on the left and right side of the interface at $x = 0$ is given by

$$\begin{bmatrix} E_{10} \\ E_{10}' \end{bmatrix} = \frac{1}{t_{12}}\begin{bmatrix} 1 & r_{12} \\ r_{12} & 1 \end{bmatrix}\begin{bmatrix} E_{20} \\ E_{20}' \end{bmatrix} \tag{2.23}$$

where r_{12} and t_{12} are the Fresnel reflection and transmission coefficients at the interface $x = 0$. For waves travelling distance d inside layer 2, the 2×2 matrix is given by

$$\begin{bmatrix} E_{20} \\ E_{20}' \end{bmatrix} = \begin{bmatrix} e^{-i\phi} & 0 \\ 0 & e^{i\phi} \end{bmatrix}\begin{bmatrix} E_{2d} \\ E_{2d}' \end{bmatrix} \tag{2.24}$$

where the phase retardation is given by

$$\phi = k_{2x} d \tag{2.25}$$

The amplitudes of waves propagating in multi-layered structures can be related by successive multiplication of the matrices given in Eq. (2.23) and Eq. (2.24).

2.7.2 Reflection, transmission and absorption near a thin layer

The transfer matrix which links the waves near the thin layer shown in Fig. 2.6 can be expressed as

$$\begin{bmatrix} E_{10} \\ E'_{10} \end{bmatrix} = \begin{bmatrix} M_{11} & M_{12} \\ M_{21} & M_{22} \end{bmatrix} \begin{bmatrix} E_{3d} \\ E'_{3d} \end{bmatrix} \tag{2.26}$$

where

$$\begin{bmatrix} M_{11} & M_{12} \\ M_{21} & M_{22} \end{bmatrix} = \frac{1}{t_{12}} \begin{bmatrix} 1 & r_{12} \\ r_{12} & 1 \end{bmatrix} \begin{bmatrix} e^{-i\phi} & 0 \\ 0 & e^{i\phi} \end{bmatrix} \frac{1}{t_{23}} \begin{bmatrix} 1 & r_{23} \\ r_{23} & 1 \end{bmatrix} \tag{2.27}$$

Then the reflection and transmission coefficients of a single layer can be obtained as

$$r = \frac{E'_{10}}{E_{10}} = \frac{M_{21}}{M_{11}} = \frac{r_{12} + r_{23} e^{i2\phi}}{1 + r_{12} r_{23} e^{i2\phi}} \tag{2.28}$$

$$t = \frac{E_{3d}}{E_{10}} = \frac{1}{M_{11}} = \frac{t_{12} t_{23} e^{i\phi}}{1 + r_{12} r_{23} e^{i2\phi}} \tag{2.29}$$

Equation (2.28) and Eq. (2.29) are called Airy's summations [11]. Inserting these two summations into Eq. (2.14), the absorbance of a thin layer can be readily obtained as

$$A = 1 - \left| \frac{r_{12} + r_{23} e^{i2\phi}}{1 + r_{12} r_{23} e^{i2\phi}} \right|^2 - \frac{n_3 \cos\theta_3}{n_1 \cos\theta_1} \left| \frac{t_{12} t_{23} e^{i\phi}}{1 + r_{12} r_{23} e^{i2\phi}} \right|^2 \tag{2.30}$$

This equation is discussed further in Chapter 6 to model the quantum efficiency of a 200 nm thick crystalline silicon solar cell.

2.7.3 Anti-reflection coating design

Near 30% of incident light on bare crystalline silicon is reflected back [19]. In order to reduce this reflection loss of silicon solar cells, anti-reflection coating (ARC) should be deposited on the surface of silicon. For single layer ARC structure, the reflectance is given by Eq. (2.28). To totally suppress reflection, we only need to fulfil $r_{12} + r_{23} e^{i2\phi} = 0$. And this condition leads to the

conclusion that the minimum thickness of a single layer of ARC is $\lambda / 4n_{\mathrm{ARC}}$ for light incident in the normal direction to the silicon solar cell surface, where λ is the wavelength of light and n_{ARC} the refractive index of the ARC material given by the square root of the refractive index of silicon.

2.8 Optical modes in a thin dielectric layer

This section reviews the optical modes supported by a thin dielectric layer.

2.8.1 Radiation modes

As shown in Fig. 2.7, the incident light from medium 1 undergoes multiple reflections in the thin layer 2 with thickness of t, and finally part of them transmits into layer 3. Figure 2.7 also shows the refractive indices ($n_1 < n_2, n_3 < n_2$) and light propagation angles in each layer. According to Snell's law, the propagation angle of light in the thin layer will be limited to the range of $0 < \theta_2 < \theta_c$. Light of this kind can propagate freely inside and outside of the thin layer, and they are called radiation modes of the thin layer, in contrast to the trapped waveguide modes, which is discussed in Sec. 2.8.3.

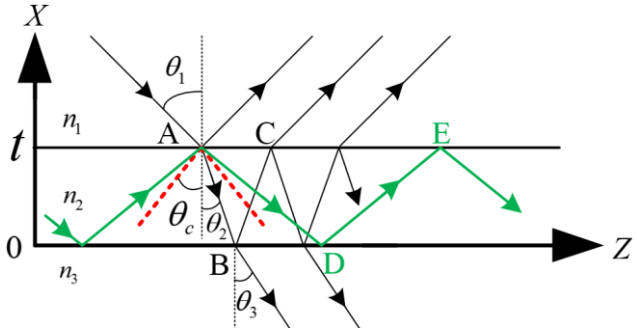

Figure 2.7: Light propagating near a thin layer.

2.8.2 Fabry-Perot modes

Fabry-Perot modes is a special kind of radiation modes, it is discussed here to distinguish with the waveguide modes introduced in the next section. As shown in Fig. 2.7, light inside the thin layer undergoes multiple reflections. If the phase shift for light travelling one period inside the thin layer satisfies the condition for constructive interference, i.e. $\Delta\phi_{ABC} = m \cdot 2\pi \quad (m = 0,1,2,3\ldots)$, then these resonant modes are called the Fabry-Perot modes. The phase shift of light in one period includes the phase shift after travelling from A to B, and the phase shift when reflection occurs at B and C. Then the constructive interference condition is given by

$$2k_{2x}t - 2\phi_{21} - 2\phi_{23} = m \cdot 2\pi \quad (m = 0,1,2,3\ldots) \tag{2.31}$$

Since all the propagation angles $\theta_i, i = 1,2,3$ are real and the phase shift $\phi_{21} = \phi_{23} = 0$, the Fabry-Perot modes can be simply find out by

$$2k_{2x}t = m \cdot 2\pi \quad (m = 0,1,2,3...) \tag{2.32}$$

2.8.3 Waveguide modes

The waveguide modes are the internal modes trapped in the thin layer by TIR, as shown by the green light path in Fig. 2.7. However, according to the Snell's law, these internal modes cannot be excited by ordinary incident planar waves, as shown by Fig. 2.8 (a). Only the radiation modes can be excited inside the cone defined by the critical angle for TIR. While the evanescent waves emitted by excited fluorescent molecules can be injected to the forbidden zone as waveguide modes via photon tunnelling, which is discussed in Sec. 2.6.

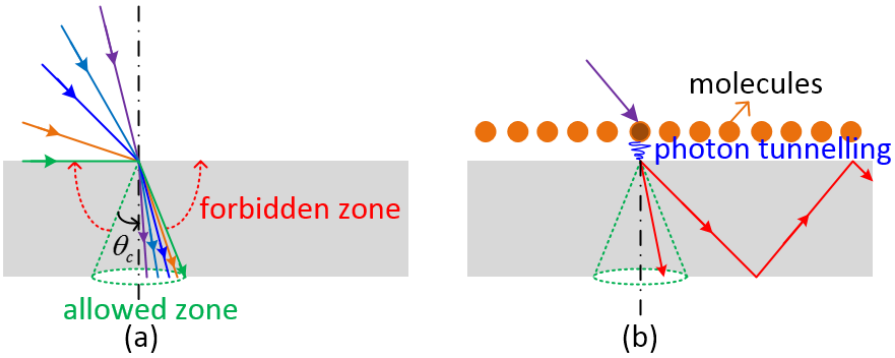

Figure 2.8: (a) Normal light refraction near a thin layer and (b) photon tunnelling from molecules.

These trapped modes undergoes TIR on both the top and bottom surface of the thin layer and they also satisfy the condition for constructive interference as given by Eq. (2.31), which is called the characteristic equation for waveguide modes and the integer m represents the index number of the waveguide mode [20]. In comparison with the Fabry-Perot modes, the phase shifts of light reflection at the locations D and E shown in Fig. 2.7 are non-zero for the waveguide modes, and the phase angles ϕ_{21} and ϕ_{23} can be obtained from Eq. (2.17) and Eq. (2.18) for TM and TE waves, respectively.

Equation (2.31) has discrete solutions when the thickness of the thin layer is in the order of the wavelength of light, which means that in this thickness range only a few waveguide modes can be supported by the thin layer. And as the thickness decreases, the number of supportable waveguide modes also drops down. When a certain order of mode cannot be supported, the related thickness is called the cut-off thickness for that mode. Rewriting Eq. (2.31), the cut-off thickness can be obtained as

$$t_c^{\mathrm{TM}} = \frac{m\pi\lambda + \lambda \arctan\sqrt{a_{\mathrm{TM}}}}{2\pi\sqrt{n_1^2 - n_2^2}} \quad (m = 0,1,2,3...) \tag{2.33}$$

$$t_c^{\mathrm{TE}} = \frac{m\pi\lambda + \lambda \arctan\sqrt{a_{\mathrm{TE}}}}{2\pi\sqrt{n_1^2 - n_2^2}} \quad (m = 0,1,2,3...) \tag{2.34}$$

where a_{TE} and a_{TM} are called the asymmetric parameters of the waveguide and they are given by $a_{\mathrm{TE}} = \left(n_2^2 - n_3^2\right) / \left(n_1^2 - n_2^2\right)$ and $a_{\mathrm{TM}} = \left(n_1 / n_3\right)^4 a_{\mathrm{TE}}$, respectively.

2.9 Conclusion

This chapter reviews the optical concepts such as Fresnel coefficients, (frustrated) total internal reflection, evanescent waves, photon tunnelling, Fabry-Perot modes and waveguide modes. And these concepts lead to the conclusion that the evanescent waves emitted by an excited fluorescent molecule can couple to a nearby silicon solar cell as trapped waveguide modes via photon tunnelling. The transfer matrix method, which represents a convenient tool to model light propagation in layered structures, and its application in optical devices are also reviewed. The following chapters discuss the application of these optical concepts in planar photovoltaic devices such as fluorescent solar collectors and silicon solar cells.

Chapter 3 Light Source and Silicon Solar Cells

3.1 Introduction

Solar Cells are semiconductor devices that can convert sunlight into electricity via the photovoltaic effect. This chapter reviews light source for solar cells and the operation principle of ideal single-junction silicon solar cells. The theoretical efficiency limits of single junction solar cells are also reviewed.

3.2 Solar radiation

3.2.1 Blackbody radiation

To a good approximation, the Sun acts as a perfect blackbody radiator with the temperature T_s close to 6000 K. The radiation spectrum or the energy distribution from a blackbody is given by Planck's equation for blackbody radiation

$$I(\nu,T)=\frac{2h\nu^3}{c^2}\frac{1}{e^{\frac{h\nu}{k_BT}}-1} \tag{3.1}$$

where $I(\nu,T)$ is the energy per unit time emitted by the blackbody, per unit area of the emitting surface in the normal direction, per unit solid angle and per unit frequency, h the Planck constant, c the speed of light, ν the emission frequency, k_B the Boltzmann constant, and T the temperature of the blackbody. While for luminescent radiation, a generalised Planck's law is given by [21]

$$I(\nu,T,\mu)=\frac{2h\nu^3}{c^2}\frac{1}{e^{\frac{h\nu-\mu}{k_BT}}-1} \tag{3.2}$$

where μ is the chemical potential of the luminescent photons. For blackbody radiation the chemical potential of the emitted photons is zero, whereas for luminescence it is non-zero [22] and experimentally quantifiable [23]. We shall call the luminescent radiation quasi-blackbody radiation [6].

3.2.2 Solar constant and solar spectrum

The solar constant S, which is defined as the average energy flux incident on a unit area perpendicular to the sun light beam outside the Earth's atmosphere, can be approximated by dividing the surface area of a sphere with diameter given by the Sun-Earth mean distance R_{SE} into the total energy radiated by the sun blackbody and is given by

$$S = f_\omega \sigma T_S^4 \tag{3.3}$$

where σ is the Stefan-Boltzmann constant and f_ω is a geometrical factor given by

$$f_\omega = \left(\frac{R_S}{R_{SE}} \right)^2 \tag{3.4}$$

where R_S is the radius of Sun. By using Planck's law, the energy per unit time, per unit wavelength interval, and per unit area received from the Sun just outside the Earth's atmosphere is given by

$$f(\lambda, T_S, \Omega_S) = I(\lambda, T_S) \cdot \Omega_S = \frac{2hc^2}{\lambda^5} \frac{1}{e^{\frac{hc}{\lambda k_B T}} - 1} \cdot \pi f_\omega \tag{3.5}$$

where Ω_s denotes the solid angle subtended by Sun when seen from the Earth. The solar radiation is attenuated through scattering and absorption by air molecules, aerosols and dust particles in the atmosphere by approximately 30% before it reaches the Earth surface [24]. An air mass, which is defined as the atmospheric path length relative to the minimum path length when the sun is directly overhead (denoted by AM1), is used to distinguish the different solar spectra received at Earth surface when the Sun is moving relatively to the observing point. The spectrum of the extra-terrestrial radiation, which is not attenuated by the atmosphere, is denoted by AM0. The atmosphere not only attenuates the intensity but also changes the spectrum of the solar radiation received at different locations of the globe. AM1.5 spectrum is a typical solar spectrum on Earth's surface on a sunny day. In order to compare the efficiencies of solar cells worldwide, artificial solar simulators equipped with electric light source such as Xenon lamps and related filters are used to test the efficiency of solar cells. The radiation spectrum of the solar simulator is similar to the standard AM1.5 solar spectrum and the light intensity is tuned to 1 kW/m^2 in the efficiency measurements. For solar cells used on satellites and space ships outside the atmosphere of the Earth, the standard testing condition employs the AM0 spectrum [24].

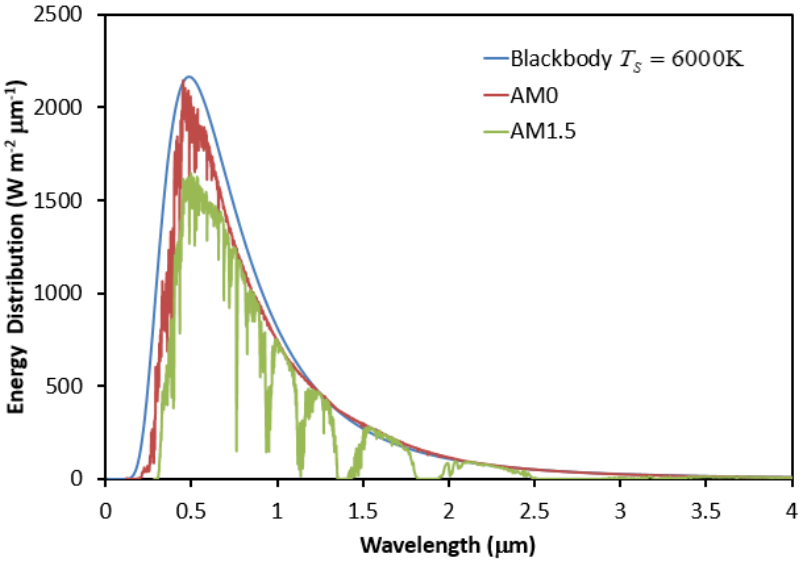

Figure 3.1: Energy distribution of blackbody radiation and solar spectra.

Figure 3.1 compares the energy distribution of the blackbody radiation at $T_s = 6000\text{K}$ and the solar radiation spectrum given by NREL [25], [26]. The blackbody radiation is close to the extra-terrestrial solar radiation spectrum AM0. Due to the attenuation of the atmosphere, the AM1.5 solar radiation spectrum is lower than the AM0 spectrum at certain spectra bands.

3.2.3 Direct radiation and diffuse radiation

The radiation which is not reflected or scattered and reaches the Earth ground directly is called direct radiation. The scattered radiation which reaches the Earth's ground is called diffuse radiation. Diffuse radiation is an important component of the solar radiation. In cloudy skies, most of the solar radiation is diffuse radiation. Even in clear and cloudless skies, the diffuse component can account to 10 to 20% of the total radiation received by a horizontal surface during the day [27]. In central and northern Europe more than 50% of the arriving energy results from diffuse radiation [28]. Thus in order to improve the efficiency of solar converters, diffuse radiation must be captured, for example, by fluorescent solar collectors.

3.3 Molecular Fluorescence

Solar radiation can be converted to molecular fluorescence to excite solar cells. The advantage of using molecules is that solar radiation can be converted to the waveguide modes in solar converters such as fluorescent solar collectors and silicon solar cells, which is discussed further in the following chapters.

3.3.1 Light interaction with fluorescent molecules

Light interaction with fluorescent molecules can be understand by reviewing the Jablonski diagram, which is shown in Fig. 3.2. In the event of molecular fluorescence, a fluorescent

molecule first absorbs the energy of incident light and this energy excites an electron from the ground state S_0 to one of the vibrational states coupled with a higher electronic state S_n. Then the excited electron loses part of its energy via vibrational relaxation and internal conversion via collision with nearby molecules, and goes back to the first electronic state S_1. Then, the excited electron goes back to the ground state S_0 with the emission of fluorescence. An alternative process to fluorescence is that the excited electron migrates to one of vibrational states coupled with the triplet state T_1, and return to the ground state S_0 via the emission of phosphorescence. In addition to fluorescence and phosphorescence, there are also non-radiative transitions from S_1 to S_0, which are caused by, for example, collisional quenching or resonance energy transfer to nearby molecules.

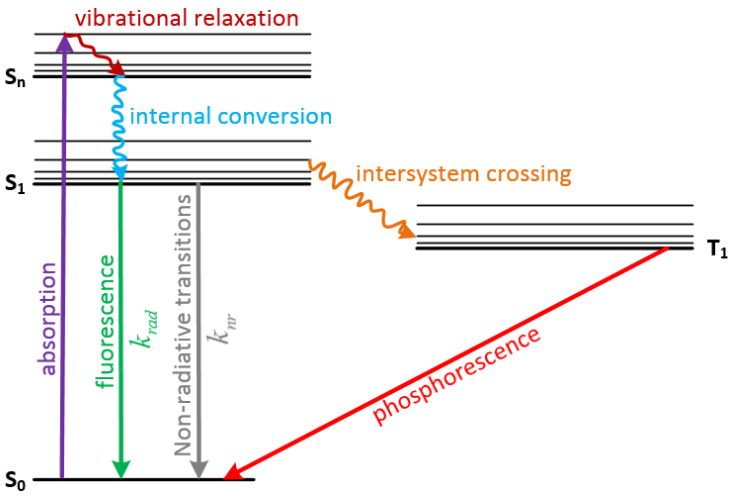

Figure 3.2: A Jablonski diagram showing transition processes in fluorescent molecules [29].

Compared to fluorescence, phosphorescence has a lower probability since the intersystem crossing needs a spin-flip, and another spin-flip is required in the process of phosphorescence. In this thesis, phosphorescence is neglected.

3.3.2 Fluorescence spectra

Three kinds of fluorescence spectra are measured: the excitation, the absorption and the emission spectra. The excitation spectrum is measured by recording the fluorescence intensity at a fixed long wavelength of light, where the fluorescent molecules have weak absorption, with different excitation wavelength of light. The absorption spectrum or the spectral absorbance of the fluorescent molecules is obtained from

$$A(\lambda) = \log_{10}\left[\frac{I_0(\lambda)}{I_t(\lambda)}\right] \tag{3.6}$$

where $I_0(\lambda)$ and $I_t(\lambda)$ are the incident and transmitted photon flux. The emission spectrum is obtained by exciting the fluorescent molecules at a fix wavelength, where the molecules absorb strongly, and recording the fluorescence intensity at different wavelength.

3.3.3 Fluorescence quantum yield and fluorescence lifetime

Fluorescence quantum yield quantifies the efficiency of fluorescence process, and it is given by the fraction of absorbed photons that are emitted. Due to the non-radiative transitions, the quantum yields for fluorescent molecules are less than unity. The quantum yield can also be obtained from

$$\phi_f = \frac{k_{rad}}{k_{rad} + k_{nr}} = \frac{1/\tau_{rad}}{1/\tau_{rad} + 1/\tau_{nr}} \tag{3.7}$$

where k_{rad} and k_{nr} are the radiative and non-radiative decay rate, respectively, and τ_{rad} and τ_{nr} the lifetimes of the two processes, respectively. Note that the radiative lifetime is not the measured natural lifetime, which is given by

$$\tau_f = \frac{1}{k_{rad} + k_{nr}} = \frac{1}{1/\tau_{rad} + 1/\tau_{nr}} \tag{3.8}$$

It is seen that the radiative lifetime is related to the natural lifetime via the fluorescence quantum yield, i.e. $\tau_{rad} = \tau_f / \phi_f$. This indicates that the natural lifetime is shorter than the radiative lifetime due to the non-radiative transitions. The fluorescence lifetimes discussed in the following chapters all refer to the measured natural lifetime, unless otherwise stated.

A very short pulse of light can bring a certain number of molecules into the excited state. These excited molecules go back to the ground state by various transition process shown in Fig. 3.2. As in classical chemical kinetics, after a period t the number of excited molecules is [29]

$$N^*(t) = N^*(0)\exp\left(-\frac{t}{\tau_f}\right) \tag{3.9}$$

where $N^*(0)$ is the number of excited molecules just after light excitation. The number of fluorescent photons emitted per unit time is given by

$$N_f = k_{rad} N^*(t) \tag{3.10}$$

It is seen that N_f decreases according to a single exponential. The measured fluorescence intensity in experiments is proportional to N_f. It is shown in Chapter 9 that the time-correlated

single photon counting technique was used to obtain a histogram to fit with Eq. (3.10) to obtain the fluorescence lifetime.

Fluorescence lifetime is an important quantity to characterise fluorescent molecules. However, it is shown in Chapter 7 that the local optical environment can greatly modify the lifetime of fluorescent molecules.

3.4 Light absorption in silicon

All the silicon material discussed in this thesis refers to crystalline silicon, unless otherwise stated. Silicon is the active material in silicon solar cells that absorbs incident solar radiation and converts light into electron-hole pairs. Although silicon solar cell technology dominates the commercial market, silicon is not a good absorber due to its indirect bandgap nature. A typical commercial silicon solar cell needs a few hundreds of micrometres of silicon to achieve efficient operation [19].

3.4.1 Electronic band structure of silicon

Figure 3.3 shows the simplified electronic band structure of silicon [30]. The lowest bandgap is 1.12 eV (corresponds to the energy of a photon at the wavelength of 1108 nm, which is called the cut-off wavelength of silicon), which is the energy difference between the valence band maximum E_v and the conduction band minimum E_c. A direct transition from E_v to E_c is forbidden due to the different values of crystal momentum. Phonons (vibration of lattice) are needed to assist the absorption of photons, as shown in Fig. 3.3. Direct transitions can also occur in silicon when the incident photons have energy larger than the first direct bandgap, which is 3.4 eV (corresponds to the energy of a photon at the wavelength of 365 nm). The electronic band structure determines the strength of photon absorption, and this is reflected by the absorption coefficients of silicon, which is discussed in the following section.

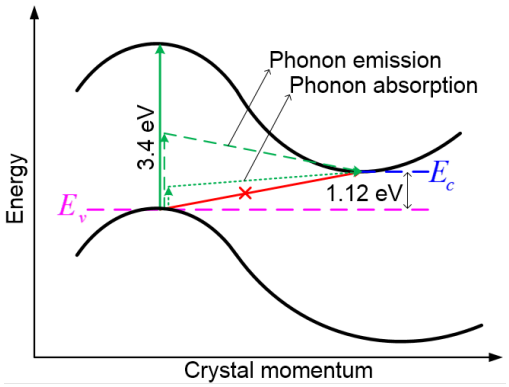

Figure 3.3: Simplified electronic band structure and optical transitions of silicon [30].

3.4.2 Optical property of silicon

The optical property of silicon can be characterised by its complex optical refractive index, which is given by

$$n_{Si}(\lambda) = n(\lambda) + i\kappa(\lambda) \tag{3.11}$$

where n is the normal optical refractive index, κ the extinction coefficient, and λ the wavelength of light. Figure 3.4 shows the measured refractive index and extinction coefficient of silicon at 300 K [16], [31].

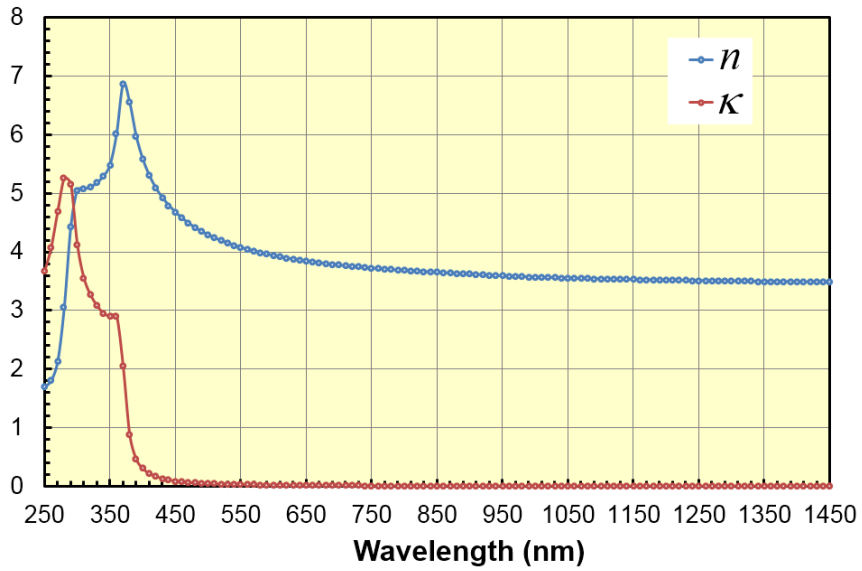

Figure 3.4: Complex optical refractive index of silicon at 300 K.

The absorption coefficient of silicon can be linked to the extinction coefficient by

$$\alpha(\lambda) = \frac{4\pi\kappa(\lambda)}{\lambda} \tag{3.12}$$

The absorption depth of silicon is given by the inverse of the absorption coefficient. It shows the thickness of silicon needed to absorb $1-e^{-1} = 63.21\%$ of incident light. Figure 3.5 shows the absorption coefficient and absorption depth calculated from the extinction coefficient given in Fig. 3.4.

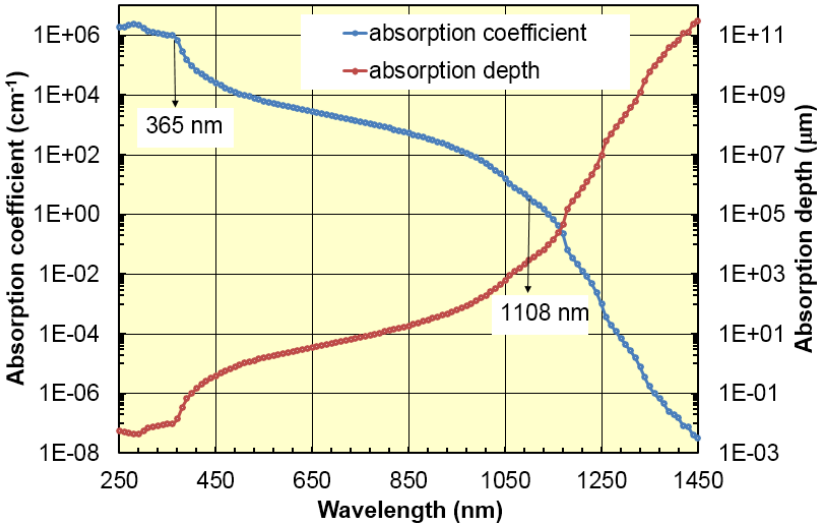

Figure 3.5: Absorption coefficient and absorption depth of silicon at 300 K.

It is seen from Fig. 3.5 that the absorption coefficient is large for wavelength below 365 nm, which corresponds to the first direct bandgap. Then as the wavelength increases, the absorption coefficient decrease rapidly due to indirect transitions. Beyond the cut-off wavelength of 1108 nm, the absorption coefficient is negligible. It is seen that the absorption depth in the wavelength range of 500 nm to the cut-off wavelength is in the order of hundreds of micrometres. This determines the thickness of silicon in commercial solar cells.

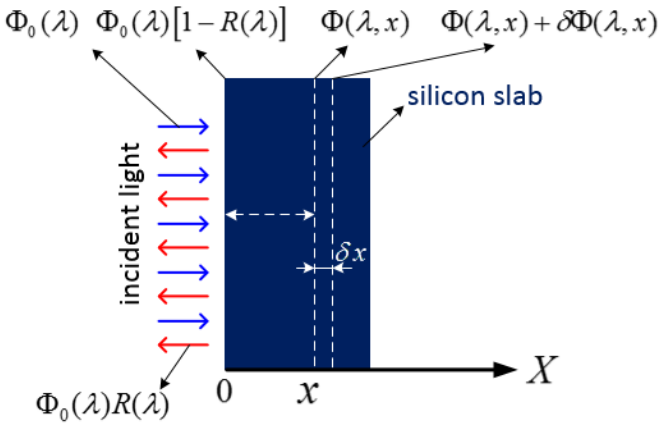

Figure 3.6: Light absorption inside a silicon slab.

When light incident on to a silicon slab, a part of the light is reflected and the rest transmitted into silicon, as shown in Fig. 3.6. According to Beer-Lambert's law, the number of photons at the position x is given by $\Phi(\lambda,x)=\Phi_0(\lambda)[1-R(\lambda)]\exp[-\alpha(\lambda)x]$, where $\Phi_0(\lambda)$ is the number of incident photons, $R(\lambda)$ the reflectance of the silicon surface. A generation function of electron-hole pairs $G(\lambda,x)$, is defined as the number of electron-hole pairs generated in per unit width of the silicon slab at x. Assuming one photon generates one electron-hole pair, the generation

function balances the decrease of the number of photons due to absorption in per unit width of the silicon slab at x and can be obtained as

$$G(\lambda,x)\delta x=-\delta\Phi(\lambda,x)=\Phi_0(\lambda)\left[1-R(\lambda)\right]\exp\left[-\alpha(\lambda)x\right]\alpha(\lambda)\delta x \tag{3.13}$$

This function is used in Sec. 3.7.1 to model the quantum efficiency of a silicon solar cell.

3.5 Principle of silicon solar cells

Silicon solar cell is the dominant technology in commercial market. A typical structure of this kind of solar cell is shown in Fig. 3.7. The base is a p-type semiconductor whereas the emitter is an n-type semiconductor. The top and back contacts are used to collect the generated electrical current. An anti-reflection coating (ARC) layer is deposited on the top surface to decrease the reflection loss, as discussed in Sec.2.7.3.

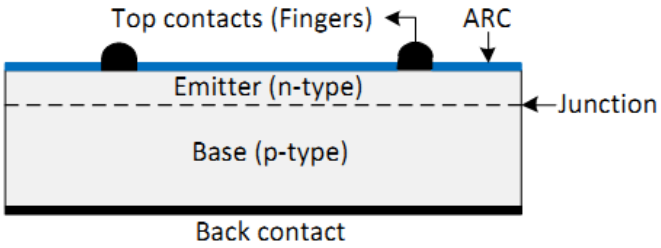

Figure 3.7: Cross-sectional view of a typical solar cell [24].

3.5.1 Carrier concentration and Fermi levels

For non-degenerate semiconductors, the carrier concentrations can be obtained from the density of states in the conduction and valence bands and the occupation probabilities given approximately by the Boltzmann distribution [27]. The electron concentration in the conduction band is given by

$$n=N_c\exp\left(\frac{\mu_e-E_c}{k_BT}\right) \tag{3.14}$$

where N_c is the effective density of states in the conduction band, μ_e the chemical potential or Fermi level for the electrons, E_c the lower conduction band edge energy and T the temperature of the semiconductor. And the hole concentration in the valence band is given by

$$p=N_v\exp\left(\frac{E_v-\mu_h}{k_BT}\right) \tag{3.15}$$

where N_v is the effective density of states in the valence band, E_v the higher valence band edge energy and μ_h the Fermi level for the holes. For n-type semiconductors the electron concentration n is nearly equal to the donor doping concentration N_D, and for p-type semiconductors the hole concentration p is nearly equal to the acceptor doping concentration N_A. A p-n junction in solar cells is obtained either by diffusion of donor into a p-type semiconductor or by diffusion of acceptor into an n-type semiconductor. The majority carriers in each type of semiconductors diffuse to the other side and a depletion region forms near the junction.

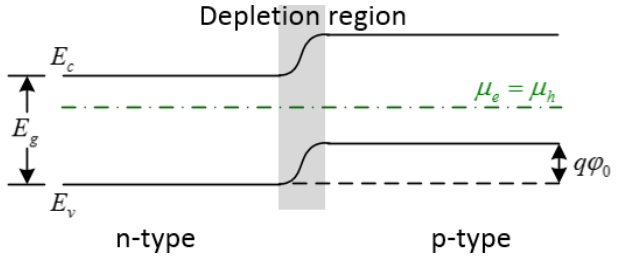

Figure 3.8: Energy band diagram of a p-n junction in thermal equilibrium.

At thermal equilibrium, the Fermi level for electrons and holes equals, i.e. $\mu_e = \mu_h$. Combining Eq. (3.14) and Eq. (3.15), the built-in potential φ_0 of the junction is obtained as

$$\varphi_0 = \frac{k_B T}{q} ln(\frac{N_A N_D}{n_i^2}) \tag{3.16}$$

where n_i is the intrinsic carrier concentration of the semiconductor given by

$$n_i^2 = N_c N_v \exp\left(-\frac{E_g}{k_B T}\right) \tag{3.17}$$

where E_g is the bandgap energy of the semiconductor. Under steady external excitation such as illumination, the carriers generated in each band lose their excess energy via thermal processes such as scattering from lattice vibrations and reach equilibrium in each band before they recombine. Thus the electrons in the conduction band and holes in the valence band are mutually in equilibrium and the Fermi levels of them split as shown in Fig. 3.9. And these two chemical potentials are called quasi-Fermi levels.

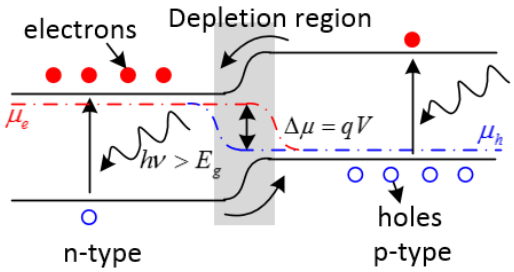

Figure 3.9: Energy band diagram of a p-n junction under steady illumination.

The generated minority carriers in each type semiconductors diffuse to the depletion region and are swept away by the built-in electric field. Thus electrical current is generated across the solar cell and being extracted by the metal contacts. The difference between the quasi-Fermi levels $\Delta\mu$ is equal to the work that can be carried out by an electron if moved round an external circuit, i.e.

$$\Delta\mu = qV \tag{3.18}$$

where V is the external voltage across the junction and q the charge of an electron.

3.5.2 Electrical performance

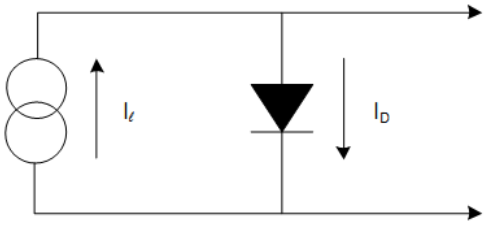

Figure 3.10: Equivalent circuit of an ideal solar cell.

The electrical performance of an ideal solar cell can be approximated by the circuit shown in Fig. 3.10. The light generated current is represented by a current generator in parallel with a diode which represents the p-n junction. The output current is the difference of the light generated current and the diode current, given by

$$I = I_l - I_o\left[\exp\left(\frac{qV}{k_B T}\right) - 1\right] \tag{3.19}$$

where I is the output current, I_l the light generated current, I_o the dark saturation current of the equivalent diode, V the output voltage and T the temperature of the solar cell.

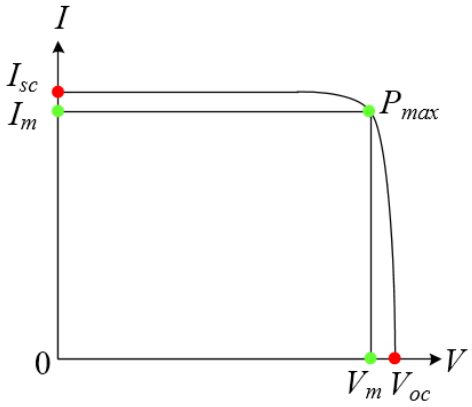

Figure 3.11: I-V characteristic of a solar cell.

Figure 3.11 shows the I-V characteristic of an idealised solar cell. The maximum power can be produced by a solar cell is at the point on the I-V characteristic where the product of the output current and the output voltage is maximum. A fill factor (FF) is defined by

$$FF = \frac{P_{max}}{I_{sc} V_{oc}} \tag{3.20}$$

The efficiency of a solar cell is defined by

$$\eta = \frac{P_{max}}{P_{in}} = \frac{I_{sc} V_{oc} FF}{P_{in}} \tag{3.21}$$

where P_{in} is the power of the incident light.

3.6 Efficiency limits of silicon solar cells

This section reviews the maximum efficiencies that can be achieved by an ideal single junction solar cell: the ultimate efficiency given by Trivich and Flinn (T&F) and the detailed balance efficiency given by Shockley and Queisser (S&Q).

3.6.1 T&F ultimate limit

The number of photons per unit time, per unit wavelength interval, and per unit area received from the Sun just outside the Earth's atmosphere is given by

$$N(\lambda, T_S, \Omega_S) = \frac{f(\lambda, T_S, \Omega_S)}{h\nu} \tag{3.22}$$

T&F [32] gave the ultimate efficiency with the assumption that the output of the solar cell after absorption of a photon with energy larger than the bandgap energy equals to the bandgap energy. This means that the output voltage equals to the 'band gap voltage' given by E_g / q, where E_g is the band gap of the solar cell. They also assumed that each photon with energy

larger than the bandgap energy produces one electron-hole pair. Then the ultimate efficiency is given by

$$\eta_{TF} = \frac{E_g \int_0^{\lambda_g} N(\lambda, T_s, \Omega_S) d\lambda}{\int_0^{\infty} f(\lambda, T_S, \Omega_S) d\lambda} \tag{3.23}$$

where $\lambda_g = hc / E_g$ is the cut-off wavelength of the solar cell and $f(\lambda, T_S, \Omega_S)$ is given by Eq. (3.5).

3.6.2 S&Q detailed balance limit

S&Q [33] gave a detailed balance analysis of the operation of an ideal single junction solar cell. They assumed that the solar cell itself is a quasi-blackbody, the radiation of which is due to the interband radiative recombination of electron-hole pairs inside the solar cell. By assuming that each photon above the bandgap energy generates one electron-hole pair and neglecting non-radiative recombination and any other losses, the output current of the solar cell is given by

$$I = q\left[F_s - F_c(V)\right] \tag{3.24}$$

where F_s is the generation rate of electron-hole pairs and it is equal to the incident photon flux per unit time from the blackbody radiation emitted by the Sun, which is given by

$$F_s = A\int_{\nu_g}^{\infty} N(\nu, T_S, \Omega_S) d\nu \tag{3.25}$$

where A is the area of the solar cell, $N(\nu, T_S, \Omega_S)$ can be obtained from Eq. (3.22). The second term in Eq. (3.24) is the rate of interband radiative recombination, which is given by

$$F_c(V) = F_{c0} \frac{np}{n_i^2} = F_{c0}\left(\frac{qV}{k_B T_c}\right) \tag{3.26}$$

where n and p are the electron and hole concentration in the conduction and valence band, respectively, n_i the concentration of electrons or holes at thermal equilibrium and here F_{c0} represents the recombination rate at thermal equilibrium and can be obtained from the blackbody radiation rate of the solar cell at temperature T_c, which is given by

$$F_{c0} = 2A\int_{\nu_g}^{\infty} N(\nu, T_c, \pi) d\nu \tag{3.27}$$

Then Eq. (3.24) can be written as

$$I = q(F_s - F_{c0}) - qF_{c0}\left[\exp\left(\frac{qV}{k_B T_c}\right) - 1\right] \tag{3.28}$$

Equation (3.28) resembles the current output of the simple equivalent circuit of an ideal solar cell given by Eq. (3.19). The short circuit current equals to $q(F_s - F_{c0})$ and the open circuit voltage can be obtained approximately as

$$V_{oc} \approx \frac{h\nu_g}{q}\left(1 - \frac{T_c}{T_s}\right) + \frac{k_B T_c}{q}\ln\left(\frac{T_s}{T_c}\right) - \frac{k_B T_c}{q}\ln\left(\frac{\pi}{\Omega_s}\right) \tag{3.29}$$

This result has also been obtained by Ruppel and Würfel by considering the photon balance at thermal equilibrium [34]: the absorption rate of the blackbody radiation from the Sun equals to the emission rate of the quasi-blackbody radiation by the solar cell, which is characterised by a non-zero chemical potential μ and given by

$$F_c(\mu) = 2A\int_{\nu_g}^{\infty} N(\nu, T_c, \pi, \mu)d\nu \tag{3.30}$$

By equalling Eq. (3.30) with Eq. (3.25), μ can be obtained. And it is related to the open circuit voltage via Eq. (3.18). The final result for this voltage is identical to Eq. (3.29).

The maximum power output can be found from the I-V characteristic given by Eq. (3.28). And finally the efficiency of the solar cell can be obtained by dividing the power of incident solar radiation into the maximum power output.

3.6.3 Numerical results and discussion

The open circuit voltage given by S&Q is compared with the bandgap voltage, which is the open circuit voltage in the analysis of T&F, for different values of bandgap energy in Fig. 3.12. The open circuit voltages of the world record solar cells [35] are also shown.

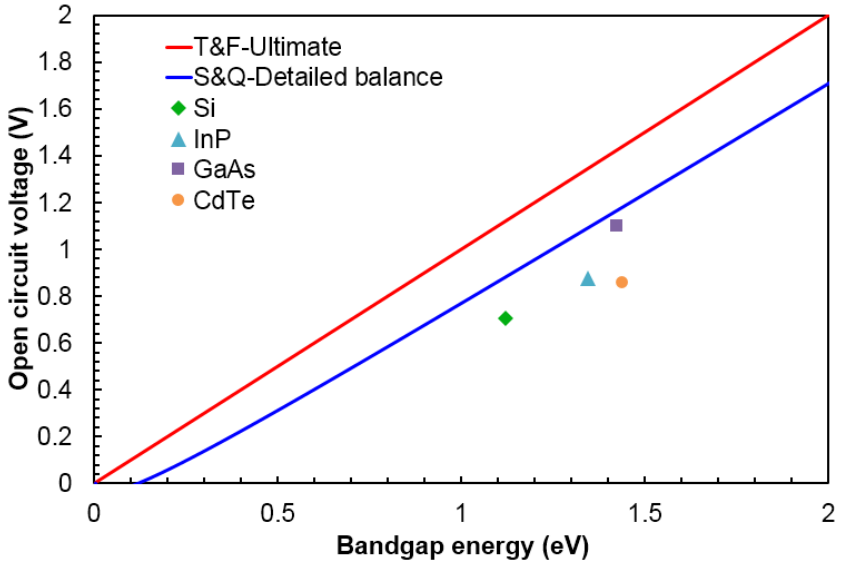

Figure 3.12: Theoretical open circuit voltage of single junction solar cells.

It is seen that the open circuit voltage given by S&Q is always lower than the bandgap voltage. This is because that in comparison with the work by S&Q, T&F did not consider the quasi-blackbody radiation emitted by the solar cell, which is due to interband radiative recombination of photo-generated electron-hole pairs. To restrict the emission from the solar cell, one can set the temperature of the solar cell T_c to be zero, then the open circuit voltage given by Eq. (3.29) equals to the bandgap voltage. Note that the open circuit voltage of the world record GaAs solar cell is close to the S&Q limit.

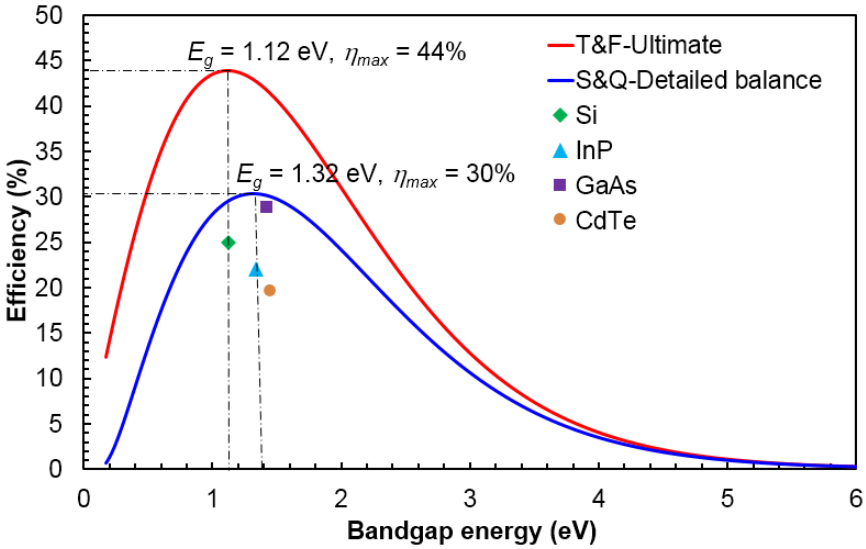

Figure 3.13: Theoretical efficiencies of single junction solar cells.

The numerical results of the T&F ultimate efficiency and the S&Q detailed balance efficiency for single-junction solar cells with different bandgap energy are shown in Fig. 3.13. The efficiencies of the world record solar cells [35] are also shown. Again, note that the efficiency of the world

record GaAs solar cell is 28.8±0.9% under the standard AM1.5 spectrum (1000 W/m^2), which is only 2% away from the S&Q limit.

The work of S&Q makes use of the detailed balance analysis, which represents a major conceptual advance in modelling photovoltaic devices. Similar analyses are also extended to multi-junction solar cells [36] and fluorescent solar collectors [6]. However, because of the approximation used in Eq. (3.26), their analysis can only be applied to non-degenerate statistics, which requires that the doping concentrations are lower than the effective density of states for electrons in the conduction and valence bands, respectively.

3.7 Quantum efficiency of silicon solar cells

The discussion in Sec. 3.6 is limited to idealised solar cells, in which only unavoidable losses are taken into consideration. However, practical solar cells also suffer from avoidable losses such as recombination via defects in the bulk and at the surface, and reflection loss, etc. This section reviews the analytical model for the Internal Quantum Efficiency (IQE) of a simplified silicon solar cell by considering carrier transport in one-dimensional form [37]. The defects in materials is characterised by the lifetime of minority carriers, and the defects at surface are characterised by the surface recombination velocities. The reflection losses only consider that at the top surface of the solar cell. The other practical losses are not considered. The result from this analytical model is compared with PC1D, which is a numerical software commonly used in industry to model solar cells.

3.7.1 Analytical model for an abrupt junction solar cell

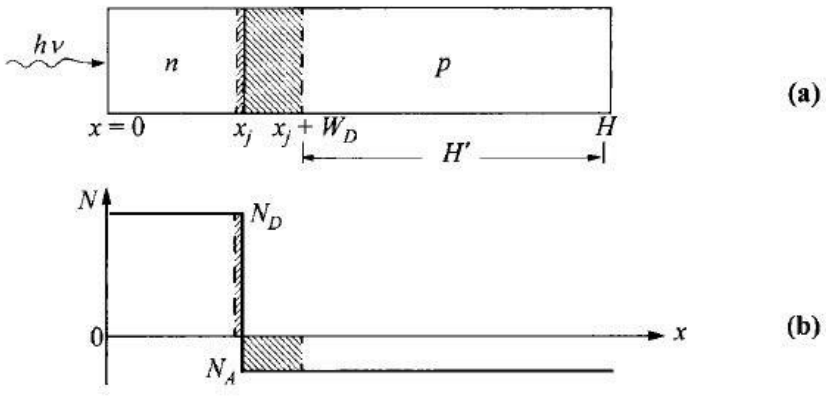

Figure 3.14: (a) Solar cell structure; (b) Doping profile [37].

Figure 3.14 shows the one-dimensional structure and doping profile of the simplified solar cell. Because the doping profile is abrupt in the junction and uniform in both the n-type and p-type semiconductor, via the use of the depletion approximation the solar cell can be divided into

three regions: a quasi-neutral n region from $x=0$ to x_j, a depletion region from x_j to x_j+W_D, and a quasi-neutral p region from x_j+W_D to H, where W_D is the width of the depletion region and given by

$$W_D=\left[\frac{2\varepsilon}{q}\varphi_0(\frac{1}{N_A}+\frac{1}{N_D})\right]^{1/2} \tag{3.31}$$

where ε is the permittivity of the semiconductor, N_A the dopant concentration in the p-type semiconductor, N_D the dopant concentration in the n-type semiconductor and φ_0 the built-in potential of the junction given by Eq. (3.16). Because there is no electric field in the neutral regions, carriers transport in the quasi-neutral regions only consists of a diffusion process. The carrier transport equations are given by

$$D_e\frac{d^2n}{dx^2}=U_e-G_e \tag{3.32}$$

$$D_h\frac{d^2p}{dx^2}=U_h-G_h \tag{3.33}$$

where D_e and D_h are the electron and hole diffusion constant, respectively, which can be obtained from the empirical functions of the dopant concentrations [27], n and p are the minority carriers concentration in the p-type and n-type semiconductors, respectively, U_e and U_h are the bulk recombination rates given by

$$U_e=\frac{n-n_0}{\tau_e} \tag{3.34}$$

$$U_h=\frac{p-p_0}{\tau_h} \tag{3.35}$$

where n_0 and p_0 are the minority carriers concentration at equilibrium, τ_e and τ_h are the lifetime of minority carriers in the p-type and n-type semiconductor, and G_e and G_h are the generation functions, which is given by Eq. (3.13).

To find the exact solution of Eq. (3.33), related boundary conditions should be applied.

(1) At $x=0$, there is surface recombination with recombination velocity S_h:

$$D_h\frac{d(p-p_0)}{dx}=S_h(p-p_0) \tag{3.36}$$

(2) At $x = x_j$ or the depletion region edge, the excess carrier density is negligible due to the strong electric field in the depletion region:

$$p - p_0 \approx 0 \tag{3.37}$$

With these two boundary conditions, one can obtain the hole current density at the depletion edge $x = x_j$ as

$$J_h = -qD_h\left(\frac{dp}{dx}\right)_{x=x_j} = \frac{q\phi(1-R)\alpha L_h}{\alpha^2 L_h^2 - 1} \times \left[\frac{(\frac{S_h L_h}{D_h} + \alpha L_h) - exp(-\alpha x_j)(\frac{S_h L_h}{D_h} cosh\frac{x_j}{L_h} + sinh\frac{x_j}{L_p})}{\frac{S_h L_h}{D_h} sinh(\frac{x_j}{L_h}) + cosh(\frac{x_j}{L_p})} - \alpha L_h exp(-\alpha x_j)\right] \tag{3.38}$$

where $L_{e,h}$ are the diffusion length for electrons and holes, respectively, which can be obtained from $L_{e,h} = \sqrt{D_{e,h}\tau_{e,h}}$. Following a similar process, the electron current density at the depletion edge $x = x_j + W_D$ can be obtained as

$$J_e = qD_e\left(\frac{dn}{dx}\right)_{x=x_j+W_D} = \frac{q\phi(1-R)\alpha L_e}{\alpha^2 L_e^2 - 1} exp\left[-\alpha(x_j + W_D)\right] \times \left\{\alpha L_e - \frac{\frac{S_e L_e}{D_e}[cosh(\frac{H'}{L_e}) - exp(-\alpha H')] + sinh(\frac{H'}{L_e}) + \alpha L_e exp(-\alpha H')}{\frac{S_e L_e}{D_e} sinh(\frac{H'}{L_e}) + cosh(\frac{H'}{L_e})}\right\} \tag{3.39}$$

where S_e is the surface recombination velocity at $x = H$. Due to the strong built-in electric field in the depletion region, the electron-hole pairs generated in this region has no time to recombine before they are swept out, thus the IQE is unity for photons absorbed in this region. And then the photocurrent generated in this region can be given by

$$J_{DR} = \int_{x_j}^{x_j+W_D} G(\lambda, x)dx = q\phi(1-R)exp(-\alpha x_j)[1 - exp(-\alpha W_D)] \tag{3.40}$$

The total current generated by the solar cell is the sum of the currents generated in the three regions. The IQE of the solar cell can be obtained from

$$IQE(\lambda) = \frac{J_h + J_e + J_{DR}}{q\phi[1 - R(\lambda)]} \tag{3.41}$$

3.7.2 Numerical results and comparison with PC1D

Table 3.1 shows the parameters of a typical silicon solar cell [37]. They are used to calculate the IQE by using the analytical model described in the previous section. And they are also input to PC1D to obtain the IQE. The results of these two methods are compared in Fig. 3.15.

$n_i(cm^{-3})$	$N_D(cm^{-3})$	$N_A(cm^{-3})$	$x_j(\mu m)$	$W_D(\mu m)$	$H(\mu m)$
1.5×10^{10}	5×10^{19}	1.5×10^{16}	0.5	0.28	450
$\tau_e(\mu s)$	$\tau_h(\mu s)$	$L_e(\mu m)$	$L_h(\mu m)$	$S_e(cm\bullet s^{-1})$	$S_h(cm\bullet s^{-1})$
10	0.4	164.68	7.23	1×10^{5}	1×10^{4}

Table 3.1: Parameters for a typical silicon solar cell.

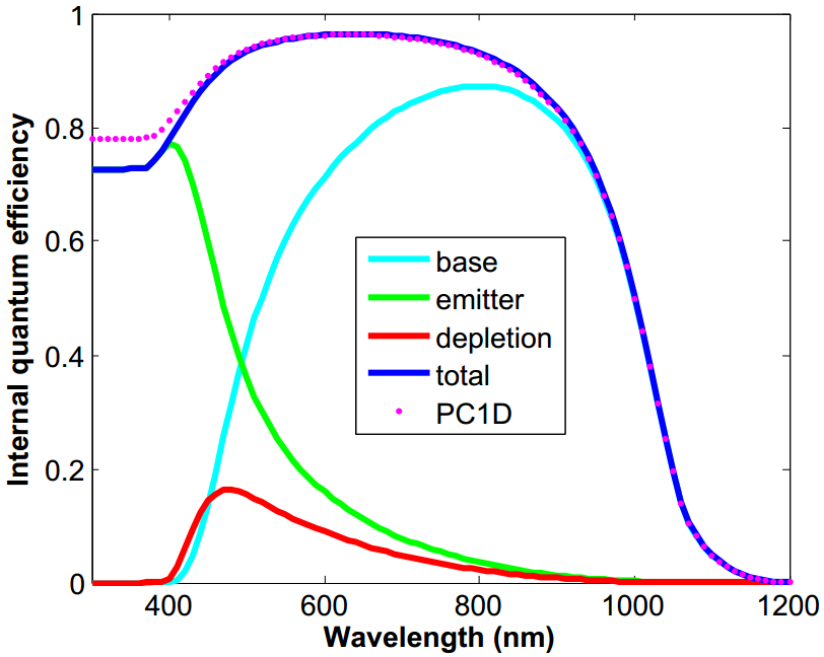

Figure 3.15: Modelling results of the IQE of the silicon solar cell.

From Fig. 3.15 one can see that the large energy photons are mainly absorbed in the n-type emitter, while the small energy photons are mainly absorbed in the p-type base. The contribution from the depletion region to the IQE is limited due to its limited width. It is apparent that the analytic model agrees well with PC1D except for the low wavelength part. This discrepancy is due to that the high doping effect, such as bandgap narrowing in the n-type emitter [38], is not considered in the analytic model.

To get a brief idea of the solar cell efficiency dependence on the thickness of silicon, PC1D is used to calculate the efficiency of silicon solar cells with parameters given in Tab. 3.1. The result is shown in Fig. 3.16. It is seen that the efficiency increases rapidly to 13% when the thickness of silicon increases from 10 to 50 μm. Then the increase rate slows down and reaches a plateau of

16%, which is the typical efficiency of a commercial silicon solar cell module (see, for example, [39]). Note that the silicon solar cells inside the module should have even higher efficiency, due to the losses such as mismatch loss [24] when connecting the constituent solar cells together. This indicates that a typical commercial silicon cell needs hundreds of micrometres of silicon to achieve efficient operation.

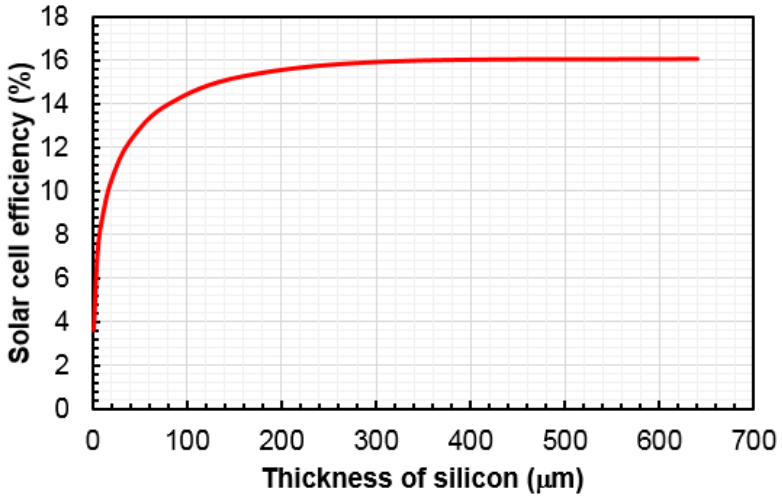

Figure 3.16: Solar cell efficiency dependence on the thickness of silicon.

3.8 Conclusion

This chapter introduces the light source and the working principle of single-junction solar cells. The efficiency limits for ideal single junction solar cells are also reviewed. It is also shown that the currently reported world record efficiency of a single-junction GaAs solar cell is close to the detailed balance limit given by S&Q. However, the practical problem is that the costs of solar cells are still high that hold back the widespread utilisation.

According to the assessment by the Department of Energy and Climate Change of UK, the average cost of installed solar panels is around £2100 per kWp from April 2013 to March 2014 [40], and the average cost of traditional electricity is around £0.16 per kWh (deduced from the data given by [41]). A simple estimation from these data reveals that the cost of solar panels is nearly ten times the cost of traditional electricity in UK.

Thus more effort is needed to find approaches to achieve low cost while maintaining high efficiency. The following chapters discuss our approaches via the use of fluorescent molecules.

Chapter 4 Literature Review of Fluorescent Solar Collectors

4.1 Introduction

The initial structure of fluorescent solar collectors proposed by Weber and Lambe (W&L) consists of a clear planar dielectric waveguide doped with fluorescent dyes [1], [42]. One or several of the four edge surfaces can be mounted with solar cells [43]–[46], the remained edge surfaces and the bottom surface are usually covered by mirrors. The fluorescent molecules absorb the incident solar radiation, and re-emits photons, i.e. fluorescence. Since the refractive index of the matrix is larger than the ambient air, most re-emitted photons are trapped inside the collector by total internal reflection (TIR) and finally collected by the edge solar cell.

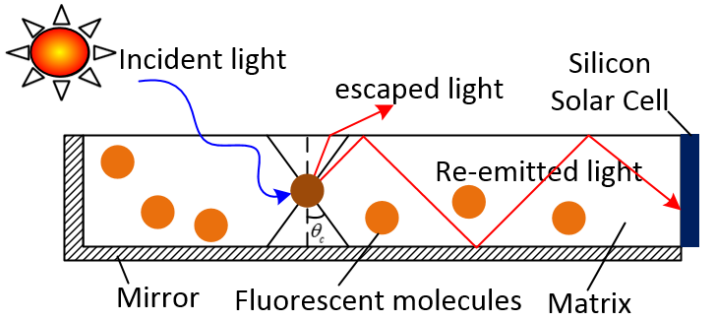

Figure 4.1: Cross-sectional view of a typical fluorescent solar collector.

There are several advantages of collectors [2]–[4]: both direct and diffuse radiation can be captured; the extra energy of the short wavelength photons that deteriorates the performance of solar cells can be dissipated as heat inside the collector; multiple dyes can be doped in collectors to potentially harvest the whole spectrum of solar radiation; multiple stage collectors doped with different dyes in each stage can be covered with spectral response matched solar cells to achieve high efficiency; edge solar cells with top contact outside of the photon-collecting area could be used to eliminate the loss by contact shadowing. W&L first introduced collectors in 1976 [1], and the research on fluorescent solar collectors was booming in the following decade [28], [47], [48]. The research interests were reduced during the 1990s due to the lack of suitable materials, especially fluorescent dyes. Recently, new dyes such as BASF Lumogen dyes [49], quantum dots [50], lanthanide complexes [51] and novel concepts such as photonic filters [52], dye alignments [53], zeolites [54] emerge, the research on collectors gains interests again.

4.2 Parameters to characterise collectors

To compare the practical performance of fluorescent solar collectors, we need to consider the different geometric shapes of the collectors and different type and number of edge solar cells.

The parameters to characterise the performance of a collector are the geometric gain, optical efficiency and photon flux gain.

4.2.1 Geometric gain

Fluorescent solar collectors can concentrate sunlight, because photons incident on a large area top surface are guided to a small area solar cell. The geometric gain is given by

$$G = \frac{A_t}{A_e} \tag{4.1}$$

where A_t is the area of the top surface, and A_e the area of the edge surfaces that are mounted with solar cells.

4.2.2 Optical efficiency

The optical efficiency of a collector is the ratio of the number of the photons per unit time collected at the edge and that for the incident photons at the top surface [55]. It can be written as

$$\eta_{opt} = Q_A \cdot Q_C \tag{4.2}$$

where Q_A is the absorption efficiency, Q_C is the collection efficiency of the absorbed photons at the edge. Other definitions [1], [42] (not adopted here) insert the fluorescent quantum yield into Eq. (4.2).

4.2.3 Photon flux gain

Photon flux (number of incident photons per unit area per unit time) seen by the edge solar cell coupled at the collector edge is larger than the flux seen by the solar cell under direct illumination. This gain is defined as the photon flux gain, which equals to the product of the geometric gain and the optical efficiency [56]

$$\Phi_G = G \cdot \eta_{opt} \tag{4.3}$$

4.3 Practical Performance of collectors

Although the theoretical energy conversion efficiency of a silicon solar cell with a fluorescent solar collector can reach 90% of the maximum efficiency of an ideal silicon solar cell given by the Shockley and Queisser detailed balance limit [6], the achieved highest overall power conversion efficiencies of collectors with different edge solar cell configurations shown in literature are all below the 10% industrial application benchmark [43]–[45]. This is due to several loss mechanisms discussed below.

4.4 Loss mechanisms of collectors

4.4.1 Dye losses

The fluorescence quantum yield of dyes used in collectors can be less than unity; a part of the absorbed photons will then be lost non-radiatively as heat. The reduction of quantum yield can be caused by, for example, by concentration quenching at high dye concentrations or photo-bleaching due to absorption of UV radiation.

4.4.2 Top escape cone loss

Most of the fluorescent photons emitted by the dye are trapped by TIR and collected by the edge solar cell, as shown by the red ray 1 in Fig. 4.2. Other photons escape from the collector via the surface escape cones, as shown by the blue ray 2. By using the Snell's law at the collector/air interface, the critical angle for total internal reflection is given by

$$\theta_c = \arcsin(1/n_c) \tag{4.4}$$

where n_c is the refractive index of the matrix material.

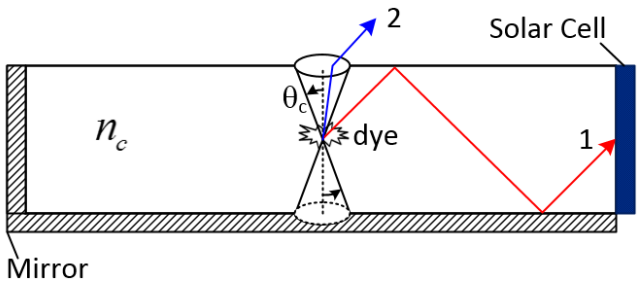

Figure 4.2: Escape cone loss in a typical collector.

By assuming the fluorescence emitted by the dye to be isotropic and neglecting the reabsorption of the photons emitted inside the loss cones, the fraction of photons lost through the top escape cone is given by

$$P = \frac{\int_0^{2\pi} d\varphi \int_0^{\theta_c} \sin\theta d\theta}{\int_0^{2\pi} d\varphi \int_0^{\pi/2} \sin\theta d\theta} = 1 - \cos\theta_c \tag{4.5}$$

Substituting Eq. (4.4) to Eq. (4.5), the lost fraction becomes

$$P = 1 - \sqrt{1 - 1/n_c^2} \tag{4.6}$$

Clearly, the escape cone loss can be decreased by using high refraction index matrix materials. For PMMA matrix with refractive index $n_c = 1.5$, the critical angle for total internal reflection is $\theta_c \approx 41.81^0$, and the top escape cone loss is $P = 25.46\%$.

4.4.3 Loss in fluorescence reabsorption

Fluorescence reabsorption is due to the overlap of the absorption and the emission spectra of the dyes doped in collectors. Figure 4.3 shows the absorption and top fluorescence spectra of a thin film collector doped with Rhodamine 101 dye (concentration of 24×10^{-3} mol/L in PMMA). It is seen that a significant fraction of fluorescence are reabsorbed. For every reabsorption event, there is probability for non-radiative losses resulting from the non-unity fluorescent quantum yield and the loss of re-emitted photons through the top escape cone.

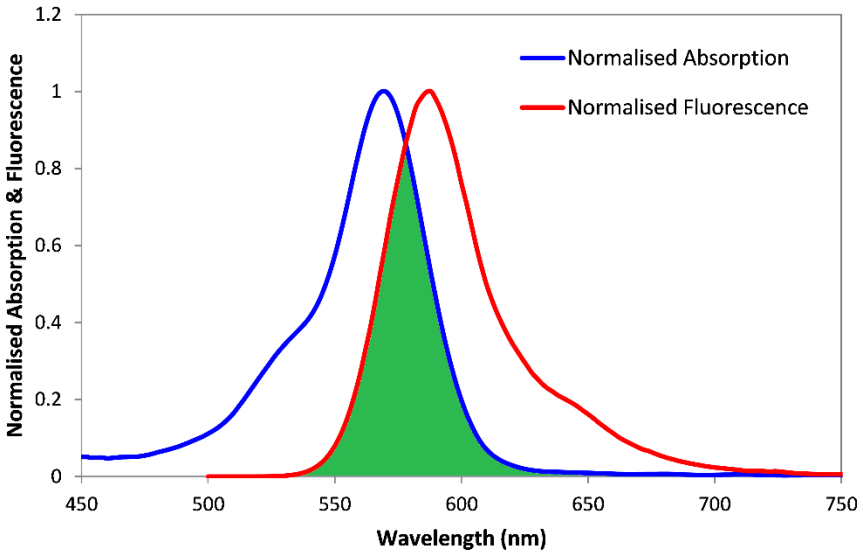

Figure 4.3: Normalised absorption and fluorescence spectra of a thin film collector.

4.4.4 Loss in matrix

The matrix doped with dyes is usually not perfectly homogeneous for light propagation. The photons trapped inside the collector may be scattered and absorbed within the collector [57]. Further, both the top and bottom surface of the collector need to be perfect flat to guarantee effective trapping of fluorescent photons by TIR. And the top surface of the collector needs to apply ARC to reduce reflection loss.

4.4.5 Typical practical losses

The first typical practical loss is due to the imperfect coupling of the edge solar cell to the collector (i.e an air gap between collector and the cell). As the refractive index of the matrix is higher than air, only a fraction of photons emitted inside the right edge escape cone can escape from the collector and be captured by the imperfect coupled edge solar cell [58]. As shown in Fig. 4.4, the red ray represents the photons escape from the right edge escape cone, and the blue ray represents the photons trapped by TIR and thus cannot be captured by the edge solar cell. This typical loss is discussed further in the next chapter. The second typical practice loss is

due to the imperfect reflection at the mirror/collector interface. A part of the photons might escape the collector via the left edge escape cone and will not be reflected back by the mirror, as shown by the green ray in Fig. 4.4. If the collector edge is not well polished, this loss cannot be neglected.

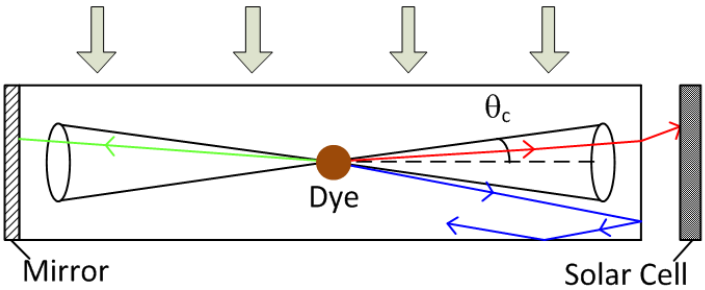

Figure 4.4: Typical practical losses of collectors.

4.5 Materials for collectors

A good fluorescent solar collector requires the dye to have the following features [59]: the absorption spectrum of the dye should have good spectra coverage and high absorption of the solar radiation; the dye should have a good fluorescent quantum yield; the emission spectrum of the dye should match the spectral response range of the edge solar cells, and the dye should have a good photo-stability.

4.5.1 Matrix materials

The matrix material used in fluorescent solar collectors needs to be optically transparent with low absorption and low scattering [57]. Another requirement is that dyes can be easily doped in the matrix material. Due to their high solubility of organic dyes, many organic polymers such as PMMA, MMA and PVC are good candidates for the matrix materials. And PMMA is the most commonly used and studied material due to its high transparency, high durability and relative low cost [60], [61]. Inorganic glasses are another type of matrix materials. These optically transparent glasses have larger refractive indices than the organic materials, thus the top surface escape cone loss can be decreased. But the costs of these glasses are higher than the organic matrix materials, and more complicate process are needed to dope these inorganic glasses with dyes [62]–[64].

4.5.2 Organic dyes

Organic dyes have high absorption coefficients and the fluorescent quantum yield of some dyes are nearly unity [49], [65]–[67]. These features make organic dyes ideal candidates for collectors. Commonly used organic dyes are the laser dyes which are used in chemical lasers, e.g. Coumarin, DCM, Rhodamine and Oxazine [68]. The BASF Lumogen dyes are popular among the recently

reported collectors because of their great photo-stability, heat-stability [61], and near unity fluorescent quantum yield in PMMA matrix [69]. They can also be readily incorporated in plastic matrix [55]. The main problems for organic dyes are the small Stokes shift and poor coverage of the solar spectrum. These problems could be solved by doping the collector with multiple dyes. Figure 4.5 shows the measured absorption and fluorescence spectra of the BASF Lumogen dyes in PMMA matrix as well as the AM1.5 solar spectrum, which indicates that multiple dye systems have better spectral coverage and it is able to realise energy transfer between different dyes to decrease the negative effect of small Stokes shift.

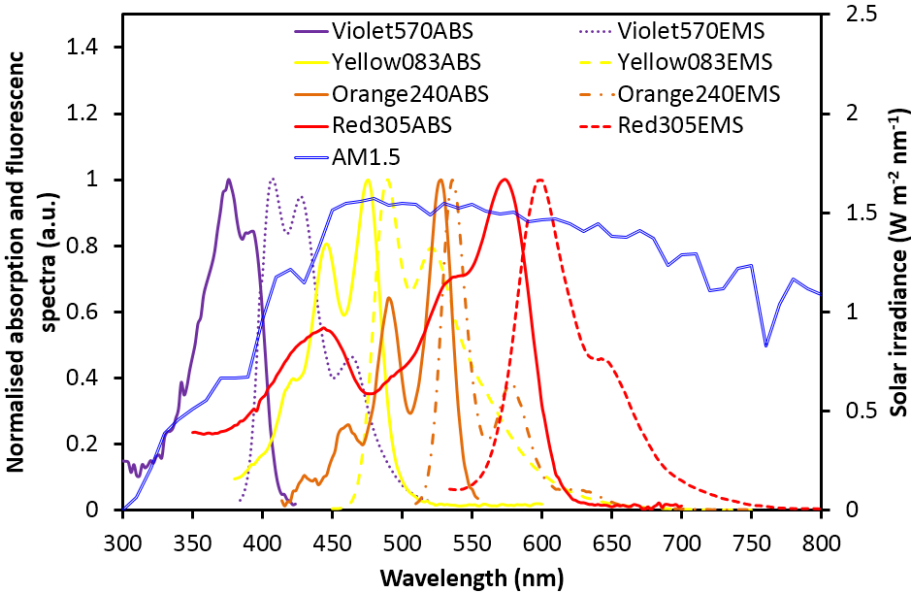

Figure 4.5: Fluorescent spectra of BASF dyes and AM1.5 solar spectrum.

However, a simple mixture of these dyes cannot achieve efficient energy transfer due to strong quenching between the donor dye molecules. A more effective approach is to incorporate organic dyes in zeolites [54]. The crystals of zeolite L are cylindrically shaped porous aluminosilicates featuring hexagonal symmetry. A large amount of strongly absorbing donor and very little emitting acceptor can be filled in the porous nano-channels as shown in Fig. 4.6, and the molecular excitation can spatially hop along the axis of the nano-channel with concomitant fluorescence spectrum shift from the donor to the acceptor. Via the use of this structure, fluorescence quenching between the donor molecules can be reduced significantly, and efficient resonance energy transfer can be achieved to effectively solve the reabsorption problem. The photo-stability of the dye molecules is also considerably improved because of confinement in the nano-channels. The absorption wavelength range that has been covered so far ranges from near-UV to 700 nm.

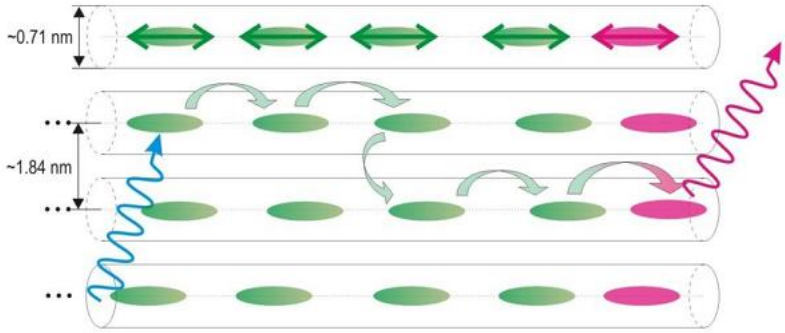

Figure 4.6: Energy transfer in zeolites [54].

4.5.3 Inorganic dyes

Common inorganic dyes are based on rare earth ions such as Nd^{3+}, Yb^{3+}, Eu^{3+}, Tb^{3+}, Cr^{3+}, Sm^{3+}, Gd^{3+}, Dy^{3+} , Ho^{3+} and UO^{22+} etc. [62]–[64], [70]. The main advantage of inorganic dyes is the high thermal resistivity, and many of them are free from reabsorption. For example, the Nd^{3+} doped laser glass has strong absorption bands in the 500-900 nm wavelength range, and luminesces at 1060 nm. At this wavelength, however, most of the commercial available solar cells have low power conversion efficiency. The fluorescent quantum yield is reported to be in the range of 50-75% [1], [42]. The main problem of inorganic dyes is that the absorption coefficients are low in most bands of the solar radiation spectrum, so only part of the solar spectrum can be used. The fluorescent quantum yield of these inorganic dyes vary greatly from 10% to 90%, depending on the matrix material [71]. Cr^{3+} has large spectral absorption around 450 nm and 650 nm, but the fluorescent quantum yield of Cr^{3+} is fairly low with highest efficiencies of 17.5% in silicate glasses and 14% in phosphate glasses. Cr^{3+} has been reported to be co-doped with Yb^{3+} to increases light absorption and efficient energy transfer has been archived [64], [70]. However, Yb^{3+} has similar disadvantage as Nd^{3+} since the emission peak of Yb^{3+} is around 970 nm. Thus collectors only doped with these inorganic dyes are unlikely to have good power conversion efficiency.

4.5.4 Lanthanide complexes

The advantages of organic and inorganic dyes can be combined [51], [71], [72]. The most reported combinations are the lanthanide complexes synthesised from organic ligands and lanthanide ions such as Nd^{3+}, Eu^{3+}, Tb^{3+} and Yb^{3+}. As shown in Fig. 4.7, the organic ligands are used as an antenna, which efficiently absorbs the incident light and then transfer the absorbed energy to the lanthanide ions via resonance energy transfer.

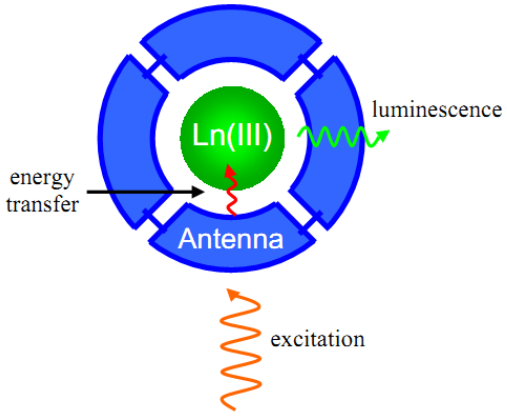

Figure 4.7: Operation principle of lanthanide complexes [71]].

Via the use of organic ligands, the low absorption efficiency of the inorganic lanthanide ions discussed in the previous section can be improved. These lanthanide complexes exhibit intense and narrow emission bands due to the long-lived excited states (milliseconds scale) of the lanthanide ions and also show little dependence on the ligands [51]. There is no overlap between the absorption spectrum of the ligand and the emission spectrum of the lanthanide ions, which makes them good candidates for collector dyes. The most suitable complex is made from the Eu^{3+} ions, which emits around 620 nm and an overall fluorescent quantum yield of up to 85% in a PMMA matrix has been reported [72]. The main disadvantage of those complexes is their poor thermal and chemical stability. For practical application a protective matrix is needed, e.g. zeolites [54], sol-gel-derived glass [73] and porous nanoparticles [74].

4.5.5 Quantum dots

Using quantum dots as fluorescent dyes is a novel solution that emerged in recent years [50]. Quantum dots are nanometre-sized crystallite semiconductors, which can be produced by several cost effective methods [75]. The fluorescent quantum yield for CdSe/CdS hetero-structure quantum dots over 80% has been reported [76]. The possible advantage of using quantum dots is that the fluorescence spectrum could be tuned by changing the size and the size distribution of the quantum dots [77]. Thus collectors using quantum dots could be optimised to match the spectra response of the edge solar cell. Another advantage for quantum dots over organic dyes is the broad absorption spectrum. However, the current commercially available quantum dots have the disadvantages of large overlaps between the absorption and emission spectra and low fluorescent quantum yield [78]. The currently reported highest experimental optical efficiency of the collectors doped with PbS quantum dots is only 12.6% [75]. Recently, Mn^{2+} doped ZnSe nanocrystals were reported to have zero-reabsorption [79]. This is achieved by energy transfer from excited ZnSe nanocrystals to Mn^{2+} ions. And optical efficiency

as high as 40% has been measured in the absorption range (360 - 440 nm) of ZnSe nanocrystals. However, due to the large bandgap of ZnSe nanocrystals, insufficient solar radiation is absorbed. Using other low bandgap nanocrystals such as CdSe or InP is promising, but the doping of emitters such as Mn^{2+} into these nanocrystals are challenging. Quantum dots are promising providing that the high reabsorption and low fluorescent quantum yield problems are solved.

4.6 Structures of collectors

Levitt and Weber were the first to report fabricated fluorescent solar collectors with simple structures of a square glass or a square PMMA [42]. The efficiencies of these collectors were fairly low. In order to improve the performance, various novel approaches are applied and they are discussed below.

4.6.1 Stack collectors

Goetzberger and Wittwer were the first to report stack collectors [28]. The concept of stack collectors is to capture the split solar spectrum with spectra matched solar cells. This concept is similar to tandem solar cells, but stack collectors do not have the need for tunnel diodes and the current limitation problems. With this structure more photons of the solar spectrum can be converted to electricity. The theoretical efficiency of a four stage stack collector (edge mounted with Ge, Si, GaAs and an alloy semiconductor with an energy gap of 2eV, respectively) given by Goetzberger exceeded 30% [80]. However, the practical efficiencies are significantly lower due to the low efficiency of each single-stage collector [44].

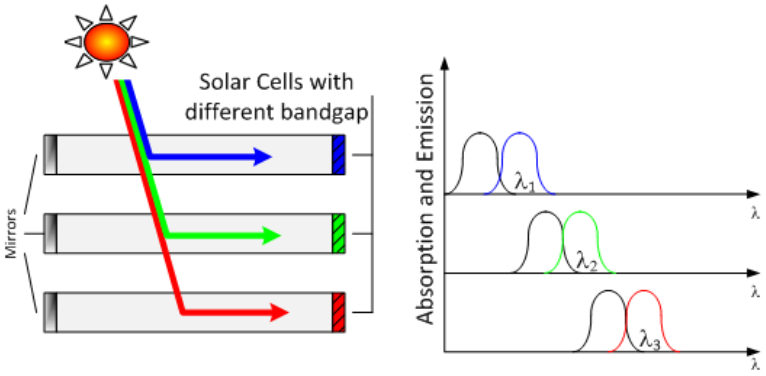

Figure 4.8: A stack collector and fluorescence spectra of each single-stage collector.

4.6.2 Thin film collectors

Rapp and Boling [81] were the first to report collectors consisting of a thin fluorescent film deposited on an un-doped substrate with a similar refractive index. The thin active layer absorbs incident light and re-emit photons, which can be trapped in the substrate by TIR, seemingly without reabsorption. It has also been suggested that thin film collectors have the advantage of reduced reabsorption over homogeneously doped collector plates, as reabsorption only occur

in the thin active layer [81]–[83]. It has been shown however, that the gain in the path length of the substrate is compensated by the reabsorption loss within the high dye concentration active layer [84]. This conclusion has been confirmed experimentally as no significant difference were found between thin film collectors and collector plates with nearly the same absorbance [85]. Nevertheless, thin film collectors are easier to fabricate, as thin film can be deposited on a wide range of substrates relatively easily, e.g. by spincoating [55]. Also high quality optical glasses can be chosen to minimise the absorption and scattering by the matrix. In addition, due to the high concentrations required for resonance energy transfer to occur, thin film collectors are most suitable for multiple dye systems [86].

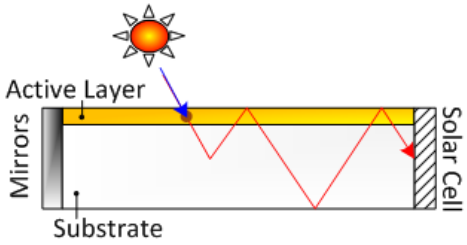

Figure 4.9: Cross-sectional view of a thin film collector.

4.6.3 Photonic collectors

The idea of eliminate the top escape cone losses by the application of photonic filters were first proposed by Richards [5]. Photonic collectors usually have a band stop filter layer on the top surface of a traditional collector, as shown in Fig. 4.10.

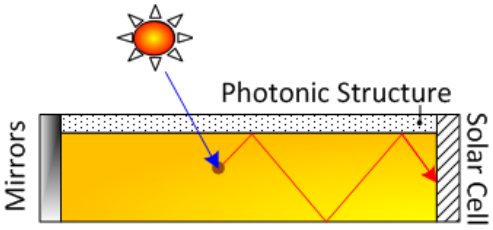

Figure 4.10: Cross-sectional view of a photonic collector.

The band stop filter transmits the short wavelength photons but reflects the long wavelength photons. Thus the re-emitted long wavelength photons can be trapped in the collector without escape cone loss. With the use of this kind of photonic filters, the power conversion efficiency of a collector could reach the thermodynamic efficiency limit of a single-junction solar cell [6]. Figure 4.11 shows the spectral reflectance of a typical photonic filter fabricated at Fraunhofer ISE, the absorption and photoluminescence spectra are for a collector doped with BA 856 dye [87].

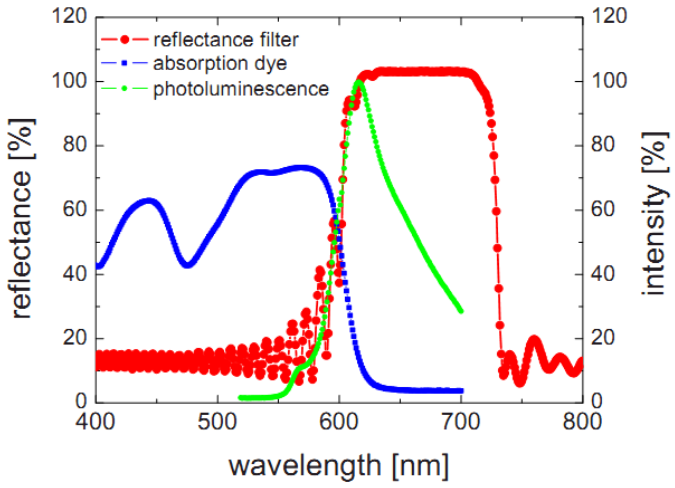

Figure 4.11: Spectra reflectance of a typical photonic filter [87].

With a photonic band edge filter applied, the power conversion efficiency of a collector increased from 2.6% to 3.1%, and the reason for this improvement is that more than 75% of the loss cone loss are reduced [44].

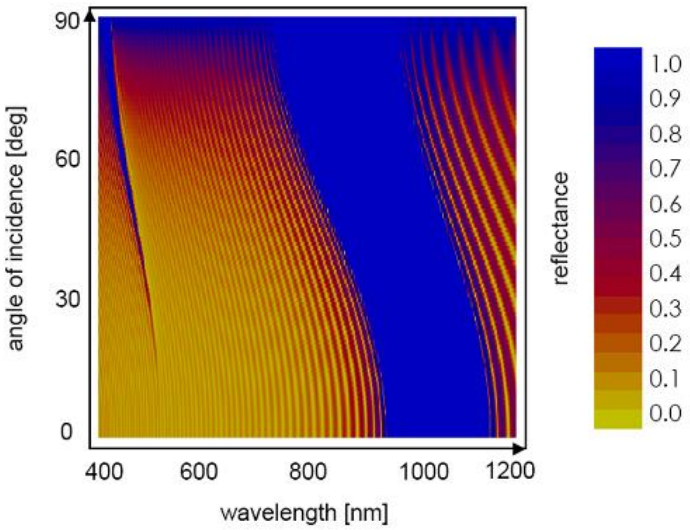

Figure 4.12: Angular dependent reflectance of a typical photonic filter [52].

The recently fabricated photonics structures are optimised with normal incidence of light. When the incident angle of light increases, the reflection threshold shifts to low wavelength range, as seen from Fig. 4.12. Thus after the application of this kind of photonic filter on the collector, a part of the high energy photons which can be absorbed is reflected back by the photonic filter. Furthermore, the practical fabricated photonic filters have non-unity reflection peaks and if these filters are optically coupled to collectors, light trapping by TIR (without the application of photonic filter) will be deteriorated and consequently the effect on the light guiding efficiency

to the edge solar cell would be negative [87]. Thus photonic filters still need further optimisation to be applied in a photonic collector.

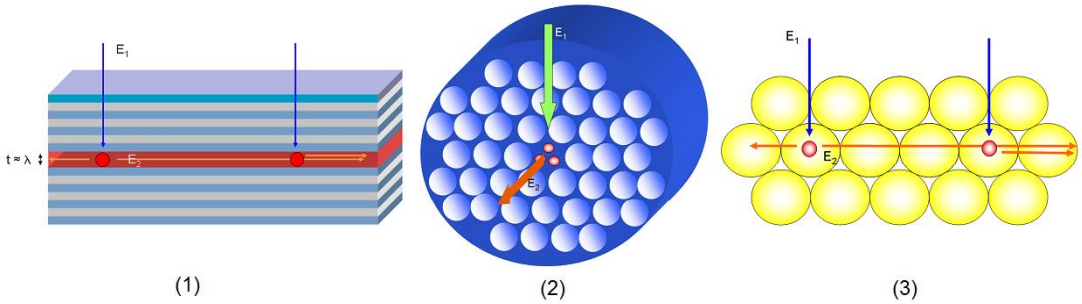

Figure 4.13: 'Nano-Fluko' structures [88].

More advanced structures, as shown in Fig. 4.13, are proposed to incorporate dyes to photonic structures ((1) Bragg stack, (2) photonic fibre, (3) opal) to form a 'Nano-Fluko' to restrict angular emission [88]. Thus the fluorescent photons are suppressed to propagate in the direction towards the edge solar cell to minimise path length dependent losses such as reabsorption related losses and loss due to absorption by the matrix. Although the fabrication process will be much more complicated, Nano-Fluoks bear the promise to surpass the efficiency of traditional collectors.

4.6.4 Dye alignment

An alternative to photonic structures to reduce the escape cone loss is to restrict fluorescence emission predominantly into directions away from the escape cones. This can be achieved by orientation alignments of the dyes which absorb and emit photons as electric dipoles [89]–[93].

Figure 4.14: (1) Random, (2) homeotropic, (3) planar and (4) titled dye alignments.

Liquid crystal is a good matrix material that can align dye in several orientations: random (isotropic), homeotropic, planar and titled as shown in Fig. 4.14. And then the doped liquid crystals was deposited on PMMA waveguides [53]. The planar alignment showed the emission from the edge parallel to the dye alignment was favoured over the emission from the edge perpendicular to the dye alignment by up to 60%, and the emission from the parallel edge exceeds the emission from the randomly aligned collector with the same light absorption by up to 30% [90]. The homeotropic alignment showed greatly reduced top escape cone loss, but this does not lead to a significant increase in edge output since the fluorescence was emitted in such

favoured directions that the probability of reabsorption loss increased. Further, homeotropic alignment will lead to the decrease of absorption due to the orientation of the absorption dipoles [53]. An external diffuser was placed on the top of the collector to alleviate the weak absorption [92]. Tilted alignment was suggested to combine the reduced escape cone losses of the homeotropic alignment and the increased edge emission of the planar alignment [53], but no experimental results has been reported. Recently, Macqueen and co-workers used a square-symmetric porphyrin sensitiser, which can effectively absorb radiation at normal incidence and transfer energy to a nearby homeotropic-aligned emitter in a liquid crystal host [94]. Highly polarised emission has been observed in their proof-of-concept experiments, but the energy transfer efficiency of this process is unknown. Overall, dye alignment is a good way to reduce escape cone losses, but this will deteriorate the advantage of collectors for diffuse radiation utilisation. Using random orientated molecules to sensitise homeotropic-aligned molecules represents a promising approach, but the energy transfer process should be efficient.

4.7 Models and Techniques for the analysis of collector performance

4.7.1 Weber and Lambe's model

The collector structure modelled by W&L is shown in Fig. 4.15. It's assumed that three edges are covered with mirrors with unity reflectance and the remained edge is mounted with a solar cell.

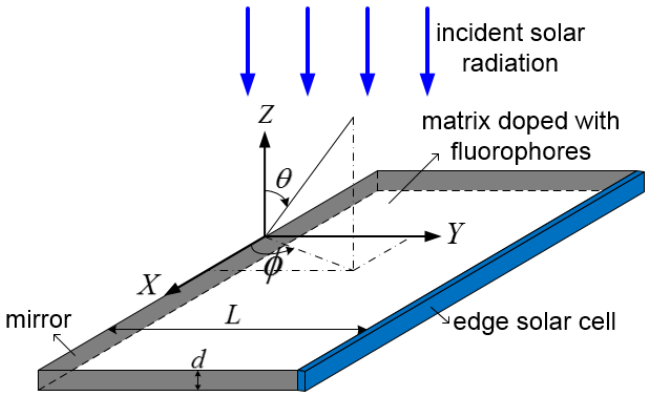

Figure 4.15: Collector modelled by W&L [1].

W&L gave the absorption efficiency as

$$Q_A = \int_0^{\lambda c} d\lambda \cdot N(\lambda) \cdot \{1 - \exp[-\alpha(\lambda) \cdot 2d]\} \Big/ \int_0^{\lambda c} d\lambda \cdot N(\lambda) \qquad (4.7)$$

where $N(\lambda)$ is the photon flux in the solar spectrum, λ_c the cut-off wavelength of the edge solar cell, $2d$ the absorbing length which is twice the thickness of the collector when the bottom of the collector is covered with a mirror, and $\alpha(\lambda)$ the absorption coefficient of the dye. They also give an analytical model for the collection efficiency of a planar collector

$$Q_{c1} = (1-P)\{1-r(\lambda)\} \tag{4.8}$$

where P is the fraction of photons lost in the top surface escape cone, as defined in Sec. 4.4.2, and $r(\lambda)$ is the spectral reabsorption probability. The collection efficiency in Eq. (4.8) only counts the first generation photons [89], in other words, photons that have not been reabsorbed. At the same time, all photons emitted in the top escape cone are considered as loss. Nevertheless, the model of W&L can be employed to calculate $r(\lambda)$. Applying Beer-Lambert's law, the generalised form for $r(\lambda)$ can be cast as [58]

$$1-r(\lambda) = \int_{(V_0)} \frac{dV}{V_0} \int_{(\Omega_0)} \frac{d\omega}{\Omega_0} e^{-\alpha(\lambda)l} \tag{4.9}$$

Where V_0 is the volume of the collector, Ω_0 the solid angle which equals to $4\pi(1-P)$, and l the path length travelled by the photon. W&L evaluated Eq. (4.9) and gave the results as

$$1-r(\lambda) = \frac{1}{4\pi(1-P)} \int_0^{\pi} d\phi \int_{\theta_c}^{\pi-\theta_c} \frac{\sin\theta\sin\phi}{\alpha(\lambda)L} \left\{1-\exp\left[\frac{-2\alpha(\lambda)L}{\sin\theta\sin\phi}\right]\right\} \sin\theta d\theta \tag{4.10}$$

where θ and ϕ are the spherical angles defined in Fig. 4.15, and θ_c the critical angle for TIR in the collector matrix. This result is for all the photons arrive at the edge surface or seen by a fully optically coupled edge solar cell in experiments. The next chapter uses Eq. (4.9) to calculate $r(\lambda)$ for the fluorescent photons emitted in the edge escape cone, which is the observed photon flux in spectroscopic measurements.

4.7.2 Batchelder and Zewail's model

Batchelder and Zewail (B&Z) further developed the collection efficiency model by W&L [89].

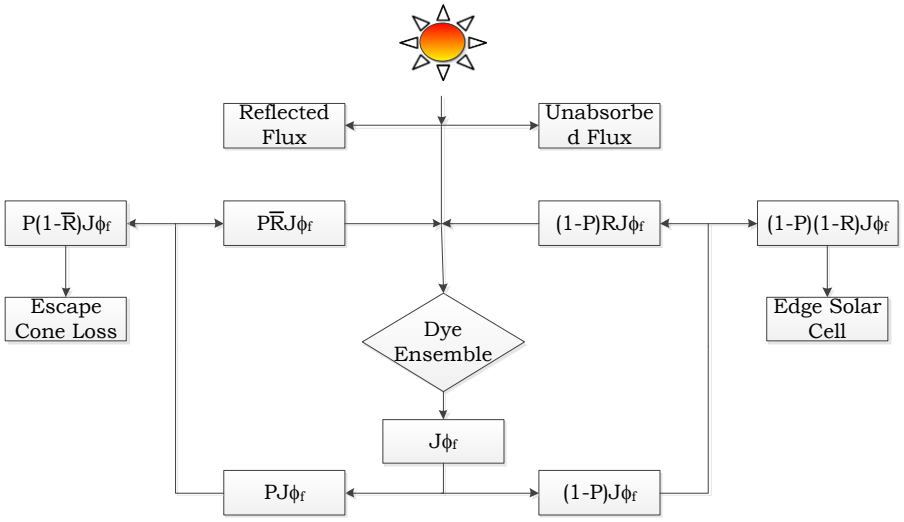

Figure 4.16: Photon flow chart in a collector [89].

They distinguished the photons collected by the edge solar cell by the different generations of photons. The order of generation denotes the number of times of the photons captured by the fluorescent molecules. Figure 4.16 shows the photon flow channels available in a collector, where J denotes the absorbed incident energy, ϕ_f fluorescent quantum yield, P the fraction of photons emitted in the escape cone, and R and $\bar{R}$ the reabsorption probability of photons emitted outside and inside the escape cone, respectively. Photons trapped in the collector will undergo multiple absorption and emission. The total collection efficiency is the sum of the collection efficiency of each generation photons, given by

$$Q_c = Q_{c1} + Q_{c2} + Q_{c3} + ... \tag{4.11}$$

In the model of B&Z the above sum is given by a geometry series

$$\begin{aligned} Q_c = {} & (1-R)(1-P)\phi_f + \left[(1-R)(1-P)\phi_f\right]\cdot\left\{\left[\bar{R}P + (1-P)R\right]\phi_f\right\} + \\ & \left[(1-R)(1-P)\phi_f\right]\cdot\left\{\left[\bar{R}P + (1-P)R\right]\phi_f\right\}^2 + \\ & \left[(1-R)(1-P)\phi_f\right]\cdot\left\{\left[\bar{R}P + (1-P)R\right]\phi_f\right\}^3 + ... \end{aligned} \tag{4.12}$$

The first term equals to the first generation collection efficiency given by W&L. The above series can be summed up to be

$$Q_c = \frac{(1-R)(1-P)\phi_f}{1-\left\{\bar{R}P + (1-P)R\right\}\phi_f} \tag{4.13}$$

From Eq. (4.13) one can see that the collection efficiency of the collector can be obtained once the reabsorption probability and fluorescent quantum yield of the dye are known.

4.7.3 Markvart's model

Markvart obtained identical results as B&Z via a much simpler approach by considering photon balance in the collector [55]. The photon balance in the collector is given by

$$\dot{N}_{abs} = \dot{N}_{loss} + \dot{N}_{work} + \dot{N}_{nr} \tag{4.14}$$

where $\dot{N}_{abs}$ is the photon flux absorbed by the collector from the incident solar radiation, $\dot{N}_{loss}$ the photon flux lost through the top escape cone, $\dot{N}_{work}$ the useful photon flux illuminates the edge solar cell, and $\dot{N}_{nr}$ the non-radiative de-excitation rate of the luminescent species. Assuming the fluorescence emitted to be isotropic, $\dot{N}_{loss}$ and $\dot{N}_{work}$ are given by

$$\dot{N}_{loss} = P(1-\bar{R})N^* / \tau_{rad} \tag{4.15}$$

$$\dot{N}_{work} = (1-P)(1-R)N^* / \tau_{rad} \tag{4.16}$$

where R and $\bar{R}$ are the probabilities of reabsorption for photons within and outside the escape cone, respectively, τ_{rad} the radiative lifetime of the fluorescent molecules, and N^* the number of fluorescent molecules in the excited state. The non-radiative de-excitation rate is given by

$$\dot{N}_{nr} = N^* / \tau_{nr} \tag{4.17}$$

where τ_{nr} is the non-radiative lifetime of the dye molecules. The efficiency of collection of fluorescence at the edge is given by

$$Q_C = \dot{N}_{work} / \dot{N}_{abs} \tag{4.18}$$

Substituting Eqs. (4.14), (4.15), (4.16) and (4.17) into Eq. (4.18) yields

$$Q_C = \phi_f \frac{(1-P)(1-R)}{1-\left\{(1-P)R + P\bar{R}\right\}\phi_f} \tag{4.19}$$

The collection efficiency given by B&Z in Eq.(4.13) is reproduced here via much simpler derivation. The absorption efficiency Q_A is given by

$$Q_A = \dot{N}_{abs} / I_o \tag{4.20}$$

where I_o is the incident photon flux. Then the optical efficiency is given by

$$\eta_{opt} = \frac{\dot{N}_{work}}{I_o} = \frac{\dot{N}_{abs}}{I_o}\frac{\dot{N}_{work}}{\dot{N}_{abs}} = Q_A Q_C \tag{4.21}$$

A normalised first generation fluorescence is defined by

$$\int f_1(\lambda) d\lambda = 1 \tag{4.22}$$

Then Q_C can be written as

$$Q_C = \int \chi(\lambda)\, f_1(\lambda) d\lambda \tag{4.23}$$

where $\chi(\lambda)$ is the spectral fluorescence collection efficiency given by

$$\chi(\lambda) = \frac{\phi_f (1-P)}{1-\left\{(1-P)R + P\bar{R}\right\}\phi_f}\left\{1-r(\lambda)\right\} \tag{4.24}$$

Here $r(\lambda)$ is the spectral reabsorption probability, which is discussed further in next chapter.

4.7.4 Chatten's model

Chatten [76] gave a thermodynamic model for fluorescent solar collectors by applying detailed balance arguments to relate the absorbed light to the spontaneous emission using self-consistent three-dimensional fluxes. The model was derived by employing the radiative transfer method and the radiation is considered as consisting simply of forward (+) and backward (-) streams.

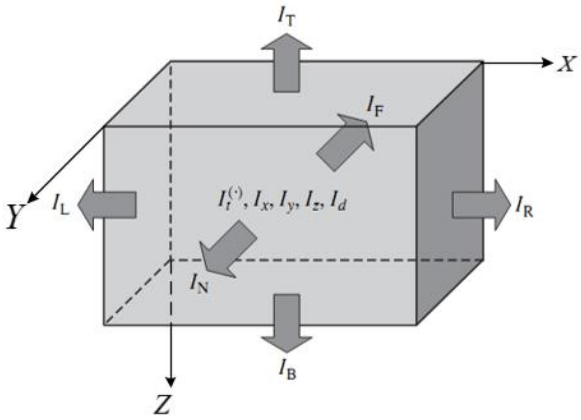

Figure 4.17: Trapped and escaping photon streams of a collector [76].

The luminescent fluxes propagating in collectors is decreased due to absorption by the collector comprising fluorophores doped inside and increased due to fluorescence emission from the fluorophores, applying the radiative transfer equations yields

$$\mp\frac{\partial I_{x,y,z}^{(\pm)}}{\partial x,y,z}=N\sigma_a(\nu)I_{x,y,z}^{(\pm)}\mp N\sigma_e(\nu)B(\nu) \tag{4.25}$$

where $I_x^{(\pm)}$, $I_y^{(\pm)}$, $I_z^{(\pm)}$ are the escaping luminescent fluxes propagating in the positive and negative X, Y and Z directions, respectively, N the density of fluorophores, $\sigma_a(\nu)$ the absorption cross section of the collector comprising the fluorophores, $\sigma_e(\nu)$ the absorption cross section of the fluorophores and P the fraction of fluorescence lost in the escape cone and given by Eq. (4.6), and $B(\nu)$ the brightness of the radiation field in the collector in thermal equilibrium and given by the generalised Planck's law in the form of

$$B(\nu)=\frac{I(\nu,T,\mu)}{h\nu}\times 4\pi=\frac{8\pi n^2\nu^2}{c^2}\frac{1}{\mathrm{e}^{\frac{h\nu-\mu}{k_BT}}-1} \tag{4.26}$$

where n is the refractive index of the collector and μ the chemical potential of the photon. The chemical potentials at different positions were obtained by the detailed balance within the collector

$$F(\mu) = \int dv \sigma_e(v) I_c(v) - \int dv \frac{\sigma_e(v)}{\phi_f} B(v, x, y, z) = 0 \quad (4.27)$$

where ϕ_f is the fluorescent quantum yield of the fluorophores, I_c the total radiation field. Equation (4.27) can only be solved numerically to obtain the chemical potential. Substituting Eq. (4.26) into Eq. (4.25), a set of analytical expressions for the luminescent fluxes propagating in three different directions can be obtained. Applying proper boundary conditions at the surfaces of the collector, the photon fluxes outside the collector can be obtained.

This model was used to predict the luminescence spectra from the top and bottom surface of collectors which were made from acrylic matrix doped with CdSe/CdS quantum dots [76] or polyacrylate Plexit 55 matrix doped with Bayer Fluorescent Red and Yellow coumarin dyes [95]. The modelling results for the former system show good agreement with experimental observed results, whereas for the latter system the modelling results can only predict correct luminescent peaks. And for both systems, only normalised luminescent spectra were shown.

4.7.5 Ray tracing

Several groups reported the technique to simulate the operation of collectors via the aid of computational analysis. Monte Carlo ray tracing has been carried out to get the efficiency of a collector [96]; Tracepro (Lambda Research) has been used to study the reabsorption probability for collectors with different geometry shapes [97]; Optisworks (Optis, France) has been used to model the power density at the edge surface of collectors [98]. The main advantage of computer based ray tracing is that the performance of collectors can be studied more realistically and readily. However, the ray tracing codes and algorithms are usually long and time-consuming to build up.

4.7.6 Model comparison

W&L built up the fundamentals for collector modelling, but their model only considered the first generation fluorescence. B&Z and Markvart improved the model of W&L, and gave out identical collection efficiency for absorbed photons. Especially, the model of Markvart closely related with experimental parameters, i.e. the spectral reabsorption probability. This analytic model can be verified with experimental results and the following chapter uses this model to characterise photon reabsorption in collectors.

4.8 Conclusion

This chapter reviews the development of fluorescent solar collectors. As a promising approach for the next generation solar energy convention, the present collectors are still far from practical

use. The main problems are inefficient absorption of solar radiation and the escape cone loss in fluorescence reabsorption events. Multiple dyes can be doped in collectors to achieve high absorption efficiency, however, this normally leads to low fluorescent quantum yield and high probability of reabsorption. The top escape cone loss can be effectively avoided if good quality photonic filter is applied. Reabsorption can potentially be eliminated by using large Stokes shift dyes such as certain organic dyes or lanthanide complexes. But these dyes either suffer from stability problem or low fluorescent quantum yield.

The most promising approach is to incorporate multiple high fluorescent quantum yield organic dyes into the nano-channels of zeolites to form a cascade resonance energy transfer, thereby effectively decreasing the losses in fluorescence reabsorption with concomitant better spectral coverage of the solar radiation. These dye-loaded zeolites can be spincoated on high quality glass substrates to form a thin film collector. And then, with the proper use of a good quality photonic filter, the power conversion efficiency for zeolite-based collector exceeding 10% is not far away.

Chapter 5 Photon Reabsorption in Fluorescent Solar Collectors

This chapter has been published in part as:

[1] L. Fang, T. S. Parel, L. Danos, and T. Markvart, "Modelling the performance of fluorescent solar collectors," in *Proceedings of the 7th Photovoltaic Science Application and Technology Conference*, pp.165-168, Heriot-Watt University, Edinburgh, UK, 2011.

[2] L. Fang, T. S. Parel, L. Danos, and T. Markvart, "Photon reabsorption in fluorescent solar collectors," *Journal of Applied Physics*, vol. 111, no. 7, pp.076104-3, 2012.

5.1 Introduction

Understanding photon reabsorption (also known as recycling) is important to the design and optimum operation of devices such as fluorescent solar collectors, solar cells, semiconductor lasers or LEDs [99]–[101]. Arguably the clearest exposition of this subject has been presented with application to fluorescent solar collectors, which represent useful structures for the study of reabsorption since a large fraction of the re-emitted photons are trapped inside the collector and can be observed when emitted from the edge. In media with high absorbance, photons undergo multiple reabsorption and reemission or simply photon-recycling and gradually enter thermodynamic equilibrium with the light absorbing media before exit the collector edge [23]. Thermodynamic theories of such processes have been developed by Kennard and Stepanov for molecular structures [102], [103] and by van Roosbroeck and Shockley [104] for radiative recombination in semiconductors. Starting from the general form for spectral reabsorption probability given by Eq. (4.9), this chapter gives a new theoretical expression for the edge fluorescence spectrum of a collector observed in experiments, which is different to the fluorescence spectrum seen by a fully optical coupled edge solar cell. We show that this analytical expression agrees well with experimental measured edge fluorescence spectra. And a particularly useful universal form of the spectral reabsorption probability is found in the limit of high reabsorption.

5.2 Model description

The classical theory used to predict the photon flux which enters the solar cell at the edge of the collector was developed by W&L [105]. As this flux exits the collector from a full hemisphere, it cannot be observed by an observer in a medium with refractive index lower than that of the collector. As shown in Fig. 5.1, only the photons re-emitted in the red colour Edge Escape Cones (EEC) can escape from the collector and be detected by an observer at the collector edge. Thus, if the edge solar cell is not well-coupled to the collector, a significant fraction of edge photons

cannot be captured by the solar cell and this represents a typical practical loss as discussed in Sec. 4.4.5.

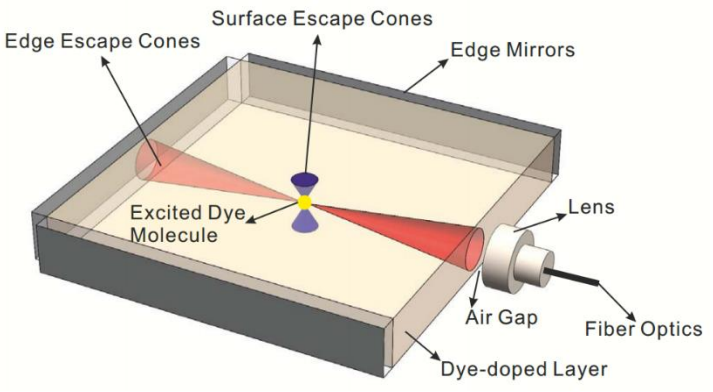

Figure 5.1: FSC structure and photon flux observed at the edge by a spectrometer [58].

This section discusses the spectral reabsorption probability for photons considered to be collected in the model of W&L and that for the photons emitted in the EEC. Similar assumptions in the model of W&L are applied here. The generalised form for the spectral reabsorption probability $r(\lambda_{ems})$ is given by Eq. (4.9) and it is rewritten here as

$$1-r(\lambda_{ems}) = \int_{(V_0)} \frac{dV}{V_0} \int_{(\Omega_0)} \frac{d\omega}{\Omega_0} e^{-\alpha(\lambda_{ems})l} \tag{5.1}$$

where λ_{ems} is the fluorescence emission wavelength. The spectrum of the photons collected at collector edge denoted by $f(\lambda_{ems})$ is predicted by

$$f(\lambda_{ems}) = f_1(\lambda_{ems})\{1-r(\lambda_{ems})\} \tag{5.2}$$

where $f_1(\lambda_{ems})$ is the normalised first generation fluorescence spectrum given by Eq. (4.22).

5.2.1 Model of W&L

In the model of W&L, the edge solar cell is assumed to be perfectly optically coupled to the collector, and all the photons emitted outside of the surface escape cones are assumed to be captured by the edge solar cell. The spectral reabsorption probability for the photons seen by a fully coupled edge solar cell is given by W&L in Eq. (4.10) and rewritten here as

$$\begin{aligned} &\{1-r(\lambda_{ems})\}_{\mathrm{WL}} = \frac{1}{4\pi(1-P)} \\ &\int_0^{\pi} d\phi \int_{\theta_c}^{\pi-\theta_c} \frac{\sin\theta\sin\phi}{\alpha(\lambda_{ems})L}\left\{1-\exp\left[\frac{-2\alpha(\lambda_{ems})L}{\sin\theta\sin\phi}\right]\right\}\sin\theta d\theta \end{aligned} \tag{5.3}$$

5.2.2 Model for edge escape cone

Light propagation in a collector is shown in Fig. 5.2. For a fully optically coupled solar cell, all the photons emitted outside of the surface escape cone 2 and 4 are collected by the solar cell, as denoted by the blue light path. While in the measurement of edge fluorescence by a spectrometer, only photons emitted in EEC 1 and 3 can be captured by a spectrometer, as denoted by the red light path.

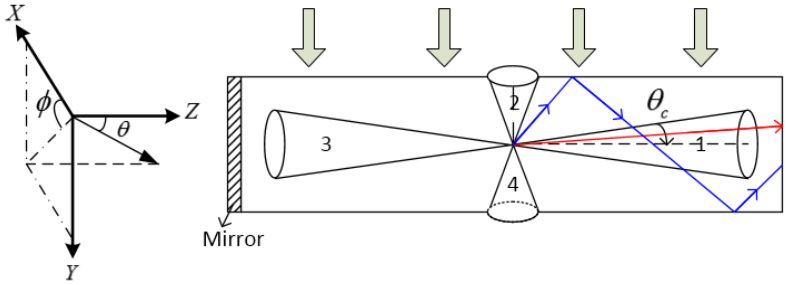

Figure 5.2: Light path in the model of W&L (blue line) and EEC (red line).

A simple calculation using Eq. (5.1) give the spectral reabsorption probability for the photons emitted in the EEC as

$$\{1-r(\lambda_{ems})\}_{\mathrm{EEC}} = \frac{1}{4\pi P\alpha(\lambda_{ems})L} \int_0^{2\pi} d\phi \int_0^{\theta_c} \left\{1-\exp\left[-\frac{2\alpha(\lambda_{ems})L}{\cos\theta}\right]\right\}\cos\theta\sin\theta d\theta \tag{5.4}$$

where the spherical angles θ and ϕ are defined in Fig. 5.2. The numerical calculation results of Eq. (5.3) and Eq. (5.4) are shown in Fig. 5.3.

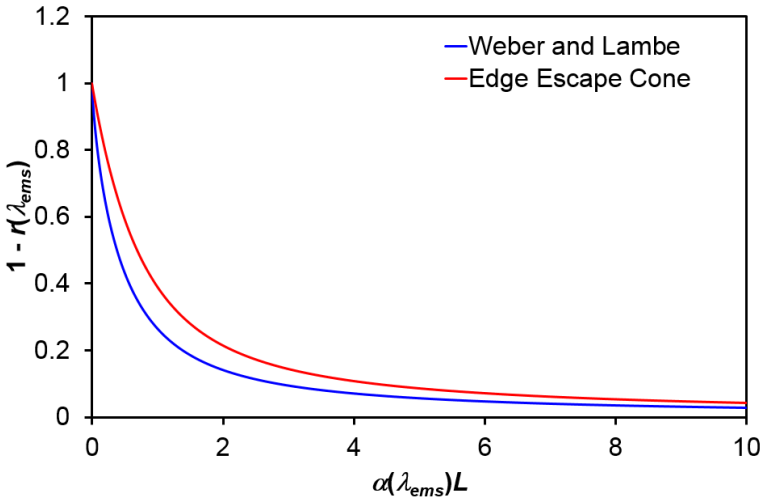

Figure 5.3: Spectral reabsorption probabilities for W&L and EEC.

The spectral reabsorption probability is plotted against the product of the absorption coefficient and the length of the collector in Fig. 5.3. It is shown that the spectral reabsorption probability for the photons assumed to be collected in the model of W&L is larger than that for the photons emitted in the EEC. Clearly, photons collected in the model of W&L propagate longer pathlengths before reaching the edge solar cell, as shown in Fig. 5.2.

5.2.3 Universal reabsorption limit

In the limit of high reabsorption, thermodynamic equilibrium between the collector medium and the fluorescent radiation is rapidly established, which requires that the photon absorption rate of the collector medium equals to the edge-emission rate and thereby photon reabsorption is limited. When $\alpha(\lambda)L >> 1$, the exponential term in Eq. (5.3) can be omitted and an approximation can be given as

$$\left\{1-r(\lambda_{ems})\right\}_{\mathrm{WL}} \approx \frac{1}{4\pi(1-P)\alpha(\lambda_{ems})L}\int_0^{\pi}\sin\phi d\phi\int_{\theta_c}^{\pi-\theta_c}(\sin\theta)^2 d\theta \tag{5.5}$$

Similarly for Eq. (5.4) we obtain

$$\left\{1-r(\lambda_{ems})\right\}_{\mathrm{EEC}} \approx \frac{1}{4\pi P\alpha(\lambda_{ems})L}\int_0^{2\pi}d\phi\int_0^{\theta_c}\cos\theta\sin\theta d\theta \tag{5.6}$$

In order to give a unified expression for the reabsorption limit, the concept of optical étendue is introduced [106]. Optical étendue is a convenient concept used in geometrical optics to describe the size of a beam. For a beam with propagation directions within an infinitesimal solid angle $\delta\omega$ passing through an infinitesimal area δA shown in Fig. 5.4, the element of étendue $\delta\mathscr{E}$ is defined as

$$\delta\mathscr{E} = n^2\cos\theta\delta\omega\delta A \tag{5.7}$$

where θ is the angle between the beam propagation direction and the normal to δA.

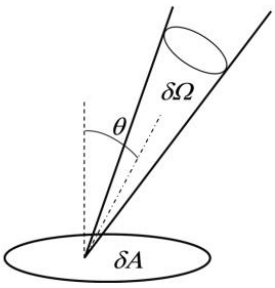

Figure 5.4: The concept of optical étendue [4].

Applying this concept to the light beam emitted from the collector edge, Eq. (5.5) and Eq. (5.6) converge to an identical form of

$$1-r(\lambda_{ems})=\frac{\mathscr{E}}{\alpha(\lambda_{ems})n^2V_0\Omega_0} \tag{5.8}$$

where n is the refractive index of the collector matrix, $V_0=L\cdot A_{edge}$ the volume of the collector, A_{edge} the area of the edge surface, Ω_0 the relevant solid angle ($\Omega_0=4\pi(1-P)$ for W&L, and $4\pi P$ for EEC), and $\mathscr{E}$ the relevant optical étendue of the edge light beam which is given by

$$\mathscr{E}=n^2A_{\text{edge}}\int_0^{\Omega_0/2}\cos\theta d\omega \tag{5.9}$$

where θ is defined in Fig. 5.2. Equation (5.8) shows that, in the large reabsorption limit, the reabsorption probability for a light beam emitted from the edge depends only on its size, i.e. its optical étendue, the absorption coefficient and the refractive index of the collector matrix. We shall call it the universal reabsorption limit.

5.3 Experimental

This section summarises the experimental details of fabrication and characterisation of fluorescent solar collectors.

5.3.1 Sample preparation

The dye powder (BASF Lumogen F Red 305 dye) was mixed with PMMA (MICRO CHEM 950 PMMA C 10), and then the mixture was placed in an ultrasonic bath for 1 hour to aid dissolution of the dye. The dye doped PMMA solution was dropped onto cleaned glass substrates (Menzel, 20×20×1 mm, clear cut edges) and spincoated. The spincoating speed was set to 500 rpm with acceleration of 100 rpm/s for all the samples in order to maintain identical PMMA film thickness. The spincoated samples were left at room temperature for 24 hours to consolidate before spectral measurements. The dye concentrations were 200, 100 and 50 mg/L for three different samples. The molar mass of the dye is not specified by the manufacturer, so the units of the concentrations were in mg/L.

5.3.2 Spectral measurements

For absorbance measurements, a halogen lamp equipped with a monochromator was used as the excitation light source and a calibrated silicon detector (dh_Si, Bentham Instruments Ltd.) was used to collect the transmitted light. As shown in Fig. 5.5, an aluminium structure was used

to align the excitation light beam to be perpendicular to the surface of the collector and the red square was the sample.

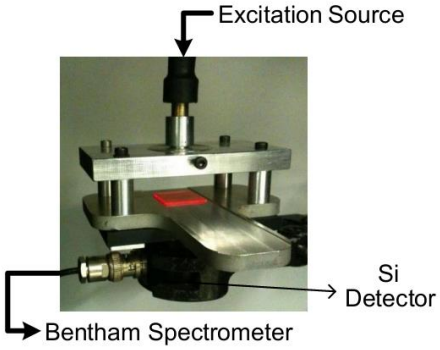

Figure 5.5: Absorbance measurement setup.

The top fluorescence spectra were measured by a calibrated Avantes spectrometer (AvaSpec-2048, grating UA 200-1100 nm, slits 25 μm based on the symmetrical Czerny-Tuner design with a 2048 pixel CCD detector array) with integration time of 300 milliseconds and average for 100 times. The collector samples were excited at 440 nm (bandwidth 2 nm) by light from a monochromator controlled by the Bentham spectrometer. As shown in Fig. 5.6, the excitation optical fibre was fixed 60 degree to the detection direction. The aligned optical lens above the collector sample is used to focus the top fluorescence to the fibre optic. The photo below the spectrometer shows a collector sample under excitation during measurements.

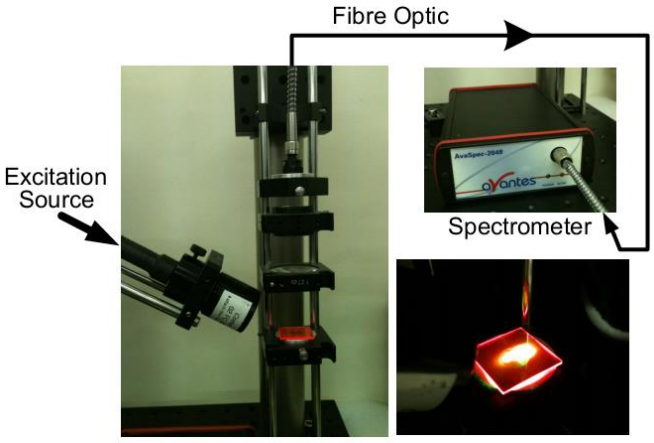

Figure 5.6: Top fluorescence measurement setup.

The edge fluorescence spectra were measured by the Avantes spectrometer at one edge with integration time of 300 milliseconds and average for 100 times, the other edges were covered by highly reflecting films (3M Vikuiti Enhanced Specular Reflector) with specular reflectance over 98% across the visible spectrum. The excitation light source was a Xenon lamp with a band pass filter at 440 nm (bandwidth 10 nm). The incident light intensity was uniform on the top surface of the collector.

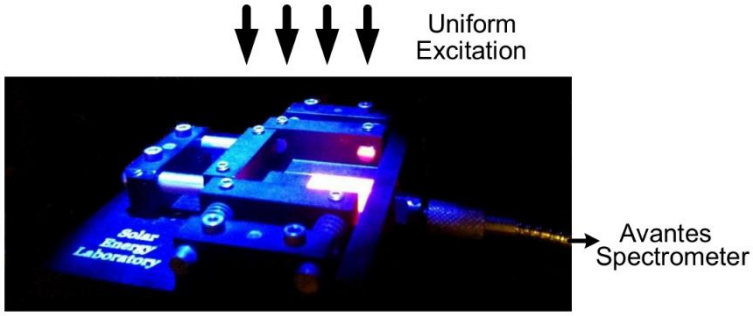

Figure 5.7: Edge fluorescence measurement setup.

5.4 Results and discussion

This section summarise the experimental results and comparison with the model of W&L and the EEC model discussed in Sec. 5.2.

5.4.1 Reabsorption characterisation

The reabsorption characterisation approach employed the model of Markvart, as reviewed in Sec. 4.7.3. The spectra reabsorption probability was obtained by scaling the edge fluorescence spectrum (f_e) to the spectrum without reabsorption, obtained by observing fluorescence from the top of the collector for samples with low dye concentration (referred to as the first generation fluorescence spectrum, f_1) [55]. This approach is illustrated in Fig. 5.8. The edge fluorescence spectrum of a collector with dye concentration of 200 mg/L is scaled to the normalised first generation, which is a measured top fluorescence from a collector sample with dye concentration of 40 mg/L. It is seen that f_e fits well with f_1 at the low absorption wavelength range, which is used to normalise the edge spectra. Then the spectral reabsorption probability $r(\lambda)$ can be obtained by

$$1-r(\lambda)=f_e(\lambda)/\ f_1(\lambda) \tag{5.10}$$

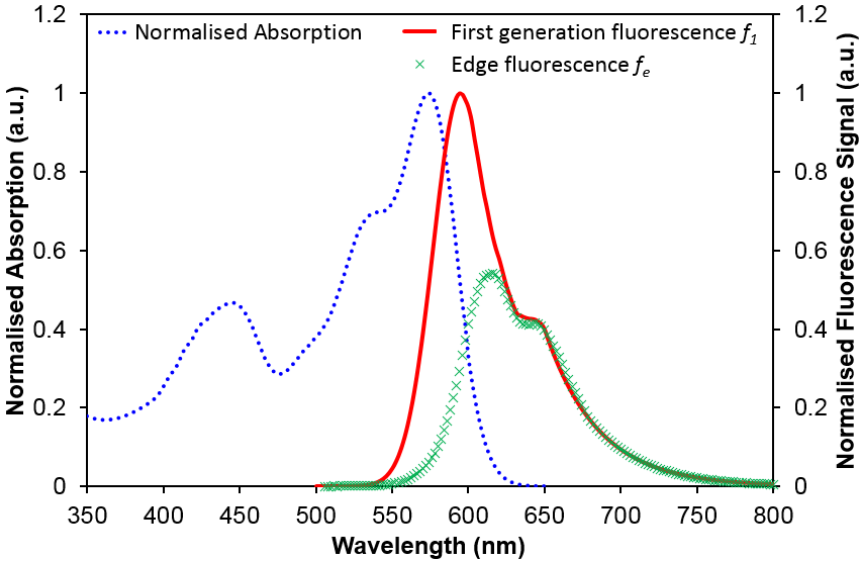

Figure 5.8: Normalised absorption and fluorescence spectra.

The spectral reabsorption probabilities obtained by Eq. (5.10) are compared with both the model of W&L (given by Eq. (5.3)) and the model for EEC (given by Eq. (5.4)) in Fig. 5.9, where L is the length of the FSC samples and α_{eff} is an effective absorption coefficient averaged over the thicknesses of the dye-doped PMMA film and the glass substrate [55]

$$\alpha_{eff} = \alpha_{film} d_{film} / (d_{film} + d_{glass}) \tag{5.11}$$

where α_{film} is the absorption coefficient of the PMMA film which has been doped with dye, d_{film} the thickness of the PMMA film and d_{glass} the thickness of the glass substrate.

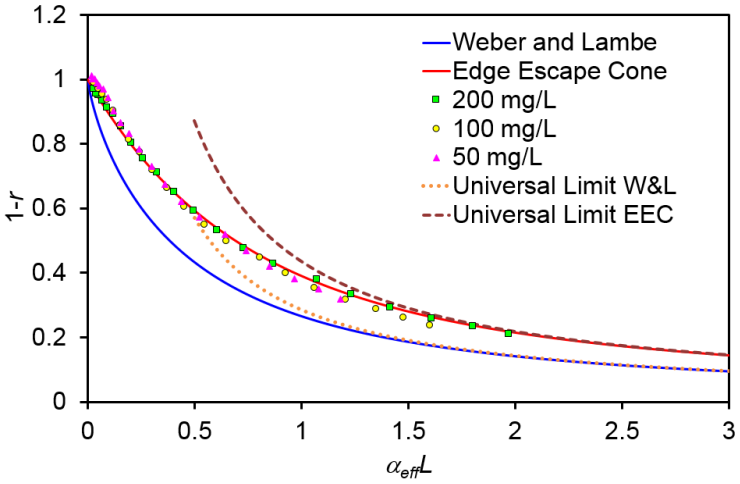

Figure 5.9: Experimental reabsorption probability compared with modelling results.

It is seen from Fig. 5.9 that the experimental results fit well with the EEC model. And at high absorption the universal reabsorption limit coincides with both of the two models. Whereas at low absorption, the photon reabsorption probabilities given by them are lower than the related

universal limit. The reason is that there is a limited number of reabsorption events occurring before the photon flux is emitted from the edge of the collector.

5.4.2 Spectra of edge fluorescence

The edge emission spectra seen by a spectrometer can be predicted by Eq. (5.2). The predicted results and experimentally observed results are compared in Fig. 5.10.

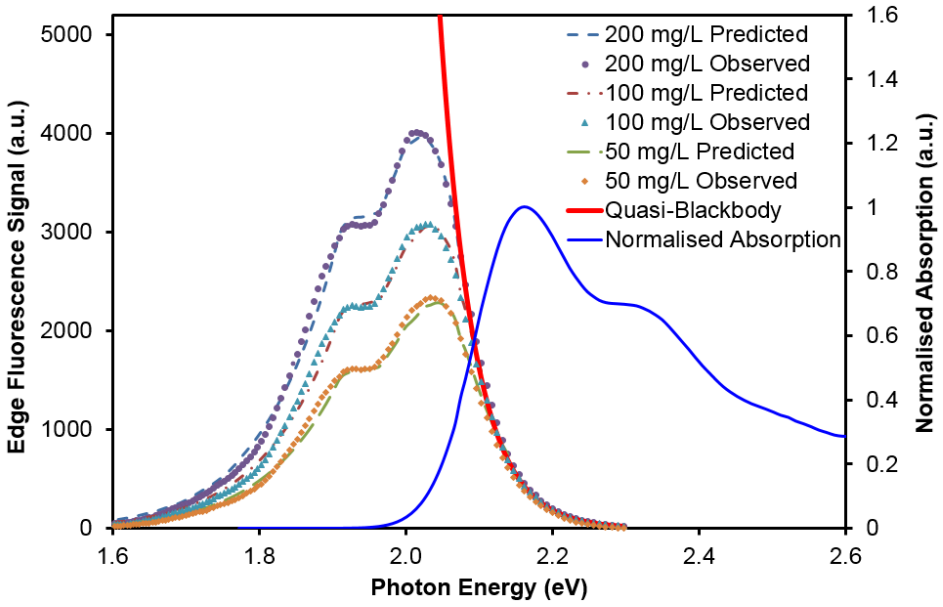

Figure 5.10: Comparison of predicted and observed edge fluorescence spectra.

Figure 5.10 shows an excellent agreement between the shape and position (redshift) of the predicted and observed f_e. At the high absorption photon energy range, photons undergo photon-recycling and enter thermal equilibrium before exit the FSC edge, thus f_e at this range resembles the quasi-blackbody radiation spectrum that can be fitted exponentially [23]. As shown by the red line in Fig. 5.10, the fitting result overlaps with all the spectra lines regardless of dye concentration. Thus even with less fluorescent dye molecules, the high energy photons still enter thermal equilibrium because of strong reabsorption. In contrast, at the low absorption photon energy range f_e is proportional to the dye concentration. This is because that a limited number of reabsorption and reemission events occur for low energy photons and the edge output is proportional to absorption of the collector samples. Similar results have also been obtained for collectors doped with other organic dyes, i.e. Coumarin 540A (Exciton), and Rhodamine 6G (Acros Organics).

5.5 Conclusion

Understanding photon reabsorption in fluorescent solar collectors is important for increasing the optical efficiencies of fluorescent solar collectors. This chapter presents an analytical

expression to characterise photon reabsorption in collectors, which represent a major source of photon loss. A particularly useful universal form of this expression was found in the limit of high reabsorption, which gives the photon reabsorption probability in a simple form as a function of the absorption coefficient and the optical étendue of the emitted light beam. This mathematical model predicts fluorescence spectra emitted from the collector edge, which are in excellent agreement with experiments, and provide an effective characterisation tool for photon transport in fluorescent solar collectors. Based on this analysis, it will be possible to infer the photon flux emitted from the edge of a collector onto a fully optically coupled solar cell, which is not easy to measure experimentally. This general expression is also valid for the new and more complex systems described in literature [3], [4], as long as photon reabsorption exists.

Chapter 6 Solar Cell as a Waveguide

This chapter has been published in part as:

L. Fang, L. Danos, T. Markvart, "Solar cell as a waveguide: quantum efficiency of an ultrathin crystalline silicon solar," in *Proceedings of the 28th European Photovoltaic Solar Energy Conference*, Paris, France, 2013.

6.1 Introduction

An analysis of an ultrathin crystalline silicon solar cell with 200 nm thick active layer fabricated in our laboratory shows that the behaviour of quantum efficiency as a function of wavelength is primarily determined by the absorption of light in the active layer, showing a series of interference peaks. In this chapter, this crystalline silicon solar cell is modelled in detail, perceiving the solar cell as a waveguide. We find that the peaks in the quantum efficiency lie close to the wavelengths of the trapped (internal) modes of the waveguide. This chapter provides a detailed explanation of how these modes, normally inaccessible to external observation, can be detected in external quantum response, in terms of the position of poles of the absorbance of the active silicon layer, in the complex wavenumber plane.

6.2 An ultrathin silicon solar cell

An ultrathin crystalline silicon solar cell has been fabricated in the cleanroom of Southampton Nanofabrication Centre (SNC) and the experimental procedure was described in [107]. The solar cell was based on the Silicon-On-Insulator (SOI) structure with active silicon layer of only 200 nm thick. The cross-sectional view of the solar cell and the nominal thickness of each layer are shown in Fig. 6.1.

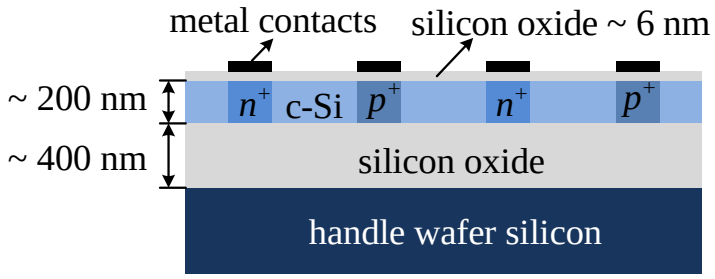

Figure 6.1: Structure of an ultrathin silicon solar cell [107].

The photo of the fabricated solar cell under microscope is shown in Fig. 6.2.

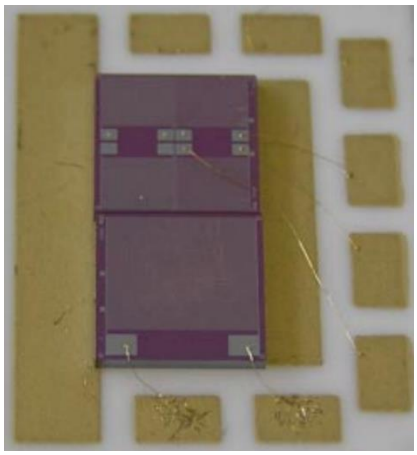

Figure 6.2: Microscope photo of the ultrathin silicon solar cell [107].

6.3 Quantum efficiency results

The external quantum efficiency of the solar cell is related to the absorbance of the solar cell by a factor, i.e. the collection efficiency of carriers:

$$EQE(\lambda) = A(\lambda) * Q(\lambda) \tag{6.1}$$

where $EQE(\lambda)$ the external quantum efficiency, $A(\lambda)$ the absorbance of the solar cell and $Q(\lambda)$ the collection efficiency of the carriers generated by the photon of wavelength λ. The absorbance of the solar cell with structure shown in Fig. 6.1 was obtained by the transfer matrix method introduced in Sec. 2.7. The quantum efficiency has been measured by the Bentham spectrometer equipped with a quantum efficiency measurement module, and the excitation light was in the normal direction of the solar cell surface. The measured quantum efficiency and modelled absorbance of the solar cell are compared in Fig. 6.3.

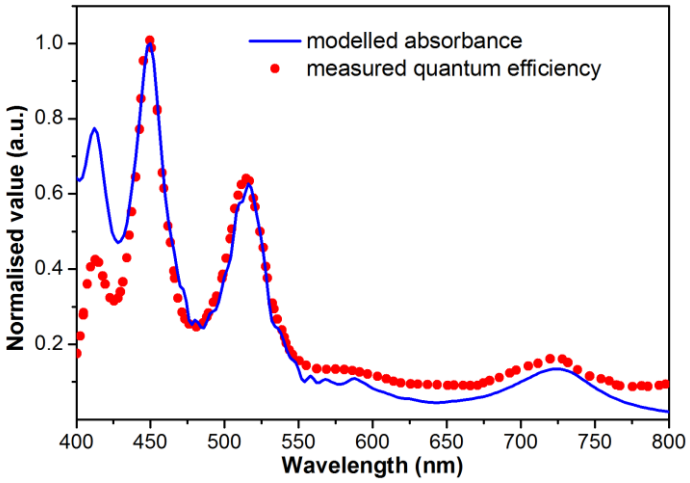

Figure 6.3: Spectral response of the ultrathin silicon solar cell.

The good fit in Fig. 6.3 suggests that the collection efficiency $Q(\lambda)$ is a constant, i.e. unity, through most part of the device. The deviation at short wavelength range is due to surface

recombination of the electron-hole pairs generated by absorption of related photons near the solar cell top surface. The measured quantum efficiency also shows four local peaks in the wavelength range 400 ~ 800 nm, which are not shown for bulk crystalline silicon solar cells [108].

These peaks are due to the constructive interference of light in the silicon layer, or simply due to the resonance of the Fabry-Perot modes. A simple calculation of the resonance condition of these modes by using Eq. (2.32) yields the resonance wavelength and the results are shown in Tab. 6.1.

m	5	4	3	2
Wavelength (nm)	415	460	548	750

Table 6.1: Mode number and wavelength of the Fabry-Perot modes.

It is seen that the calculated resonance wavelengths of the Fabry-Perot modes well correspond to the measured peaks of the quantum efficiency of the solar cell. The discrepancies are small and are mainly due to the neglect of the influence of the silicon substrate in the solar cell.

We show below that these local peaks can also be related to the waveguide modes supported by the thin silicon solar cell, via a pole analysis of the solar cell absorbance in the complex plane of wavenumber.

6.4 Analytical properties of solar cell absorbance

The solar cell can be modelled as a thin silicon layer sandwiched by two layers of silicon dioxide, as shown in Fig. 6.4.

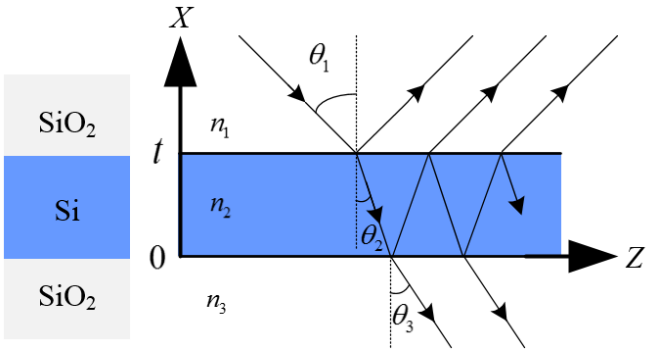

Figure 6.4: Light propagation near a planar slab.

The absorbance of this structure is given by Eq. (2.30) and rewritten here

$$A = 1 - \left| \frac{r_{12} + r_{23} e^{2i\phi}}{1 + r_{12} r_{23} e^{2i\phi}} \right|^2 - \frac{n_3 \cos\theta_3}{n_1 \cos\theta_1} \left| \frac{t_{12} t_{23} e^{i\phi}}{1 + r_{12} r_{23} e^{2i\phi}} \right|^2 \tag{6.2}$$

where the phase retardation is given by $\phi = k_{2x} t$.

It is apparent from Eq. (6.2) that the absorbance has singularities when the denominator of the second and the third term vanishes. These singularities are poles in the complex wavenumber plane whose position is given by $1+r_{12}r_{23}e^{2i\phi}=0$; in other words, when the wavenumber component in the x direction ($k_{2x}=n_2k_0\cos\theta_2$) equals to

$$k_{2x}=\frac{2m\pi+2\phi_{21}+2\phi_{23}+i\ln|r_{21}||r_{23}|}{2t}\quad(m=0,1,2,3....) \tag{6.3}$$

where k_0 the wavenumber in vacuum, $r_{21}=|r_{21}|e^{-i2\phi_{21}}$, $r_{23}=|r_{23}|e^{-i2\phi_{23}}$ and m is an integer. For the waveguide modes trapped by TIR, $\theta_2>\theta_c$ (critical angle for TIR) and $|r_{21}|=|r_{23}|=1$, Eq. (6.3) can be rewritten as

$$2k_{2x}t-2\phi_{21}-2\phi_{23}=2m\pi\quad(m=0,1,2,3....) \tag{6.4}$$

This is exactly the characteristic dispersion relation for the waveguide modes and m represents the mode index number, as discussed in Sec. 2.8.3. For these waveguide modes, the poles for the absorbance given by Eq. (6.3) are on the real axis of the complex plane of k_{2x} .

On the other hand, Eq. (6.4) is also the resonance condition for the Fabry-Perot modes, which interferes constructively in the thin silicon layer, as discussed in Sec. 2.8.2. For these modes, the light propagation angle $\theta_2<\theta_c$, the reflection coefficient $|r_{21}|=|r_{23}|<1$, and the poles of the absorbance given by Eq. (6.3) move to the complex plane of k_{2x} .

Thus, the absorbance has poles in the complex plane of k_{2x} . The poles locate on the real axis correspond to the waveguide modes, while the poles in the complex plane correspond to the Fabry-Perot modes. We find that the poles related to the Fabry-Perot modes lie close to the poles related to the waveguide modes propagating near the critical angle.

From Eq. (6.3) the poles related to the trapped waveguide modes propagating near the critical angle are given by

$$k_{2x}\approx\frac{2m\pi}{2t}\quad(m=0,1,2,3....) \tag{6.5}$$

with the condition

$$\theta_2\approx\theta_c \tag{6.6}$$

The poles related to the Fabry-Perot modes are given by

$$k_{2x} = \frac{2m\pi + i\ln|r_{21}||r_{23}|}{2t} \quad (m = 0,1,2,3....) \tag{6.7}$$

with the condition

$$\theta_2 = 0 \sim \theta_c \tag{6.8}$$

Now we consider the resonance condition of the Fabry-Perot modes and the waveguide modes propagating near the critical angle for TIR. Because the extinction coefficient of silicon is small relative to the real part of the refractive index in the spectral range of interest, the phase angles for the Fabry-Perot modes are close to zero, i.e. $\phi_{21} = \phi_{23} \approx 0$. This condition corresponds to the waveguide modes propagating near the critical angle for TIR. Thus, the resonance condition for the Fabry-Perot modes and the waveguide modes propagating near the critical angle for TIR are in an identical form given by Eq. (2.32). Clearly, the real part of Eq. (6.7) is close to the result given by Eq. (6.5), while the imaginary part is given by the Fresnel reflection coefficients, which is dependent on the angle of propagation, and the thickness of the active silicon layer.

6.4.1 Poles of solar cell absorbance

For our thin solar cell, the thickness of the active silicon layer is only 200 nm and thus Eq. (6.4) only has a few discrete solutions. By solving (6.4) numerically, the wavelength and mode index number for the waveguide modes can be obtained and the result is shown in Tab. 6.2.

m	5	4	3	2
Wavelength (nm)	410	448	524	698

Table 6.2: Mode number and wavelength of the waveguide modes.

It is seen that the resonance wavelength of the waveguide modes given in Tab. 6.2 are close to that for the Fabry-Perot modes given in Tab. 6.1. And the largest relative deviation is only 7% for the mode $m = 2$. Substituting the results given in Tab. 6.2 to Eq. (6.5), the poles related to the waveguide modes can be obtained. The poles related to the Fabry-Perot modes are dependent on the propagation angle θ_2. The movement of these poles is plotted in the complex plane of k_{2x} in Fig. 6.5 (b) as θ_2 increases from 0 to the critical angle θ_c. It is seen from Fig. 6.5 (b) that the poles related to the Fabry-Perot modes move away from the poles on the real axis, which corresponds to the waveguide modes. Thus, under light excitation in the normal direction to the solar cell surface ($\theta_2 = 0$), the absorbance of the solar cell should show local peaks close to the wavelength corresponding to these poles. Since the solar cell has unity carrier collection efficiency throughout most of the device, the quantum efficiency is proportional to the solar cell absorbance and it should show the local peaks corresponding to these poles.

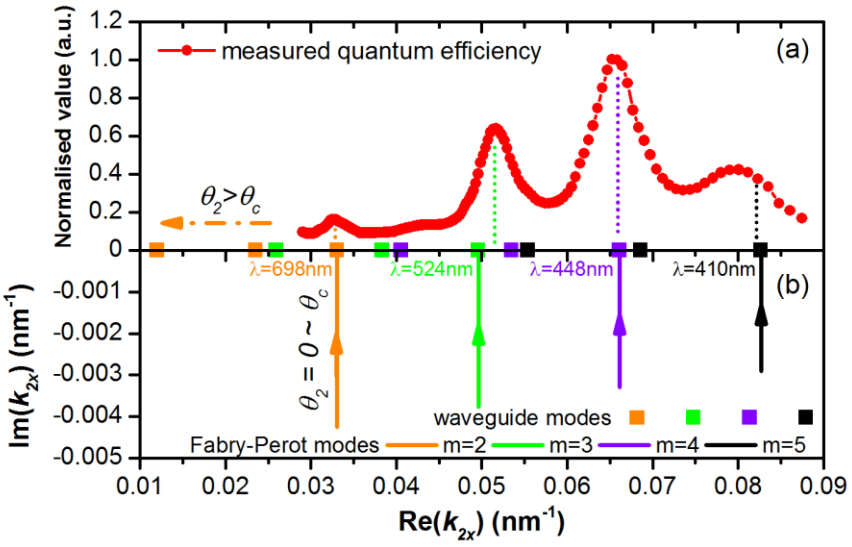

Figure 6.5: (a) The measured quantum efficiency and (b) poles of the solar cell absorbance in the complex plane of k_{2x} .

Figure 6.5 (a) plots the measured quantum efficiency against the related wavenumber $k_{2x} = n_2 k_0 \cos(0)$. It is seen that the local peaks of the quantum efficiency lie close to the poles corresponding to the trapped waveguide modes propagating near the critical angle for TIR in the complex plane of k_{2x}. Thus via the study of the analytical properties of the solar cell absorbance in the complex plane of wavenumber, the local peaks of the quantum efficiency are linked to the waveguide modes propagating near the critical angle for TIR.

6.4.2 Waveguide modes in the ultrathin crystalline silicon solar cell

Solving the characteristic equation for the waveguide modes, i.e. Eq. (6.4), the dispersion relation of the waveguide modes can be obtained. The propagation constant or the in-plane wavenumber $\beta = k_\rho = \left(n_2^2 k_0^2 - k_{2x}^2\right)^{1/2}$ is plotted against the related wavelength in Fig. 6.6 (a) for the TE and TM waveguide modes with different mode number m. The pink line shows the in-plane wavenumber calculated at the critical angle when TIR occurs at the interface of silicon-silicon oxide. It is seen that the propagation constant has identical value for the TE and TM modes with propagation angle close to the critical angle for TIR. Thus, the polarisation of light does not affect the propagation constant of the waveguide modes propagating near the critical angle.

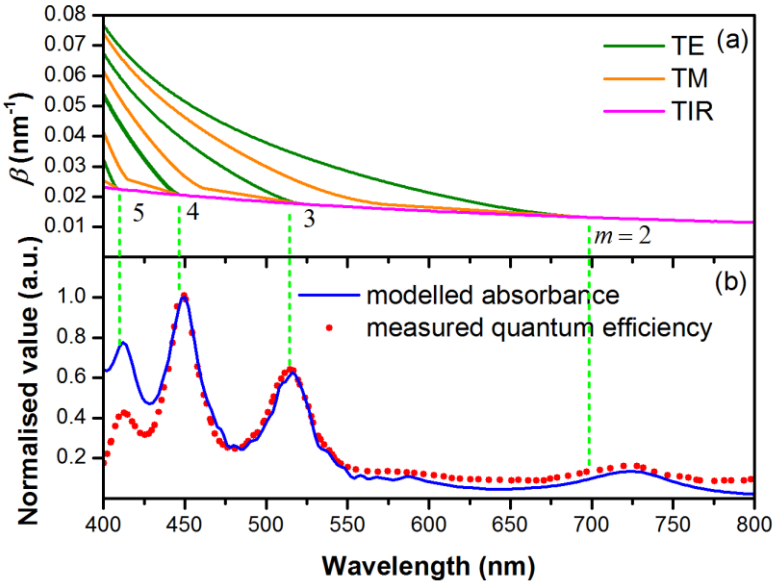

Figure 6.6: (a) Dispersion relation of the waveguide modes and (b) the measured quantum efficiency and modelled absorbance.

The measured quantum efficiency and modelled absorbance of the solar cell is shown in Fig. 6.6 (b). It is apparent that the local peaks of the quantum efficiency lie close to the wavelength of the waveguide modes propagating near the critical angle for TIR.

In the quantum efficiency measurement of our solar cell, the excitation light is in the normal direction to the surface, so there are no waveguide modes but only Fabry-Perot modes excited in the thin silicon layer. However, via the analysis of the poles of absorbance in the complex plane of wavenumber, we find the link between the Fabry-Perot modes and the waveguide modes: the real part of the complex poles (given by Eq. (6.7)) corresponding to the Fabry-Perot modes are nearly identical to the pure-real poles (given by Eq. (6.5)) corresponding to the waveguide modes propagating near the critical angle for TIR. Thus, the local peaks of the measured quantum efficiency also corresponds to these waveguide modes. This correspondence shows that the normally hidden feature of the waveguide modes can be detected via the quantum response of our thin solar cell.

6.5 Conclusion

The absorbance of a fabricated ultrathin crystalline silicon solar cell has been modelled analytically. By studying the poles of the absorbance in the complex plane of wavenumber, we find that the peaks of the quantum efficiency of the solar cell lie close to the resonance frequency of the waveguide modes propagating near the critical angles for total internal reflection. The normally inaccessible feature of the waveguide modes to external observation

can thus be detected in external quantum response, in terms of the poles of the absorbance of the active silicon layer, in the complex wavenumber plane.

The measured efficiency of our thin solar cell was only 0.12% [107], as expected from the ultrathin active silicon layer of the solar cell. The next chapter reviews various approaches to improve the efficiency of thin solar cells by exciting waveguide modes inside these solar cells.

Chapter 7 Literature Review of Fluorescence near Interface

7.1 Introduction

Many novel approaches have been reported to overcome the principal challenge to improve the optical absorption in silicon solar cells. These include the deposition of dipole-like radiators such as metal nanoparticles [109], fluorescent molecules [110] and quantum dots [111], or integrating dielectric/metallic nanostructures such as gratings or spheres into silicon solar cells [112]. Their common feature is to couple the incident solar radiation into the waveguide modes in the solar cell to enhance the optical path length of light and hence reducing the thickness and material usage of silicon solar cells. The integration of nanostructures in solar cells usually involve complicated and expensive nanofabrication process [112], so it is not considered in this work. This chapter reviews the development of fluorescence and energy transfer near interface and their application in enhancing light capture in silicon solar cells.

7.2 Fluorescence near metal surface

7.2.1 The work by Drexhage

In the 1960s, Kuhn and co-workers performed a series of pioneering experiments to study energy transfer between fluorescent molecules which were deposited as Langmuir-Blodgett monolayers [113]. Drexhage extended their work to studying energy transfer from fluorescent monolayer to metal mirrors. In his work, the dependence of fluorescence lifetime of Eu^{3+} ions on the distance to the surface of gold, silver and copper mirrors were investigated [114] and the experimental configuration is shown in Fig. 7.1. Multiple pure fatty acid Langmuir-Blodgett monolayers were deposited as spacer layers between the Eu^{3+} ions and the metal mirror.

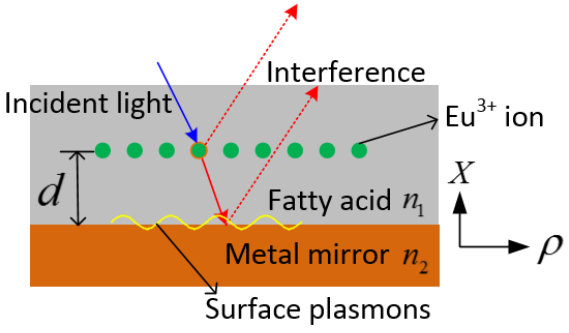

Figure 7.1: Eu^{3+} ions emitting near a metal mirror.

By considering the interference between the source light generated by an excited Eu^{3+} ion, which was modelled as an electric dipole, and the reflected light from the metal mirrors and summing up all the contribution of different angles of light incident, Drexhage gave the

normalised fluorescence damping rate (inverse fluorescence lifetime) for a VED and a HED as [115]

$$\left(\frac{b}{b_0}\right)_{\mathrm{VED}} = 1-q+\frac{3q}{2}\mathrm{Re}\left\{\int_0^1 du\,\frac{u^3}{\sqrt{1-u^2}}\left[1+r_{12}^{\mathrm{TM}}\exp(i2k_{1x}d)\right]\right\} \tag{7.1}$$

$$\left(\frac{b}{b_0}\right)_{\mathrm{HED}} = 1-q+\frac{3q}{4}\mathrm{Re}\left\{\int_0^1 du\left(\begin{array}{l}\dfrac{u}{\sqrt{1-u^2}}\left[1+r_{12}^{\mathrm{TE}}\exp(i2k_{1x}d)\right]\\ +u\sqrt{1-u^2}\left[1-r_{12}^{\mathrm{TM}}\exp(i2k_{1x}d)\right]\end{array}\right)\right\} \tag{7.2}$$

where b_0 is the damping rate in the absence of the mirror, q the fluorescence quantum yield, $u = k_\rho / k_1$ the normalised in-plane wavenumber, k_1 the wavenumber of light in the fatty acid layer, r_{12}^{TM} and r_{12}^{TE} the Fresnel reflection coefficients for the TM and TE modes, respectively, k_{1x} the wavenumber component perpendicular to the mirror surface and d the distance from the molecule to the mirror. Note that Eq. (7.1) and Eq. (7.2) are rewritten from the results given by Drexhage to compare with another model described in the next section. The excited Eu^{3+} ions have no preferred dipole moment orientation and they are isotropically distributed between VEDs and HEDs, so the normalised damping rate is given by [116]

$$\left(\frac{b}{b_0}\right)_{\mathrm{iso}} = \frac{1}{3}\left(\frac{b}{b_0}\right)_{\mathrm{VED}} + \frac{2}{3}\left(\frac{b}{b_0}\right)_{\mathrm{HED}} \tag{7.3}$$

Figure 7.2 shows the comparison of the modelling and the experimental results. It is seen that the interference model fits well with the measured data for the distance beyond 300 nm. While below this distance, the measured fluorescence lifetime diverts from the interference model and decreased monotonically towards zero. This is due to that the interference model only considers the interaction of light which can propagates freely into the far field and energy transfer to the metal mirror via the near field interactions such as coupling to the surface plasmons is totally ignored.

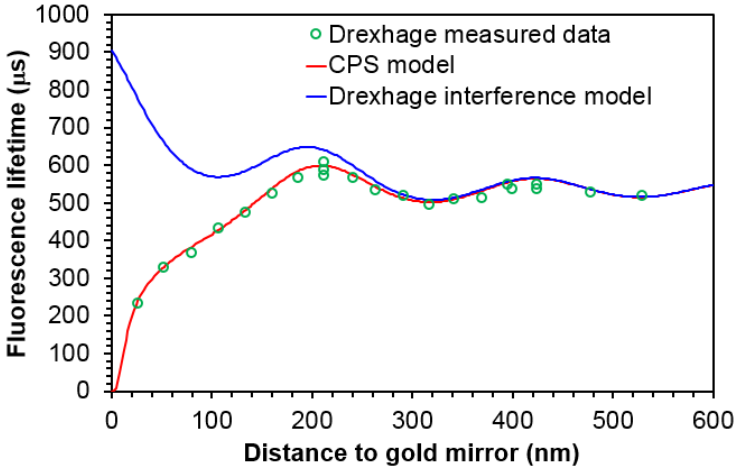

Figure 7.2: Lifetime of Eu^{3+} ions versus distance to a gold mirror.

7.2.2 The pure classic model by CPS

Kuhn also developed a classic mechanical model [117], which modelled the excited fluorescent molecule as a forced and damped harmonic oscillator. The dipole is forced by its own reflected light from the metal mirror and it is damped due to light emission into the far field and energy transfer to the mirror via near field interactions. However, in his model the mirror was idealised, in which case the Fresnel reflection coefficient is given by $r=\exp(i\pi)$ regardless of the angle of light incidence. While in practice, the reflection coefficients depend on the angle of incidence as well as the polarisation of light. Chance, Prock and Silbey (CPS) solved the Maxwell equations for the dipole-mirror system and inserted the full form of the electric field of the light reflected to the dipole position into the mechanical model developed by Kuhn to give the normalised fluorescence damping rate as [118]

$$\left(\frac{b}{b_0}\right)_{\mathrm{VED}}=1-q+\frac{3q}{2}\mathrm{Re}\left\{\int_0^{\infty}du\,\frac{u^3}{\sqrt{1-u^2}}\left[1+r_{12}^{\mathrm{TM}}\exp(i2k_{1x}d)\right]\right\} \tag{7.4}$$

$$\left(\frac{b}{b_0}\right)_{\mathrm{HED}}=1-q+\frac{3q}{4}\mathrm{Re}\left\{\int_0^{\infty}du\left(\begin{array}{l}\dfrac{u}{\sqrt{1-u^2}}\left[1+r_{12}^{\mathrm{TE}}\exp(i2k_{1x}d)\right]\\ +u\sqrt{1-u^2}\left[1-r_{12}^{\mathrm{TM}}\exp(i2k_{1x}d)\right]\end{array}\right)\right\} \tag{7.5}$$

By comparing Eqs. (7.1), (7.2) with Eqs. (7.4), (7.5), one can find that the results given by CPS are only different to the results given by Drexhage in the upper limit of the integral interval. The numerical results for an isotropic dipole configuration from the CPS model is shown in Fig. 7.2. It is seen that the CPS model fits perfectly with the experimental results. So the optical interactions via the high wavenumber components ($u>1$) of the dipole radiation can be accounted in by just extended the integral interval of the model for the far field interaction,

which only accounts the interference of the low wavenumber components ($0 < u < 1$) of the dipole radiation, to infinity. Recent development shows that by introducing a localised density of electromagnetic states [119], the CPS results can be reproduced by a full quantum mechanical approach [120].

7.2.3 Power spectrum of dipole emission

In order to understand the power dissipated in different damping channels by the dipole in the presence of metal mirrors, Ford and Weber (F&W) introduced the concept of power spectrum [121]. The amount of power per unit photon energy dissipated by a dipole in the presence of a mirror is proportional to the modified damping rate [122]

$$\frac{\mathscr{P}}{\mathscr{P}_0} = \frac{b}{b_0} \tag{7.6}$$

where $\mathscr{P}$ and $\mathscr{P}_0$ are the total power dissipated by the dipole in the presence and absence of the mirror, respectively. F&W introduced a power spectrum $d\mathscr{P} / dk_\rho$ which is defined by [121]

$$\mathscr{P} = \int_0^\infty \frac{d\mathscr{P}}{dk_\rho} dk_\rho \tag{7.7}$$

It is seen that the total power is the integral of the power spectrum over all the available in-plane wavenumbers. Combining Eq. (7.6) and Eq. (7.7), one can find that when the fluorescence quantum yield is unity, the power spectrum is direct proportional to the integrand of the fluorescent damping rate given by Eq. (7.4) and Eq. (7.5) and given by [10]

$$\left(\frac{d\mathscr{P}}{dk_\rho}\right)_{\mathrm{VED}} \propto \mathrm{Re}\left\{\frac{u^3}{\sqrt{1-u^2}}\left[1 + r_{12}^{\mathrm{TM}} \exp(i2k_{1x}d)\right]\right\} \tag{7.8}$$

$$\left(\frac{d\mathscr{P}}{dk_\rho}\right)_{\mathrm{HED}} \propto \mathrm{Re}\left\{\begin{array}{l} \dfrac{u}{\sqrt{1-u^2}}\left[1 + r_{12}^{\mathrm{TE}} \exp(i2k_{1x}d)\right] \\ +u\sqrt{1-u^2}\left[1 - r_{12}^{\mathrm{TM}} \exp(i2k_{1x}d)\right] \end{array}\right\} \tag{7.9}$$

The numerical results for the power spectrum of a VED and a HED emitting at different distance to a silver mirror are shown in Fig. 7.3. The emission wavelength of the dipole is assumed be 610 nm, and the corresponding complex refractive index of silver used in calculation is from [123].

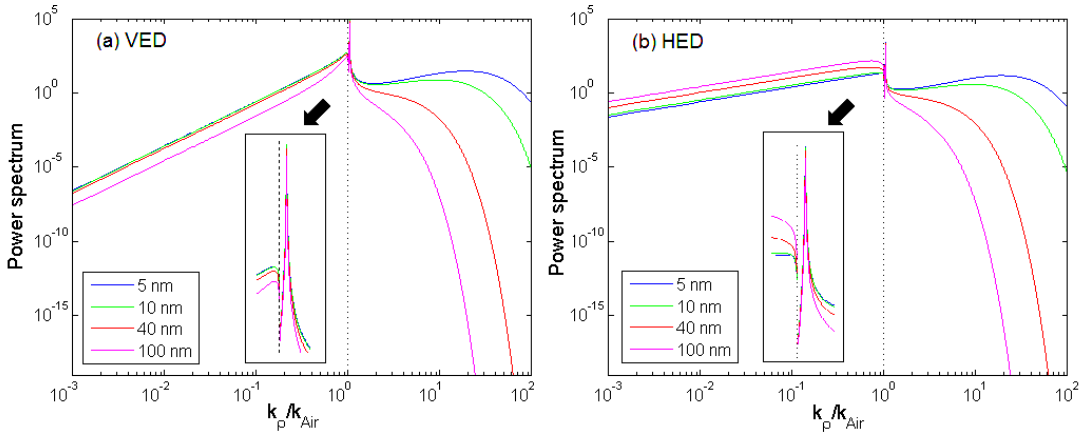

Figure 7.3: Power spectrum for dipole emission near an air-silver interface.

It is seen from Fig. 7.3 that, as the distance to silver mirror decreases the power dissipated in near field ($k_\rho / k_{\mathrm{Air}} > 1$) increases significantly. However, the maximum of the power spectra share a peak at $k_\rho / k_{\mathrm{Air}} = 1.031$, which corresponds to the resonance frequency of the surface plasmon waves supported by the air-silver interface and it is given by

$$k_\rho^{\mathrm{sp}} = \left(\frac{n_1^2 n_2^2}{n_1^2 + n_2^2} \right)^{\frac{1}{2}} k_0 \tag{7.10}$$

where n_1 and n_2 are the refractive index of air and silver, respectively, and $k_0 = 2\pi / \lambda$ the wavenumber in vacuum. The wavenumber components $k_\rho \gg k_\rho^{\mathrm{sp}}$ are termed as lossy surface waves [121], which are ultimately dissipated as heat in metal. To conclude, the power dissipation channels of a dipole emission near a metal mirror consist of light emission into the far field, coupling to surface plasmons and lossy surface waves.

7.2.4 Energy transfer probability

Since the power dissipation channels of a dipole emission near a metal mirror is clear, the fraction of power dissipated in the mirror or the energy transfer probability to mirror can be obtained as [121]

$$\eta_{\mathrm{ET}} = \frac{\mathscr{P}_{\mathrm{photon}}}{\mathscr{P}_{\mathrm{photon}} + \mathscr{P}_{\mathrm{sp}} + \mathscr{P}_{\mathrm{lsw}}} = \frac{\int_{k_{\mathrm{Air}}}^{\infty} \frac{d\mathscr{P}}{dk_\rho} dk_\rho}{\int_0^{\infty} \frac{d\mathscr{P}}{dk_\rho} dk_\rho} \tag{7.11}$$

where $\mathscr{P}_{\mathrm{photon}}$ is the power dissipated by emission of photons, $\mathscr{P}_{\mathrm{sp}}$ the power dissipated in the surface plasmons and $\mathscr{P}_{\mathrm{lsw}}$ the power dissipated in the lossy surface waves.

7.3 Fluorescence near a dielectric waveguide

Molecular fluorescence near a dielectric waveguide was first demonstrated by Holland & Hall [124], [125]. As shown in Fig. 7.4, a thin layer (3 nm) of Rhodamine B molecules was directly deposited on the surface of a lithium fluoride (LiF) waveguide of thickness d , which was fabricated on a silver coated glass substrate. The silver layer worked as a reflecting mirror to eliminate light penetrate into the glass substrate, which has similar refractive index as LiF at the concerned wavelength of light [123].

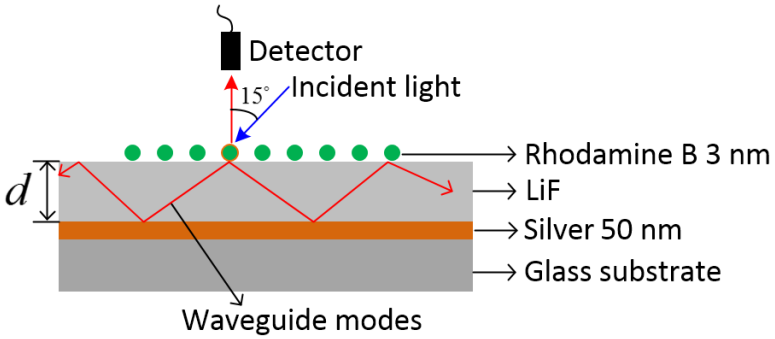

Figure 7.4: Structure for waveguide mode enhanced molecular fluorescence [124].

The Rhodamine B molecules were excited by an argon-ion laser at wavelength 514.5 nm and enhanced fluorescence emission was measured by the detector at the wavelength of 580 nm in comparison to fluorescence measured from Rhodamine B molecules directly deposited on glass substrate. The enhancement dependence on the thickness of the LiF waveguide is shown in Fig. 7.5. It is seen that the maximum enhancement of the Ag/LiF/dye/air configuration, which can support a few waveguide modes, is as high as 500-fold, while the glass/LiF/dye/air configuration, which does support any waveguide modes, shows limited enhancement. The fluorescence enhancement is due to the strong coupling between the near field radiation of the molecular dipole and the waveguide modes mediated by the evanescent waves. The net effect of this coupling is an enhanced molecular absorption rate due to large local electromagnetic fields produced by the waveguide modes and an enhanced molecular emission rate due to dissipation in the waveguide modes [124].

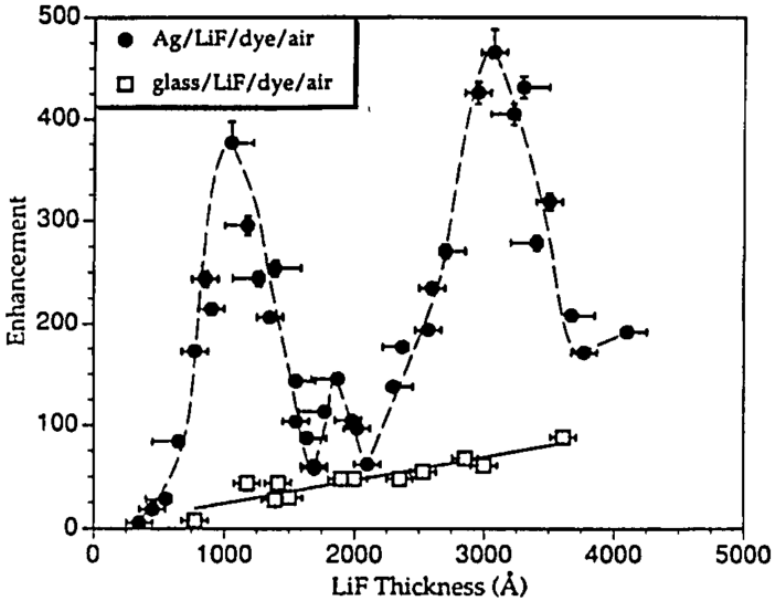

Figure 7.5: Fluorescence enhancement dependence on waveguide thickness [125].

It is also seen that the enhancement of the Ag/LiF/dye/air configuration shows three distinct peaks. This is due to that at the corresponding thickness of the LiF waveguide, the photon tunnelling rate from the Rhodamine B molecules to the waveguide has local maximum value. This phenomenon is discussed further in Chapter 8.

7.4 Fluorescence near semiconducting surface

Energy transfer from excited molecules to semiconducting materials can be distinguished into two types of interactions: Förster-type resonance energy transfer which occurs when the distance between the molecule and the semiconducting material is only a few nanometres; dipole-waveguide interaction which occurs when the distance is in the order of the wavelength of light, similar to fluorescence near a dielectric waveguide.

7.4.1 Förster-type resonance energy transfer

Compared to fluorescence near metals, less work has been done for semiconductors and much emphasis was on the non-radiative energy transfer, which is the dominate energy transfer process when the donor-acceptor distance is only a few nanometres [13]. At this close distance, electron-hole pairs can be directly excited in semiconductors in a way similar to the Förster resonance energy transfer between molecules. This energy transfer process is important to indirect bandgap semiconductors like silicon, where interband electron transition may not need the assistance of phonons. This is because that this energy transfer occurs from a localised state, and no strict momentum conservation is needed in the event of interband electron transition [126], [127]. This advantage was first pointed out and proposed for solar energy conversion by Dexter [128].

The classic CPS model can successfully model the behaviour of molecular fluorescence near metal interfaces. However, the applicability to semiconducting interfaces is yet questionable [13]. The interaction between the excited molecules and the unbounded electrons in metal can be well understood by the dipole-dipole interaction. However, in semiconductors electrons cannot move freely in the fully-occupied valence band. Thus it is not immediately clear that whether the response of semiconducting interface to excited molecules can be successfully modelled by the CPS model.

Nevertheless, many groups have successfully verified efficient energy transfer from fluorescent molecules [126], [129]–[131] or quantum dots [111] to semiconductors via the measurement of fluorescence lifetime, of which the dependence on distance to semiconducting interface, however, has no unified conclusion in the regime below 10 nm. Considering the limit when the distance between the molecule and the metal mirror approaches zero, the energy transfer rate (dissipation into surface plasmons and surface lossy waves) can be obtained from Eq. (7.8) and Eq. (7.9) and given by [118]

$$\lim_{d\to 0}\left(\frac{b_{\mathrm{ET}}}{b_0}\right)_{\mathrm{VED}} = \frac{3q}{(2k_1 d)^3}\,\mathrm{Im}\left(\frac{\varepsilon_2-\varepsilon_1}{\varepsilon_2+\varepsilon_1}\right) \tag{7.12}$$

$$\lim_{d\to 0}\left(\frac{b_{\mathrm{ET}}}{b_0}\right)_{\mathrm{HED}} = \frac{3q}{2(2k_1 d)^3}\,\mathrm{Im}\left(\frac{\varepsilon_2-\varepsilon_1}{\varepsilon_2+\varepsilon_1}\right) \tag{7.13}$$

where ε_1 is the dielectric constant of the medium that the molecule locates and ε_2 is the dielectric constant of the metal mirror. It is seen that the energy transfer rates given by Eq. (7.12) and (7.13) both show inverse cubic dependence on the distance to the metal mirror. However, the reported experimental results divert from this inverse cubic law.

Hayashi [132] found that the dependence of energy transfer rate from thin layers of tetracene (emitting at 580 nm) to silicon using LiF as spacer layer follows an exponential dependence, and for GaAs the energy transfer rate shows no dependence on the distance if it is smaller than 10 nm. However, these results were inferred from fluorescence intensity measurements which may have large errors since the fluorescence intensity quenches dramatically as the distance becomes closer. Deri [133] further analysed the experimental data obtained by Hayashi, and found that the energy transfer process was difficult to separate from light interference. Fluorescence intensity dependence on distance to silicon has also been measured by [134], [135] and they even claimed that no energy transfer occurred. Thus fluorescence intensity studies are not appropriate for investigating the energy transfer process. All the following experimental

results were obtained by fluorescence lifetime measurements. Whitmore [129] found that the dependence for energy transfer from pyrazine (emitting at 380 nm) to GaAs using ammonia as spacer follows the inverse cubic law in the quenching regime and with faster dependence below 10 nm. Whereas Sluch [130] found that the dependence for palmitic acid (emitting at 440 nm) to silicon using tricosanoic acid as spacer is slower than the inverse cubic law. Alivisatos [136] measured fluorescence lifetime of pyrene (emitting at 390 nm) on silicon substrate using xenon as spacer. However, their results cannot give the dependence of energy transfer on the distance to silicon due to the strong intermolecular energy transfer between the pyrene molecules.

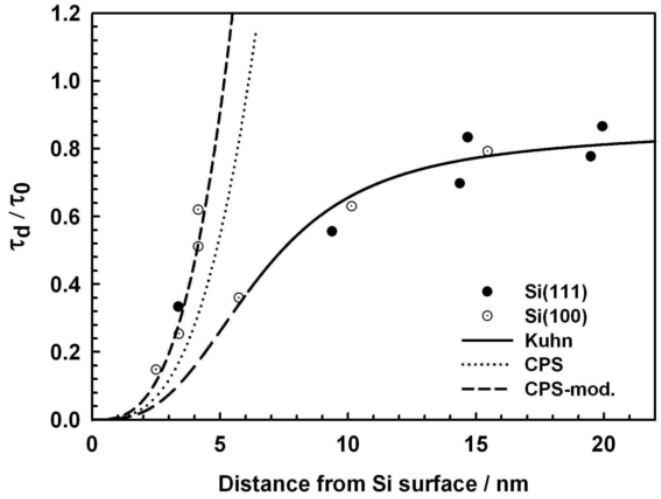

Figure 7.6: Normalised fluorescence lifetime versus distance to silicon surface [131].

Danos [131] modified the extinction coefficient of silicon to fit with the inverse cubic law for energy transfer from a long chain carbocyanine dye using stearic acid as spacer, as shown in Fig. 7.6. Andreakou [137] reported that the dependence for energy transfer from PbS nanoparticles to silicon using silica as spacer layer roughly follows the inverse cubic law but with large error bar below 10 nm. All of these experimental results suggest that the CPS model cannot successfully model dipole emission near semiconducting interfaces. More experimental results at the distance range of 0-20 nm are needed to understand this energy transfer process.

7.4.2 Energy transfer via dipole-waveguide interaction

Beyond the working distance of the Förster-type resonance energy transfer and in the distance range in the order of the wavelength of light, energy transfer by injection waveguide modes into thin silicon films via the evanescent wave of the molecular dipole radiation is less noticed. This energy transfer process is similar to fluorescence near a dielectric waveguide as discussed in Sec. 7.3 and represents an attractive approach for light trapping in thin silicon solar cells when surface texturing is not applicable.

The molecular dipole radiation can be distinguished into three power dissipation channels: fluorescence into the far field ($k_\rho < k_{\text{Air}}$); injecting waveguide modes or photon tunnelling into the thin film ($k_{\text{Air}} < k_\rho < k_{\text{Si}}$); and light harvesting via the near field ($k_\rho > k_{\text{Si}}$). Via evaluating the integral in Eq. (7.4) or Eq. (7.5) in relevant integral interval the damping rate in these three channels can be obtained. Figure 7.7 shows the normalised damping rates in these three power dissipation channels for a HED emitting near bulk silicon and a 25 nm thick thin silicon film, respectively.

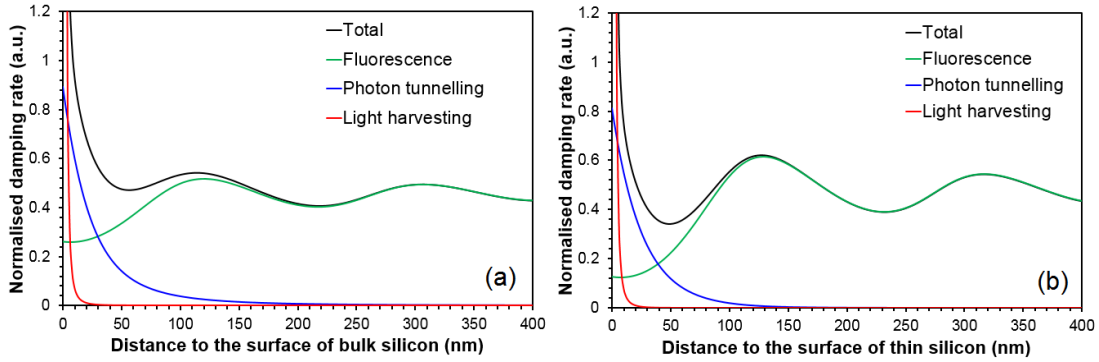

Figure 7.7: Normalised damping rate in three channels for (a) bulk and (b) thin silicon film.

The energy transfer probabilities into these three power dissipation channels can be obtained by dividing respect damping rate to the total damping rate. Figure 7.8 shows the comparison of the energy transfer probabilities for bulk silicon and the 25 nm thick thin silicon film.

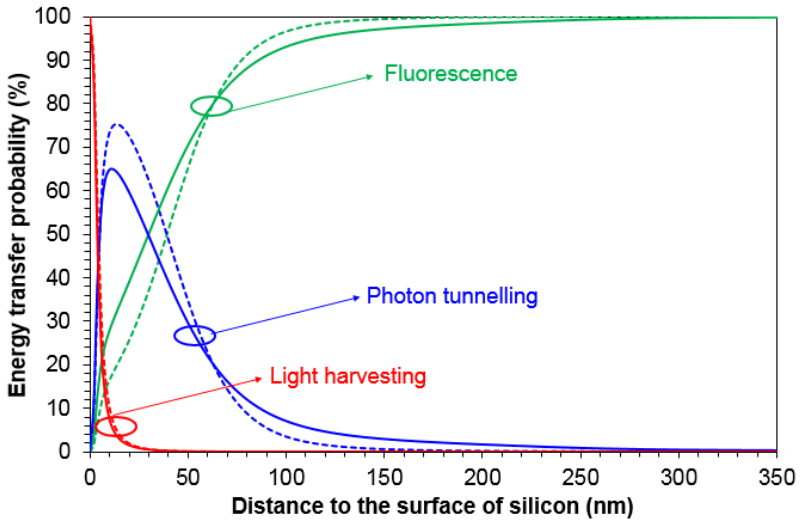

Figure 7.8: Energy transfer probability in three channels for bulk (solid line) and 25 nm thick silicon film (dashed line).

It is seen from Fig. 7.8 that the energy transfer probability via light harvesting and photon tunnelling are quite high even for a 25 nm thick thin silicon film. This highlights the substantial potential for application in light trapping for solar cells. A detailed balance treatment of light

trapping in thin films by using this kind of energy transfer process was given by [138], which showed that significant enhancements in absorption are possible even that the thin silicon film only supports a limited number of waveguide modes. However, the effect of reverse transitions are not included in the energy transfer probabilities shown in Fig. 7.8: the molecules can also couple the trapped waves out of the waveguide via the evanescent waves. Another challenge is to have sufficient molecules deposited on the semiconductor to efficient absorb solar radiation. However, increasing the amount of molecules will result in higher probability for intermolecular energy transfer and hence more loss in fluorescence reabsorption events. In most energy transfer studies, as discussed in Sec. 7.3 and Sec. 7.4.1, only a very thin or monolayer of molecules were deposited on the semiconducting surface. This is to eliminate the energy transfer between the molecules which would complicate the analysis of energy transfer to semiconductors [136]. More sophisticated systems such as zeolites [139] are needed to achieve high absorption probability of solar radiation while maintain low probability of fluorescence reabsorption. Nevertheless, dipole-waveguide coupling mechanism has been demonstrated by metal nanoparticle enhanced ultrathin thin silicon solar cells, which is discussed in the following section.

7.5 Nanoparticle enhanced solar cells

Stuart and Hall (S&H) first demonstrated the dipole-waveguide coupling mechanism by photocurrent enhancement of an ultrathin crystalline silicon photodetector, which was fabricated in a SOI wafer with active silicon layer of 160 nm thick, by deposition of metal nanoparticles on the surface [109]. Figure 7.9 shows the structure of the nanoparticle-photodetector configuration. Localised surface plasmon resonance can be excited in the individual metal nanoparticles by incident photons [140]. The excited nanoparticles then acts as dipole oscillator, which can couple the incident light to the waveguide modes in the underlying thin silicon film.

On the other hand, these nanoparticles can also couple the waveguide modes out of the thin layer via the interaction with evanescent waves of the waveguide modes. In order to compromise these two coupling processes, a 30 nm thick LiF spacer layer was deposited between the nanoparticles and the photodetector.

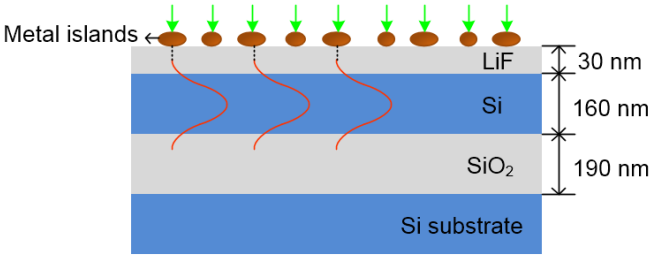

Figure 7.9: Metal nanoparticle-waveguide coupling configuration [109].

Three kinds of metals have been deposited on the photodetector. The transmittance of the metal nanoparticle films deposited on glass slides and photocurrent enhancement of the photodetector are shown in Fig. 7.10. It is seen that the transmittance of the metal films all shows a dip at a certain wavelength, which correspond to the plasmon resonance frequency of the metal nanoparticles. All the nanoparticles have positive enhancements to the photocurrent in the light wavelength range from 600 nm to 950 nm. And the best photocurrent enhancement was achieved by copper nanoparticles with more than an order of magnitude enhancement for light of wavelength 800 nm, which corresponds to the resonance frequency of one of the waveguide mode supported by the underlying SOI structure [141]. Similar results of photocurrent enhancement near the bandgap of other type of solar cells have also been reported, such as wafer based silicon solar cells [142], [143], thin film GaAs solar cells [144], [145], amorphous silicon solar cells [146] and organic solar cells [147].

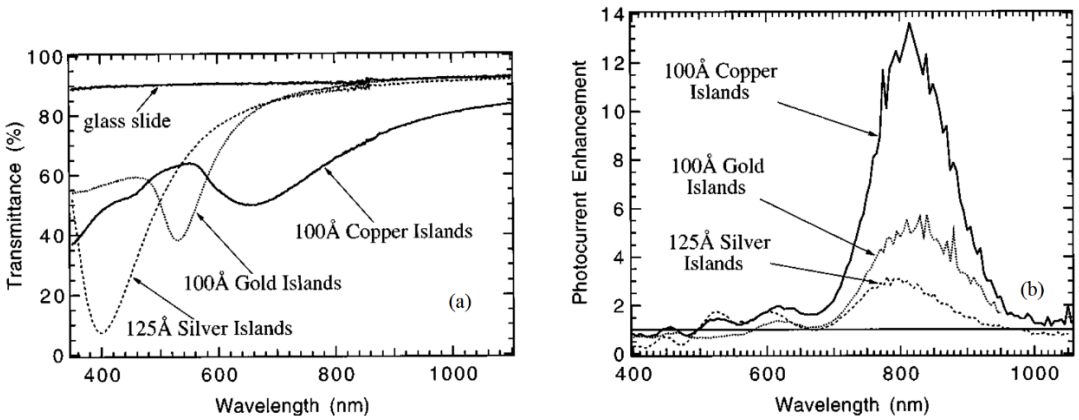

Figure 7.10: (a) transmittance of metal nanoparticles deposited on glass slides. (b) Photocurrent enhancements due to the presence of nanoparticles [109].

Increasing the size of the nanoparticles by controlling the deposition process resulted in further improved photocurrent enhancement to nearly 20-fold for silver nanoparticles [148]. This is due to enhanced dipole oscillations of the nanoparticles and enhanced interaction with the waveguide modes [141]. However, the metal nanoparticles show apparent negative effect on the photocurrent enhancement in the light wavelength range from 400 nm to 550 nm, which

corresponds to the strongest band of the spectrum of solar radiation. This negative effect is due to the parasitic absorption near the plasmon resonance frequency of the metal nanoparticles. And this effect would overcompensate the gains obtained at longer wavelength range [143].

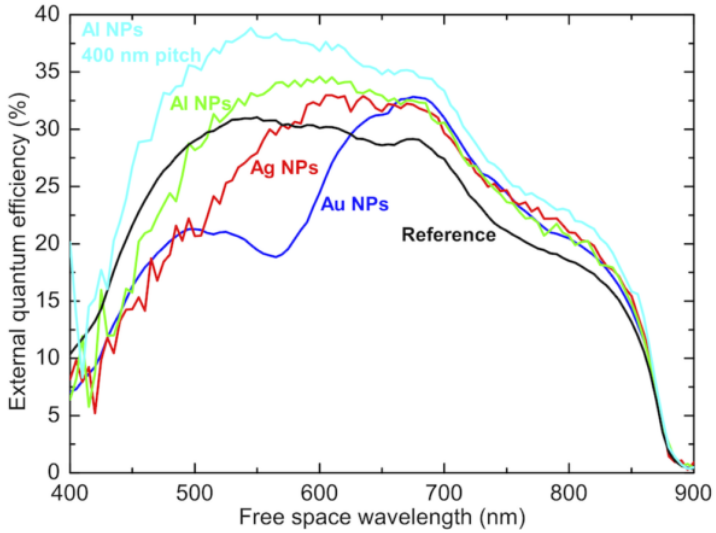

Figure 7.11: Broadband enhancement of a GaAs solar cell by Al nanoparticles [145].

Shifting the plasmon resonance frequency to the ultraviolet is an effective approach to eliminate the parasitic absorption loss and due to this effect broadband EQE enhancement by aluminium nanoparticles has been reported for a GaAs solar cell, as shown by the measured EQE result of the solar cell in Fig. 7.11 [145]. Further improvement of metal nanoparticle enhanced solar cells are currently under research in the directions of optimisation of the size, shape, coverage and distribution of nanoparticles, as well as the location to anchor the nanoparticles in the solar cell [149], [150].

To conclude, metal nanoparticles enhanced solar cell is a promising technique to reduce the material usage of silicon solar cells. The main disadvantage of this technique is the parasitic absorption loss in the metal material. For the Al nanoparticles reported in [145], certain geometric shape are required to achieve broadband enhancement and these nanoparticles need complex and expensive nanofabrication processes.

Lossless dielectric nanospheres such as silicon dioxide spheres were used to replace metal nanoparticles to enhance the performance of a GaAs solar cell [151] and an amorphous silicon solar cell [152]. Limited enhancements have been shown for both two types of solar cells. The coupling mechanism here is different to the dipole-waveguide interaction. The nanospheres can support whisper gallery modes which are surface waves trapped in the nanospheres by TIR and can be coupled to the waveguide modes of a proximal solar cell [153]. However, the energy

absorbed or trapped in the nanospheres are limited and the consequence is limited photocurrent enhancement of the underlying solar cell [151], [152].

Recently, via spectroscopic studies, visible to near-infrared quantum dots [154] have been proved to be good candidates for energy transfer. However, using quantum dots have similar challenges as using fluorescence molecules in energy transfer to semiconductors.

7.6 Conclusion

This chapter reviews the approaches to enhance light capture in solar cells via energy transfer from proximal fluorescent molecules, metal and dielectric nanoparticles and quantum dots. Preliminary calculation shows that dipole-like radiators such as fluorescent molecules offer great potential to couple solar radiation into underlying solar cells as trapped waveguide modes. Thus light harvesting and sensitisation by directed energy transfer from dipole-radiators to semiconductors represents a promising approach to achieve high efficiency and low cost solar energy applications. The following Chapter 8 and 9 give the theoretical and experimental demonstration of using fluorescent molecules to enhance the capture of light in silicon solar cells.

Chapter 8 Photon Tunnelling into Ultrathin Silicon Films

8.1 Introduction

Based on the results given by CPS for the fluorescence damping rate near interface, an analytical expression for the photon tunnelling rate or injection rate of waveguide modes into dielectric thin layers is obtained from the analysis of the poles of the Fresnel reflection coefficients in the complex plane of wavenumber. This chapter shows the derivation process of this analytical expression and its applications in modelling fluorescence near interface.

8.2 Photon tunnelling rate

Firstly, the photon tunnelling rate is obtained for a vertical electric dipole injecting waveguide modes into a thin layer, which can support only a single waveguide mode. Then, the analysis is expanded to horizontal electric dipoles and thick layers which can support more waveguide modes.

8.2.1 Vertical electric dipole

As shown in Fig. 8.1, a VED emits near a thin layer between two infinite media. The thickness of the thin layer is t, and the VED lies at distance d to the thin layer. The refractive index for each medium is $n_i, i=1,2,3$, respectively.

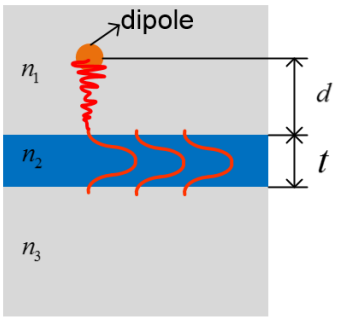

Figure 8.1: Photon tunnelling into thin layer.

The normalised damping rate for a VED near a single interface in the CPS theory is given by Eq. (7.4) and rewritten here as

$$\hat{b}_{\mathrm{VED}} = \frac{b_{\mathrm{VED}}}{b_0} = 1 - q + \frac{3q}{2}\mathrm{Re}\left(\frac{1}{k_1^3}\int_0^\infty dk_\rho \frac{k_\rho^3}{k_{1x}}\left[1 + r^{\mathrm{TM}} \exp(i2k_{1x}d)\right] \right) \tag{8.1}$$

where b_0 is the damping rate in the absence of any interface, q the quantum yield, $k_1 = n_1 k_0$ the wavenumber in layer 1, k_0 the wavenumber in vacuum, k_ρ the in-plane wavenumber, $k_{1x} = \sqrt{k_{10}^2 - k_\rho^2}$ the wavenumber component in the x direction (perpendicular to the interface)

and r^{TM} the reflection coefficient for TM waves at the interface between layer 1 and layer 2, which is given by Airy's summation in the form of

$$r^{\mathrm{TM}} = \frac{-r_{21}^{\mathrm{TM}} + r_{23}^{\mathrm{TM}} e^{i2\phi}}{1 - r_{21}^{\mathrm{TM}} r_{23}^{\mathrm{TM}} e^{i2\phi}} = \frac{g(k_\rho)}{f(k_\rho)} \tag{8.2}$$

where r_{ij}^{TM} is the Fresnel reflection coefficient for the TM waves at the interface of layer i and j, respectively, $\phi = k_{2x} t$ the phase shift for light travelling through layer 2. In Eq. (8.2), $g(k_\rho)$ and $f(k_\rho)$ were introduced to represent the numerator and the denominator, respectively. It is apparently that Eq. (8.2) has singularities when $f(k_\rho) = 0$, it has been found that these singularities are the poles in the complex plane of the in-plane wavenumber, which physically corresponds to the waveguide modes supported by the thin layer [155].

To obtain an analytical expression for the photon tunnelling rate, we first limit our discussion to the case that the thin layer can only support a single TM waveguide mode. The single solution of $f(k_\rho) = 0$ is $k_\rho = k_{\rho wg}$ (the subscript wg stands for waveguide), where $k_{\rho wg}$ is the in-plane wavenumber of the single TM waveguide mode. The Fresnel reflection coefficients for TM waves are given by

$$r_{21}^{\mathrm{TM}} = \frac{n_1^2 k_{2x} - n_2^2 k_{1x}}{n_1^2 k_{2x} + n_2^2 k_{1x}} \tag{8.3}$$

$$r_{23}^{\mathrm{TM}} = \frac{n_3^2 k_{2x} - n_2^2 k_{3x}}{n_3^2 k_{2x} + n_2^2 k_{3x}} \tag{8.4}$$

where $k_{2x} = \sqrt{k_{20}^2 - k_\rho^2}$, $k_{3x} = \sqrt{k_{30}^2 - k_\rho^2}$. For the trapped modes in the silicon layer $k_\rho > k_{10}$, both k_{1x} and k_{3x} are imaginary, while k_{2x} is real. The amplitude of the Fresnel reflection coefficients approximate unity (the trivial extinction coefficient of silicon is neglected), i.e. $|r_{21}| \approx |r_{23}| \approx 1$. Then $f(k_\rho)$ can be rewritten as

$$f(k_\rho) \approx 1 - \exp\left[i(2k_{2x}t - 2\phi_{21} - 2\phi_{23})\right] \tag{8.5}$$

where the phase angles are given by

$$\phi_{21} = \arctan\left(\frac{n_2^2 |k_{1x}|}{n_1^2 k_{2x}}\right) \tag{8.6}$$

$$\phi_{23} = \arctan\left(\frac{n_2^2 |k_{3x}|}{n_3^2 k_{2x}}\right) \tag{8.7}$$

Equation (8.5) can be expanded in the vicinity of $k_{\rho wg}$ as

$$f(k_\rho) = f(k_{\rho wg}) + f'(k_{\rho wg})(k_\rho - k_{\rho wg}) + \ldots \tag{8.8}$$

For the waveguide mode $f(k_{\rho wg}) = 0$, and then one can have the approximation

$$f(k_\rho) \approx f'(k_{\rho wg})(k_\rho - k_{\rho wg}) \tag{8.9}$$

From Eq. (8.8) we obtain

$$f'(k_{\rho wg}) = 2i\left\{k_\rho\left[\frac{t}{k_{2x}} + \frac{\varepsilon_1\varepsilon_2\left(|k_{1x}|^2 + k_{2x}^2\right)}{\varepsilon_1^2 |k_{1x}| k_{2x}^3 + \varepsilon_2^2 |k_{1x}|^3 k_{2x}} + \frac{\varepsilon_3\varepsilon_2\left(|k_{3x}|^2 + k_{2x}^2\right)}{\varepsilon_3^2 |k_{3x}| k_{2x}^3 + \varepsilon_2^2 |k_{3x}|^3 k_{2x}}\right]\right\} \tag{8.10}$$

where all the wavenumber components k_ρ, $k_{ix}, i = 1,2,3$ are evaluated at $k_\rho = k_{\rho wg}$. Assuming a unity quantum yield, the damping rate in the evanescent waves or the photon tunnelling (pt) rate can be obtained from Eq. (8.1) by changing the integral interval to $k_{10} < k_\rho < k_{20}$ and it is given by

$$\hat{b}_{\mathrm{VED}}^{pt} = \frac{3}{2}\mathrm{Im}\left\{\frac{1}{k_1^3}\int_{k_{10}}^{k_{20}} dk_\rho \frac{k_\rho^3}{|k_{1x}|}\frac{g(k_\rho)}{f'(k_{\rho wg})(k_\rho - k_{\rho wg})}\exp(-2|k_{1x}|d)\right\} = \mathrm{Im}\int_{k_{10}}^{k_{20}} F(k_\rho)dk_\rho \tag{8.11}$$

where $F(k_\rho)$ represents the integrand. It is apparent that Eq. (8.11) is an integral with a simple pole $k_\rho = k_{\rho wg}$ on the integration path. Applying the residue theory [156], this integral is given by the sum of its principal value and the contribution from the simple pole in the form of

$$\hat{b}_{\mathrm{VED}}^{pt} = \mathrm{Im}\left(P\int_{k_{10}}^{k_{20}} F(k_\rho)dk_\rho\right) + \mathrm{Im}\int_\gamma F(k_\rho)dk_\rho \tag{8.12}$$

where the first integral is the principal value of the integral, and the second integral, which represents the contribution from the simple pole, is a contour integral along a semicircle γ with radius R approaching zero, as shown in Fig. 8.2. The indented path was chosen to avoid the pole on the real axis. Note that here the semicircle is chosen below the real axis, because that the pole slightly moved up from the real axis if one considers the trivial extinction coefficient of silicon.

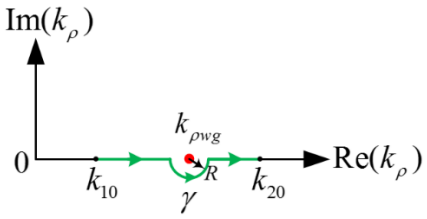

Figure 8.2: Indented integration contour for the damping rate in the waveguide mode.

Introducing $Re^{i\theta} = k_\rho - k_{\rho wg}$, $dk_\rho = iRe^{i\theta}d\theta$, the integral along γ can be written as

$$\begin{aligned}\int_\gamma F(k_\rho)dk_\rho &= \frac{3}{2}\mathrm{Im}\left\{\frac{1}{k_1^3}\frac{k_{\rho wg}^3}{|k_{1xwg}|}\frac{g(k_{\rho wg})}{f'(k_{\rho wg})}\exp(-2|k_{1xwg}|d)\int_\pi^{2\pi}\frac{1}{Re^{i\theta}}iRe^{i\theta}d\theta\right\} \\ &= \frac{3}{2}\mathrm{Im}\left\{\frac{1}{k_1^3}\frac{k_{\rho wg}^3}{|k_{1xwg}|}\frac{g(k_{\rho wg})}{f'(k_{\rho wg})}\exp(-2|k_{1xwg}|d)\pi i\right\}\end{aligned} \tag{8.13}$$

where k_{1xwg} is the wavenumber component k_{1x} evaluated at $k_\rho = k_{\rho wg}$. While for the principal value of the integral, it can be found to be zero. If one examine the imaginary part of the reflection coefficient given by Eq. (8.2) for the electromagnetic waves with $k_\rho > k_{10}$ and $k_\rho > k_{30}$, one can find

$$\mathrm{Im}(r) \approx \frac{[1-\exp(-4\phi_i)]\sin(2\phi_{21})}{[1-\exp(-2\phi_i)]^2 + 2\exp(-2\phi_i)[1-\cos(2\phi_r - 2\phi_{21} - 2\phi_{23})]} \tag{8.14}$$

where ϕ_r, ϕ_i are the real and imaginary part of $\phi = k_{2x}t = \phi_r + i\phi_i$, respectively. Note that the superscript of r is removed since this approximation has no dependence on light polarisation. Neglecting the trivial extinction coefficient of silicon leads to $\phi_i \sim 0$, and then $\mathrm{Im}(r) \sim 0$. So the principle value of the integral in Eq. (8.12) equals to zero. Physically, this result is also apparent since that there is no reflected wave originates from the waves trapped inside the waveguide. Finally, the photon tunnelling rate can be written as

$$\hat{b}_{\mathrm{VED}}^{pt} = \frac{3}{2k_1^3}\frac{k_{\rho wg}^3}{|k_{1xwg}|}\mathrm{Im}\left[\frac{g(k_{\rho wg})\pi i}{f'(k_{\rho wg})}\right]\exp(-2|k_{1xwg}|d) \tag{8.15}$$

where

$$g(k_\rho) = 4i\frac{\varepsilon_1\varepsilon_2|k_{1x}|k_{2x}}{\varepsilon_2^2|k_{1x}|^2 + \varepsilon_1^2 k_{2x}^2} \tag{8.16}$$

and all the wavenumber components are evaluated at $k_\rho = k_{\rho wg}$. Since $f'(k_\rho)$ and $g(k_\rho)$ are both pure imaginary, Eq. (8.15) can be simplified as

$$\hat{b}_{\mathrm{VED}}^{pt} \approx \frac{3\pi}{2k_1^3}\frac{k_{\rho wg}^3}{|k_{1xwg}|}\frac{g_{\mathrm{TM}}(k_{\rho wg})}{f'_{\mathrm{TM}}(k_{\rho wg})}\exp(-2|k_{1xwg}|d) \tag{8.17}$$

where the subscript TM is introduced to distinguished with the following results for TE polarisation. To validate this simple expression, the exact numerical result of Eq. (8.1) is compared with Eq. (8.17) in Fig. 8.3 for a VED emitting near a thin silicon layer with thickness of 30 nm, which supports a single TM waveguide mode at the wavelength of 566 nm.

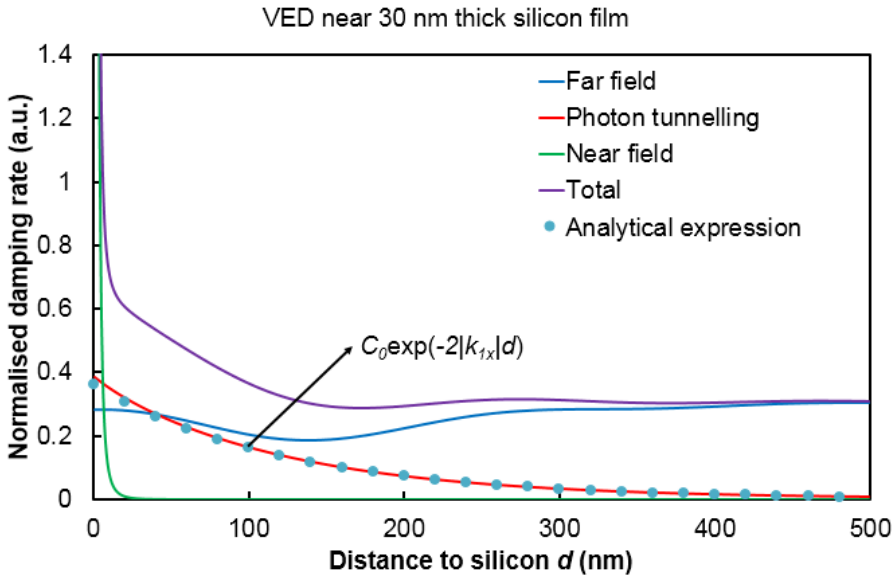

Figure 8.3: Photon tunnelling rate comparison with exact theory.

In Fig. 8.3, C_0 is a constant determined by the waveguide parameters given in Eq. (8.17). It is shown that the numerical results of the simple analytical expression agrees well with the exact result. It is seen from the above derivation process that there is no reason to limit the photon tunnelling rate to the case that the thin layer only supports a single waveguide mode. For thicker layers which can support more than one waveguide mode, the photon tunneling rate can be express as

$$\hat{b}_{\mathrm{VED}}^{pt} \approx \sum_{m=0}^{N}\frac{3\pi}{2k_1^3}\frac{k_{\rho m}^3}{|k_{1xm}|}\frac{g_{\mathrm{TM}}(k_{\rho m})}{f'_{\mathrm{TM}}(k_{\rho m})}\exp(-2|k_{1xm}|d) \tag{8.18}$$

where m is the waveguide mode index number, N the number of waveguide modes that the thin layer can support and all the wavenumbers are evaluated at respect waveguide mode in-plane wavenumbers.

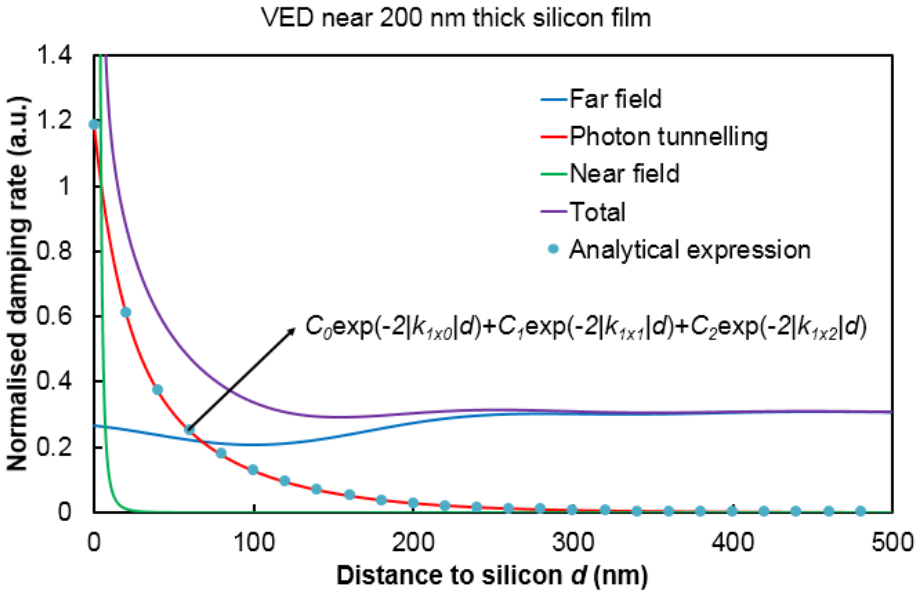

Figure 8.4: Photon tunnelling rate comparison with exact theory.

Figure 8.4 shows the comparison of the numerical result of Eq. (8.18) with the exact numerical result given by Eq. (8.1) for a thin layer with thickness of 200 nm, which can support three TM waveguide modes at the wavelength of 566 nm. In Fig. 8.4, $C_m, m = 0,1,2$ are constants. The good fit between the analytical expression and the exact numerical results verifies that the analytical expression for the photon tunnelling rate can be extended to thicker layers which support more than one waveguide mode.

8.2.2 Horizontal electric dipole

Similar analysis can be extended to HEDs, and the photon tunnelling rate can be given in a similar form as

$$\begin{aligned}\hat{b}_{\mathrm{HED}}^{pt} \approx & \sum_{m=0}^{N_{\mathrm{TM}}} \frac{3\pi}{4k_1^3} \left|k_{1xm}^{\mathrm{TM}}\right| k_{\rho m}^{\mathrm{TM}} \frac{g_{\mathrm{TM}}(k_{\rho m}^{\mathrm{TM}})}{f'_{\mathrm{TM}}(k_{\rho m}^{\mathrm{TM}})} \exp(-2\left|k_{1xm}^{\mathrm{TM}}\right| d) \\ & + \sum_{m=0}^{N_{\mathrm{TE}}} \frac{3\pi}{4k_1} \frac{k_{\rho m}^{\mathrm{TE}}}{\left|k_{1xm}^{\mathrm{TE}}\right|} \frac{g_{\mathrm{TE}}(k_{\rho m}^{\mathrm{TE}})}{f'_{\mathrm{TE}}(k_{\rho m}^{\mathrm{TE}})} \exp(-2\left|k_{1xm}^{\mathrm{TE}}\right| d)\end{aligned} \tag{8.19}$$

where N_{TM} and N_{TE} are the number of TM and TE waveguide modes that the thin layer can support, and

$$f'_{\mathrm{TE}}(k_{\rho wg}) = 2i\left[\frac{k_\rho}{k_{2x}}\left(t + \frac{1}{|k_{1x}|} + \frac{1}{|k_{3x}|}\right)\right] \tag{8.20}$$

and

$$g_{\mathrm{TE}}(k_{\rho wg}) = 4i\frac{|k_{1x}|k_{2x}}{k_2^2 - k_1^2} \tag{8.21}$$

Note that HED can inject both TM and TE waveguide modes into thin layers. A special case is a HED emitting near a thin layer, which is sandwiched by two identical materials. At this condition, the photon tunnelling rate into the TE modes can be simplified as

$$\hat{b}_{\mathrm{HED}}^{pt}\Big|_{\mathrm{TE}} \approx \sum_{m=0}^{N_{\mathrm{TE}}} \frac{3\pi}{2k_1} \frac{|k_{1xm}|\left(k_2^2 - k_1^2 - |k_{1xm}|^2\right)}{\left(k_2^2 - k_1^2\right)\left(t|k_{1xm}| + 2\right)} \exp(-2|k_{1xm}|d) \tag{8.22}$$

This expression is used to calculate the energy transfer probability from dipole to nearby thin waveguides in Sec. 8.3.2.

8.3 Application of photon tunnelling rate

8.3.1 Fluorescence lifetime near thin layers

Since light harvesting only happens at dipole-thin layer in the order of a few nanometres, which is easily surpassed in practical experiments, the analytical expressions for the photon tunnelling rate can be combined with the far field damping rate to model fluorescence lifetime near thin layers.

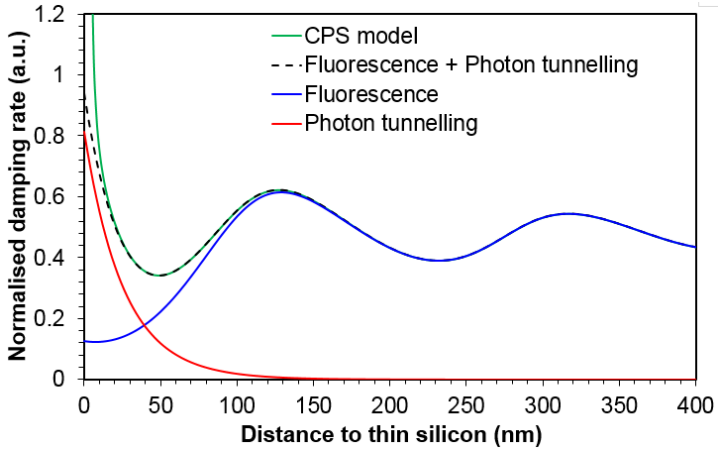

Figure 8.5: Fluorescence damping rate near a 25 nm thick silicon film.

Figure 8.5 shows the modelling result for the damping rates of a HED emitting at 566 nm in air and near a thin silicon layer with the thickness of 25 nm, which supports a single TE waveguide mode at 566 nm. The damping rate of fluorescence in the far field is obtained by evaluating the power spectrum given by Eq. (7.9) in the wavenumber interval of $k_\rho < k_1$, while the tunnelling rate into the single TE mode is obtained by evaluating Eq. (8.22). It is seen that the sum of the damping rate in the far field and the photon tunnelling rate well reproduces the exact result of

the CPS model for dipole-silicon distance beyond 10 nm. This result is compared with experimentally measured fluorescence lifetimes in the following chapter.

8.3.2 Energy transfer probability

One may wonder that what the thinnest thickness of silicon is needed to accept the energy transferred from the dipole radiators. The dependence of the energy transfer probability, which is the ratio of the photon tunnelling rate and the total damping rate of the dipole, on the thickness of silicon thin film is calculated for the structure showing in Fig. 8.1, where n_1 and n_3 are the refractive index of silicon dioxide, and n_2 is that for silicon. The numerical results are shown in Fig. 8. 6. In the calculations, the dipole is chosen at a distance of 30 nm to the surface of the silicon film. And the wavelength of light in consideration is at 566 nm.

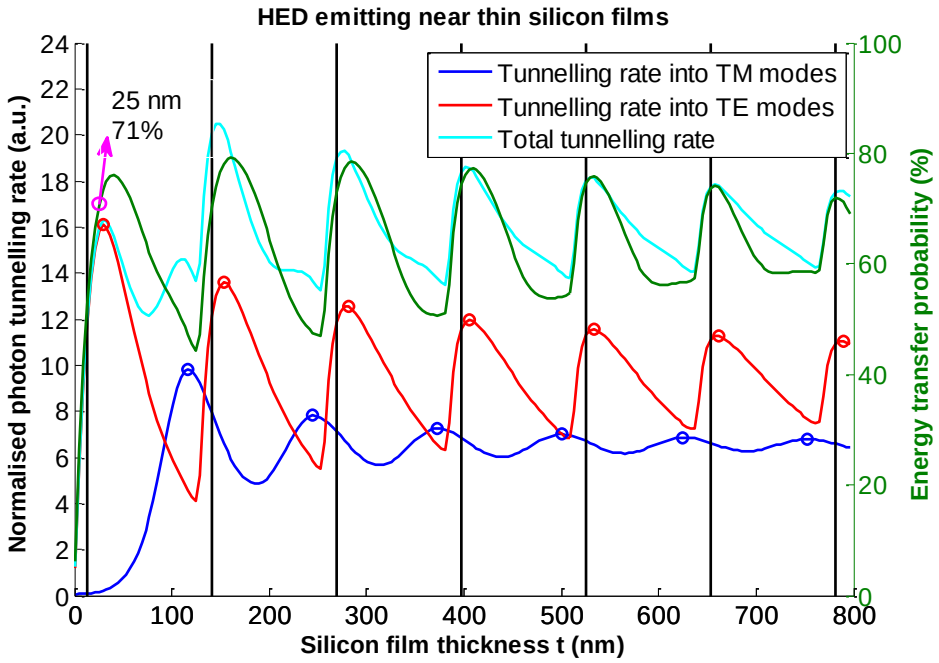

Figure 8.6: Dependence of energy transfer probability on the thickness of silicon.

In Fig. 8.6, the blue and red curves show the normalised tunnelling rate into TM and TE waveguide modes, respectively, while the cyan curve shows the sum of these two contributions. The green curve shows the energy transfer probabilities. And the vertical black lines shows the cut-off thickness of TE modes with mode index number increasing from left to right.

It is seen that the major peaks of the energy transfer probability are due to the contribution of the photon tunnelling rate into the TE waveguide modes, while the less-prominent peaks are due to that for the TM waveguide modes. It is also seen that the energy transfer probability has local maximum values when the thickness of silicon is slightly larger than the cut-off thickness. The reason for this result given in [10] is that near the cut-off condition the waveguide mode is

least trapped in silicon film and the probability to interact with the dipole is maximised. This explanation is qualitative and here we use the analytical expression for the photon tunnelling rate to illustrate this phenomenon quantitatively. Near the mode cut-off thickness, the photon tunnelling rate can be approximated from Eq. (8.22) as

$$\hat{b}_{\mathrm{HED}}^{pt}\Big|_{\mathrm{TE}} \approx \frac{3\pi}{2k_1 t}\sum_{m=0}^{N_{\mathrm{TE}}}\frac{k_2^2-k_1^2-k_{1xm}^2}{k_2^2-k_1^2}\exp(-2\left|k_{1xm}\right|d) \tag{8.23}$$

For the internal trapped waveguide modes, the in-plane wavenumber satisfies $k_{\mathrm{SiO_2}} < k_\rho < k_{\mathrm{Si}}$. Near the mode cut-off condition, $k_\rho \to k_{\mathrm{SiO_2}}$, and $\left|k_{1x}\right|^2 \to 0$. Clearly, the exponential term in the photon tunnelling rate reaches the maximum value when $\left|k_{1x}\right|^2 \to 0$. To verify this approximations, we calculate the dependence of the exact normalised photon tunnelling rate on the normalised in-plane wavenumber and the numerical results are shown in Fig. 8.7 for the thin silicon films which have local maximum energy transfer probabilities.

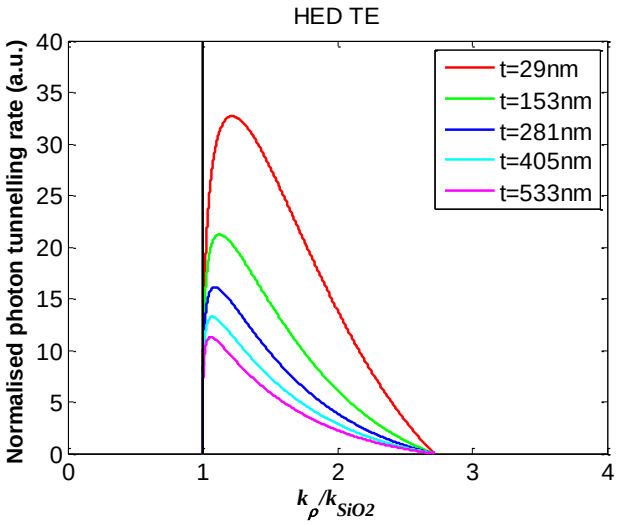

Figure 8.7: Dependence of photon tunnelling rate on in-plane wavenumber.

It is shown in Fig. 8.7 that the photon tunnelling rate has maximum value when $k_\rho \to k_{\mathrm{SiO_2}}$. So near the mode cut-off condition, the photon tunnelling rate reach local maximum values. This is the reason for the local peaks of the energy transfer probability shown in Fig. 8.6.

The numerical results shown in Fig. 8.6 also indicate that the energy transfer probability to a 25 nm thick silicon film is over 70%. This indicates efficient energy injection to a proximal ultrathin silicon film via photon tunnelling from the dipole. Thus this system bears substantial potential for photovoltaic applications.

8.4 Conclusion

This chapter shows the theoretical derivation process of an analytical expression for the photon tunnelling rate into a proximal thin dielectric layer. The applications of this tunnelling rate in modelling fluorescence lifetime and energy transfer efficiency into thin layers are illustrated. Numerical calculations of this expression indicate that the energy transfer process is efficient even when the underlying thin silicon layer is merely 25 nm thick. This expression represents a useful tool in modelling fluorescence near thin films and it is shown in the following chapter that it also agrees well with experiments.

Chapter 9 Experiments and Results of Fluorescence near Interface

This chapter has been published in part as:

L. Danos, N. Alderman, L. Fang, T. Markvart, "Silicon sensitization using light harvesting layers," in *Proceedings of the 10th Photovoltaic Science Application and Technology Conference*, Loughborough University, Loughborough, UK, 2014.

9.1 Introduction

In order to study molecular fluorescence and energy transfer from excited dye molecules near semiconducting surface, a carbocyanine dye was deposited at different distance to the surface of copper, bulk silicon and ultrathin silicon films by the Langmuir-Blodgett (LB) technique [157]. The distance was controlled either by depositing pure stearic acid LB monolayers or silicon dioxide by Plasma-Enhanced Chemical Vapour Deposition (PECVD). Time-Correlated Single Photon Counting (TCSPC) technique [158] was used to study the fluorescence properties of the dye molecules near the different substrate surfaces. The measured fluorescence lifetime results were compared with the photon tunnelling model described in Chapter 8.

9.2 Langmuir-Blodgettry

The LB technique is an easy way of fabricating molecular layered structures of well-defined morphology. It has been adopted by Drexhage in the studies of molecular fluorescence at different distance to the surface of metal mirrors [114]. A fatty acid monolayer has a typical thickness of 2.5 nm [157], so the distance can be well-controlled. Amphiphilic fluorescent molecules can be doped in one of the monolayers, so the intermolecular energy transfer can be minimised. This section introduces the principle and application of the LB technique.

9.2.1 Langmuir monolayer

A Langmuir monolayer is formed by amphiphilic molecules trapped at the interface between air and water. Amphiphilic molecules consist of a hydrophilic part that pulls the molecule towards water, and a hydrophobic part that pulls the molecule towards air. The balance between these two forces makes the molecules trapped at the air-water interface as shown in Fig. 9.1. When compressing the barriers, an ordered monolayer of these molecules forms at the interface. The film formed in such a way is called a Langmuir monolayer.

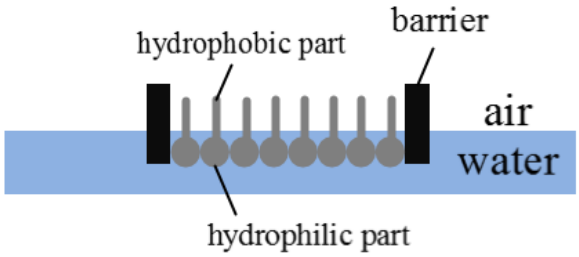

Figure 9.1: Langmuir monolayer formed at air-water interface.

9.2.2 Surface tension and surface pressure

Surface tension is an important quantity to understand monolayer formation on water surface. Water molecules at the surface of water are not surrounded by similar molecules in all directions, so there is a net attractive force towards the bulk. This net force causes the surface of water to contract, and work needs to be done to extend the surface area. Thus, a free energy is possessed by the molecules at the surface. The free energy per unit area of the surface (or equivalently, the force per unit length along the surface of water) is known as the surface tension. At Standard Temperature and Pressure (STP, 298K, 1 atmosphere), the surface tension for water is 72.8 mN/m [157]. When a Langmuir monolayer is formed at the surface of water and external force is applied to compress the monolayer, the repulsive force on one another of the molecules reduces the surface tension. A surface pressure is defined as

$$\Pi = \gamma - \gamma_0 \tag{9.1}$$

where γ is the surface tension of the monolayer covered surface and γ_0 the surface tension of pure water surface.

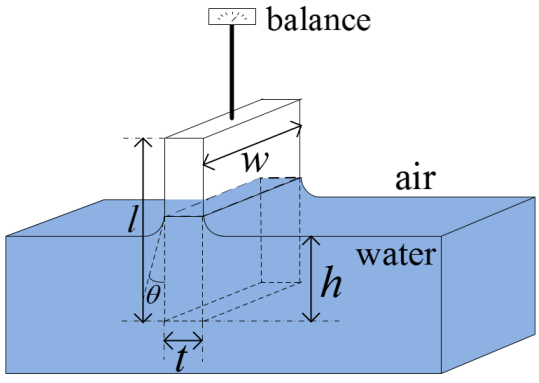

Figure 9.2: A Wilhelmy plate suspend to a balance in surface pressure measurement [157].

As shown in Fig. 9.2, the surface pressure is measured by suspending a Wilhelmy plate to a sensitive balance and across the air-water interface. The force applied to the balance are the gravity of the plate and surface tension acting downwards into bulk water and buoyancy acting upwards due to displaced water and it is given by

$$F = \rho_W glwt + 2\gamma(w+t)\cos\theta - \rho_L ghwt \tag{9.2}$$

where ρ_W and ρ_L are the density of the Wilhelmy plate and the liquid water, respectively, g the gravitational constant, θ the contact angle, l, w, t the dimensions of the plate, h the length of the plate immersed in water. In experiments, a rectangular piece of chromatography paper ($w = 1$ cm, $h = 2$ cm) is used as the Wilhelmy plate. The surface of the paper is totally wetted by water, so the contact angle $\theta = 0$. Neglecting the trivial thickness of the Wilhelmy plate, the change of the force applied on the balance is directly proportional to the change of the surface tension (in the unit of mN/cm)

$$\Delta\gamma = \frac{\Delta F}{2} \tag{9.3}$$

The force applied to the balance is calibrated to be zero by measuring the surface tension of pure water. After spreading and compressing the Langmuir monolayer, the measured force directly gives the surface pressure.

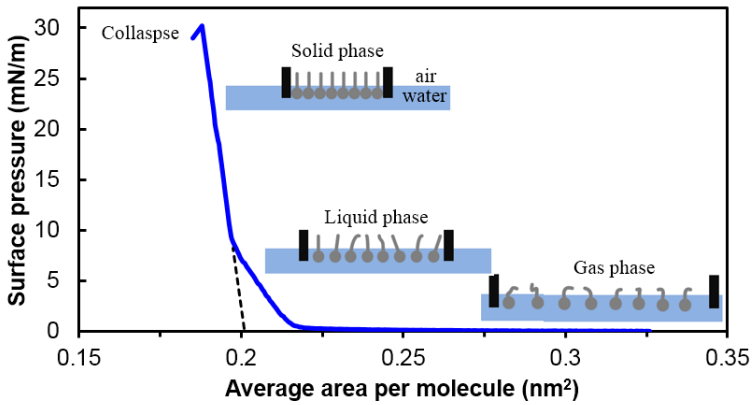

Figure 9.3: Measured isotherm of stearic acid at STP condition.

The dependence of the surface pressure on the average area per molecule occupied (obtained by dividing the number of molecules to the area of the monolayer) at a constant temperature is called the isotherm of the amphiphilic molecule. From the characteristics of isotherm, the surface pressure can be determined for LB films deposition. After initial spreading on water, the amphiphilic molecules orient randomly and behave like two-dimensional gas, as shown in Fig. 9.3. When external compressing is applied, some of the molecules start to align perpendicularly to the surface of water and the monolayer behaves like two-dimensional liquid. With continued compression, all of the molecules align perpendicularly and the gaps between molecules decrease quickly as the surface pressure rises. The monolayer behaves like solid and the LB films are deposited onto substrates at this phase. Upon further compression, the monolayer collapses. Figure 9.3 shows the measured isotherm of the stearic acid used in this work at STP condition.

9.2.3 Langmuir-Blodgett technique

The LB films are deposited on substrates by dipping/withdrawing the substrate vertically into the monolayer formed on water while maintaining the surface pressure at the solid phase of the isotherm.

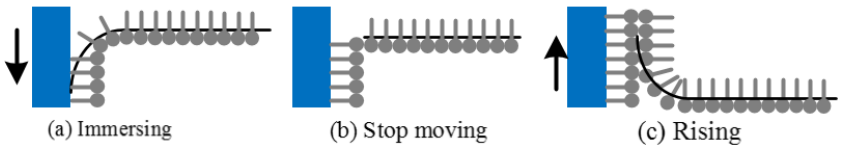

Figure 9.4: Deposition of first LB bilayer on a hydrophobic surface.

Figure 9.4 shows the deposition process of the first two LB layers onto a hydrophobic surface. The initial layer is deposited with the hydrophobic part of the amphiphilic molecules attached to the substrate surface. After an initial monolayer is deposited, the substrate surface turns to be hydrophilic. A second layer is deposited when the substrate is withdrawn, and the hydrophilic part of the amphiphilic molecules are attached to the substrate. Multilayers are deposited by repeating the immersion and withdraw processes.

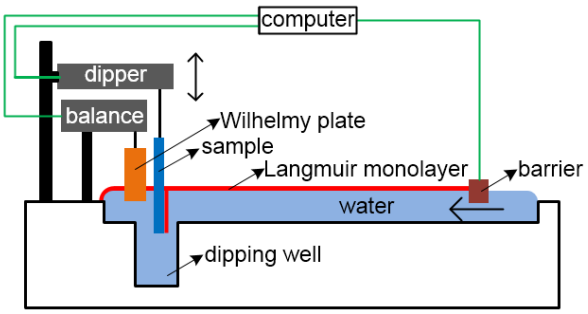

Figure 9.5: Schematic of a typical LB trough.

The equipment used to deposit LB films is called the LB trough. The schematic of a typical LB trough is shown in Fig. 9.5. Initially, the barrier, which is driven by a computer-controlled motor, keeps compressing the monolayer until the surface pressure measured by the Wilhelmy plate reaches the desired value. Then, the dipper, which is driven by another motor and moving at a constant speed, takes the sample down and up through the monolayer to deposit the LB films on the sample.

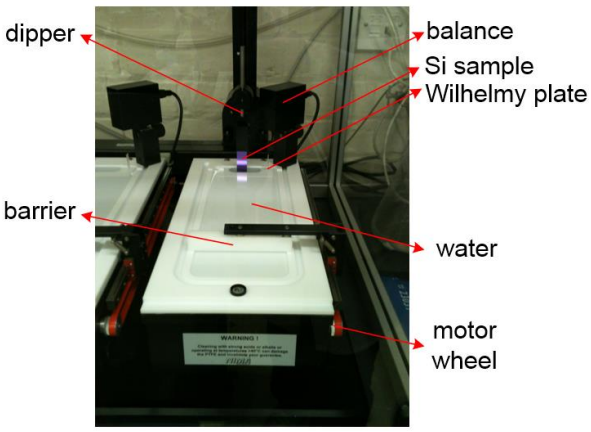

Figure 9.6: Photograph of the LB trough.

The LB trough used in this work is from NIMA Technology, UK. Figure 9.6 shows the photograph of the trough in deposition process. The surface of the trough is made of polytetrafluoroethylene (PTFE), so it is chemically inert and hydrophobic, which facilitates cleaning by solvents such as chloroform. To prevent leakage of the monolayer under the barrier when compressing, the barrier is chosen to be made of a hydrophilic material Delrin. The sensitive balance and the motors which drive the barrier and the dipper are connected to a computer and controlled by the software NIMA TR516.

9.2.4 Material for Langmuir-Blodgett films

The ultra-pure water used was De-ionised (DI) water from a Sartorius reverse osmosis water system (ARIUM-UV) with a resistivity of 18.2 Mohm·cm and with a total organic content of less than 2 ppb. The water purity is of crucial importance to the formation of stable monolayers, since contaminations make the monolayer collapse before the surface pressure reach the solid phase surface pressure. The amphiphilic molecule used in this work is a Stearic Acid (SA, $CH_3(CH_2)_{16}COOH$) with the chemical structure shown in Fig. 9.7. The hydrophilic part is the carboxylic acid, and the hydrophobic part is the hydrocarbon chain.

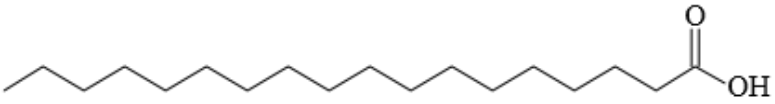

Figure 9.7: Chemical structure of stearic acid.

After spreading on water, the carboxylic acid group of SA become ionised and there is strong repulsion between adjacent acid groups, which deteriorates the formation of stable monolayers. To reduce the repulsion force, divalent metal ions were introduced to water. In this work, cadmium chloride was used and the concentration in water was 5×10^{-4} mol/L. The pH value of water was measured to be 5.5 by a Mettler Toledo Seven Easy pH meter, which is the pH value for a carbon dioxide saturated water [114]. The fluorescent molecule used in this work was a

long chain carbocyanine dye 1,1'-Dioctadecyl-3,3,3',3'-Tetramethylindocarbocyanine Perchlorate (from now on called DiI) purchased from Life Technologies.

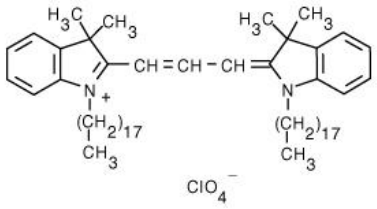

Figure 9.8: Chemical structure of the DiI dye.

Figure 9.8 shows the chemical structure of the DiI dye. Figure 9.9 shows the excitation and emission spectra of the DiI dye in chloroform with concentration of 2×10^{-6} mol/L, which were measured by a Varian Cary Eclipse 300 fluorescence spectrophotometer.

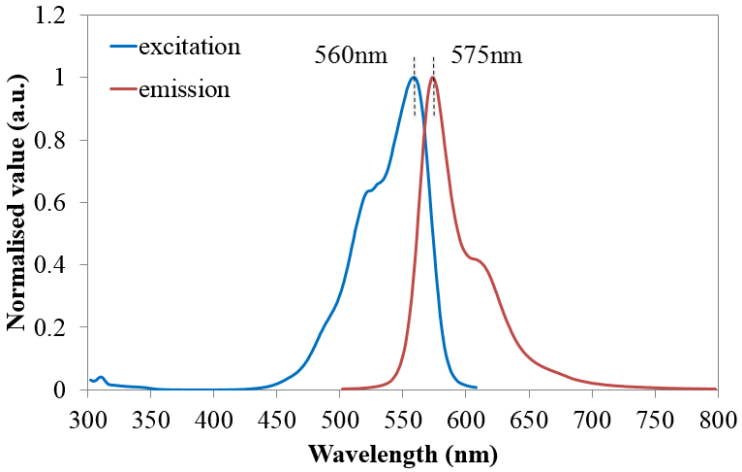

Figure 9.9: Excitation and emission spectra of DiI dye in chloroform.

All the chemicals, cadmium chloride, chloroform and hexamethyldisilazane (HMDS) were from Sigma-Aldrich at the highest purity available, and they were used without further purification. Monocrystalline silicon wafers were from Soitec (100 orientation, P type, resistivity of 1-30 ohm·cm). Silicon-On-Insulator (SOI) wafers were also from Soitec (silicon thickness 1400 nm, silicon dioxide thickness 1000 nm). Standard microscopic glass slides were from Corning. High purity (99.9999%) copper sputtering target were obtained from Kurt J. Lesker.

9.2.5 Substrate preparation

Copper was deposited on silicon wafer by a Kurt J. Lesker magnetron sputtering system. The sputtering chamber was evacuated to 2.4×10^{-7} mBar before Argon was introduced inside. The sputtering process last 10 min with input DC power at 100 W. The rotation speed of the silicon wafer was 10 rpm. The thickness of the sputtered copper film was measured by ellipsometry and the result was 100±5 nm.

Silicon dioxide of different thicknesses were deposited on silicon wafers by a PECVD system made by Oxford Instruments. The chamber was evacuated to 1000 mTorr before the introduction of silane, nitrogen and nitrous oxide. The ratio of these gases were well tuned to achieve the silicon dioxide deposition rate around 1 nm/s with input RF frequency at 13.56 MHz and power at 20 W.

The ultrathin silicon film substrates with thickness of 25±5 nm were processed from the SOI wafers by thermal oxidation of the top silicon layer in the SNC cleanroom. Then the thermal oxide was removed by hydrofluoric acid (mixture of acid and water with volume ration of 7:1).

The cleaning process of all the glass and silicon substrates were completed in three steps [126], [127]: firstly, substrates were soaked in freshly prepared Piranha solution (mixture of 99% sulphuric acid and 30% hydrogen peroxide with volume ratio of 4:1) for 1 hour; then the substrates were rinsed with DI water and transferred to a staining dish filled with DI water, and the staining dish was left in a ultrasonic for 1 hour; lastly, the substrates were taken out from the staining dish and dried with compressed nitrogen gas.

All the glass, copper and silicon substrates were exposed to HMDS gas to render the surface hydrophobic before the deposition of LB films [126], [127]. This step is important, without which the LB films may peel off the substrate after several monolayers were deposited. Practically, the substrates were left in a staining dish overnight with a few drops of HMDS added inside.

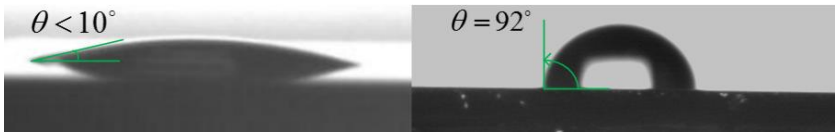

Figure 9.10: Water contact angle of silicon substrate before and after HMDS treatment.

To verify the effectiveness of this approach, contact angle of the silicon substrate surface was measured by a goniometer (Kruss DSA 100) using a DI water drop with the volume of 1 microliter. The measured results show that the contact angle increased from less than 10 degrees to 92±2 degrees after HMDS treatment, which indicates that the surface after HMDS treatment is highly hydrophobic. And no peer off phenomenon has been observed after 50 monolayers were deposited on HMDS treated silicon substrates.

9.2.6 LB films deposition

DiI was mixed with stearic acid in chloroform with molar ratio of 1:100. The concentration of the spreading solution of DiI:SA and pure SA were both 5×10^{-4} mol/L in chloroform. The spreading solutions were added dropwisely to the surface of water. The monolayers were deposited at the

rate of 10 mm/min and while deposition the surface pressure of the monolayer was maintained at 27 mN/m.

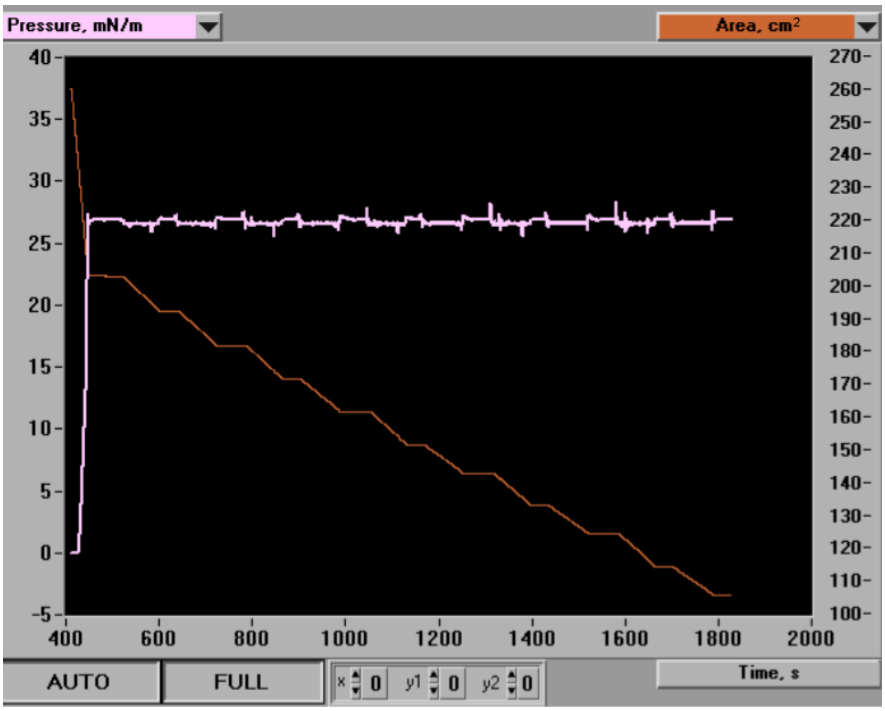

Figure 9.11: Surface pressure and monolayer area dependence on time.

A typical deposition process is shown in Fig. 9.11, which is a screenshot of the controlling software of the LB trough (NIMA TR516). The surface pressure and the area of the monolayer were plotted against time for the deposition process of 10 monolayers on a silicon substrate. It is seen that the surface pressure maintained at the target pressure during the whole deposition process, and the area of the monolayer area decreased linearly against time in each deposition step. The decreased monolayer area is almost identical in each step, which suggests that the coverage of monolayers on the substrate is uniform. The film transfer ratio, obtained by dividing the decreased film area on water to the sample area, was calculated to be larger than 0.95 for all the LB film deposited on glass, copper and silicon substrates. This suggests that the monolayer was stable during the deposition processes and the LB films were well deposited.

9.3 Optical characterisation of thin films

The thickness and the refractive index of the deposited silicon dioxide films and the LB films were measured in the wavelength range from 200-1700 nm via a J. A. Woollam M2000D Variable Angle Spectroscopic Ellipsometry (VASE) system in the SNC cleanroom.

9.3.1 Variable angle spectroscopic ellipsometry

Ellipsometry is a non-destructive optical tool for the measurements of the thickness and optical constants of multi-layered thin films.

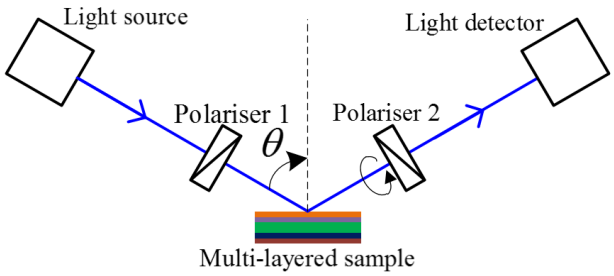

Figure 9.12: A typical setup of ellipsometer [159].

A typical ellipsometer is shown in Fig. 9.12, which consists a light source, two polarisers and a light detector. The incident light is polarised linearly by the first polariser, i.e. the amplitude and the phase of the *s* polarised component and the *p* polarised component of the incident light are identical. After reflection on the surface of the sample, the amplitude and the phase of the *s* and the *p* components change to different values and the reflected light is elliptically polarised. The reflected light travels through the continuously rotating polariser and the detector converts the transmitted light into electronic signal to map out the polarisation of the reflected light. This information can determine the ellipsometry parameters Ψ and Δ, which are defined by

$$\frac{r_p}{r_s} = \tan(\Psi)\exp(i\Delta) \tag{9.4}$$

where r_p and r_s are the Fresnel reflection coefficients that can be calculated if the thickness and the refractive indices of each layer of the multi-layered thin film are known. If some of these information are unknown, an initial guess is given to calculate the ratio of the two reflection coefficients and then the result is compared to the measured data. Any unknown parameters can be varied until a best match is found. The estimator of this match is the Mean Squared Error (MSE), which indicates the difference of the calculated data and the measured data.

To obtain a maximal difference of the two reflection coefficients, the incident angle θ is chosen around the Brewster angle of the sample to minimise the value of r_p. To improve the accuracy of measurements, more than one angle can be measured. For spectroscopic ellipsometry, the ellipsometry parameters are obtained as functions of wavelength. The spectra properties of the sample can be obtained simultaneously. After the ellipsometry parameters are measured, one needs to specify a model in the software of the ellipsometer (CompleteEASE, J. A. Woollam) to calculate the ellipsometry parameters. The model used for the transparent thin film (silicon dioxide or LB films) in this work is shown in Fig. 9.13, where the Cauchy film represents the transparent film and its refractive index is given by

$$n(\lambda) = A + B/\lambda^2 + C/\lambda^4 \tag{9.5}$$

where λ is the wavelength, A, B, C are the unknown parameters. The native oxide layer has a typically thickness of 1.5 nm. Upon fitting the calculated data and the measured data, the thickness and the refractive index of the Cauchy film can be obtained simultaneously. Note that the trivial birefringence of the LB films made of stearic acid was neglected in this work [157].

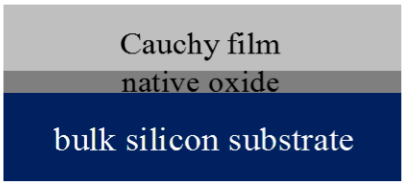

Figure 9.13: Model structure in ellipsometry measurements.

9.3.2 Film thickness and refractive index results

This section shows the thickness and refractive index results measured from VASE.

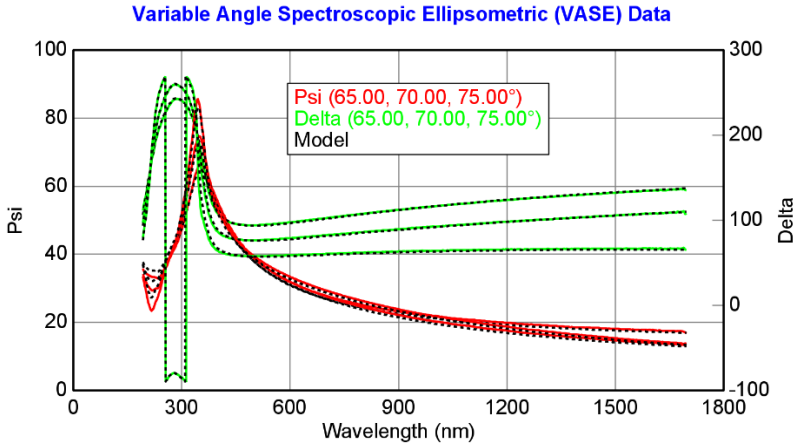

Figure 9.14: VASE result of 26 SA monolayers on silicon substrate.

Figure 9.14 shows a typical VASE measurement result of 26 SA monolayers deposited on a silicon substrate. The ellipsometry parameters Ψ (Psi in figure) and Δ (Delta in figure) were measured at three angles (65, 70 and 75 degrees), and they all fitted well (MSE=24) with the data calculated from the model specified in Fig. 9.13. The thickness and the refractive index of the LB film can be extracted from the ellipsometer software CompleteEASE.

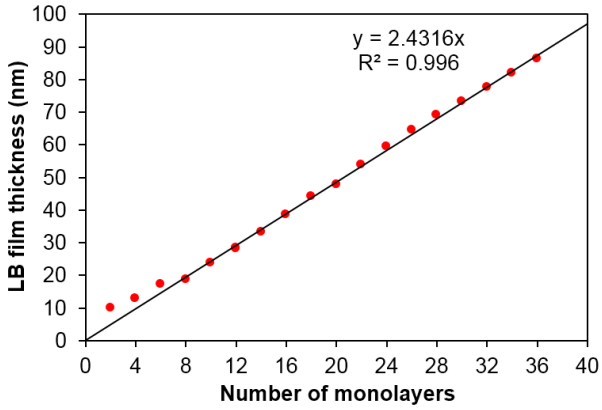

Figure 9.15: Dependence of LB film thickness on the number of monolayers.

Figure 9.15 shows the dependence of the thickness of pure SA LB film on the number of monolayers it consists. It is seen that a linear fit can be obtained and the thickness of a monolayer can be estimated to be 2.43 nm, which is close to literature [157]. The mismatch at smaller number of monolayers is due to the uncertainty of ellipsometry measurements for ultrathin films.

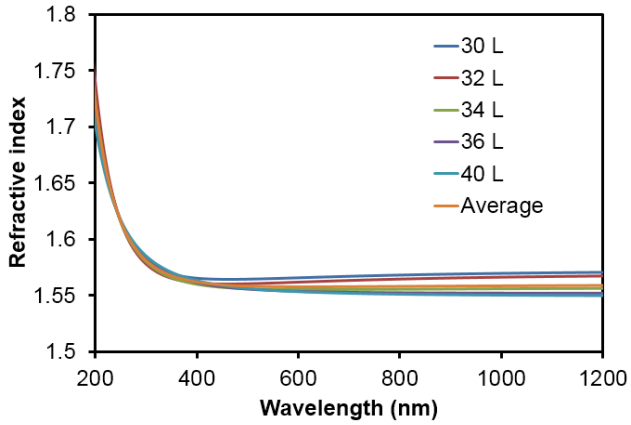

Figure 9.16: Refractive index for SA LB film with different number of LB layers.

Figure 9.16 shows the measured refractive index of the LB films consist of different number of monolayers. It is seen that the measured result is nearly identical regardless of the number of monolayers. This consistence indicates good quality of the deposited LB films. An averaged value was used in modelling.

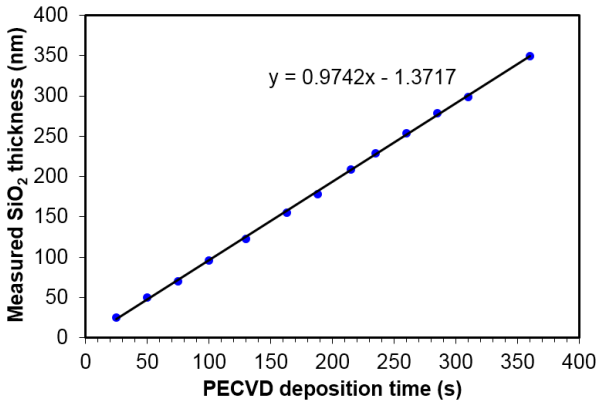

Figure 9.17: Silicon dioxide thickness dependence on the deposition time of PECVD.

The thickness and refractive index of the silicon oxide films deposited on silicon substrates were also measured by ellipsometry. Figure 9.17 shows the dependence of the silicon oxide thickness on the deposition time by PECVD. A linear fit was obtained and the deposition rate was close to the nominal rate of 1 nm/s.

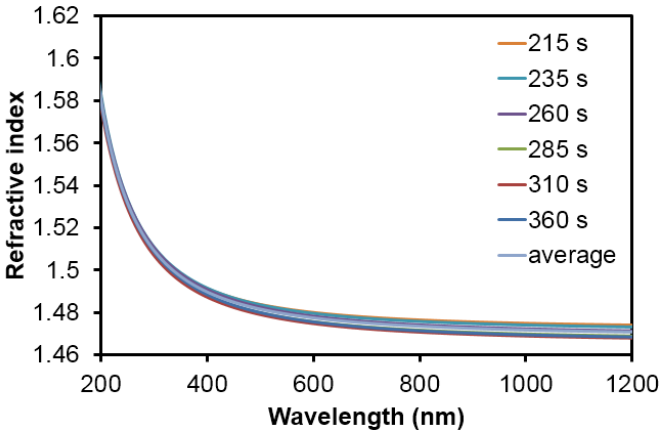

Figure 9.18: Refractive index of silicon dioxide films deposited by PECVD.

The refractive index of the silicon oxide films were plotted in Fig. 9.18. It is shown that the measured refractive index has no dependence on the thickness of the silicon dioxide film.

9.4 Fluorescence lifetime and emission spectrum measurement

The fluorescence lifetime and emission spectrum were measured via the Time Correlated Single Photon Counting (TCSPC) technique by using a PicoQuant FluoTime 200 fluorescence lifetime spectrometer.

9.4.1 Time correlated single photon counting technique

The fluorescence lifetime of organic fluorescent molecules are typically in the order of a few nanoseconds. A direct measure of fluorescence decay is difficult due to the fast decay of fluorescence emission. An alternative way to record fast decays is to use periodic excitations and extend the data collection time to multiple cycles. The TCSPC technique use periodic

excitations and precisely register the arriving time of the fluorescence photons. Then a histogram can be built to recovery the fluorescence decay curve.

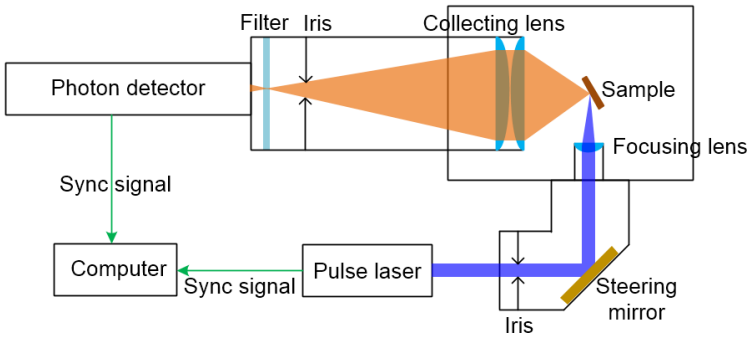

Figure 9.19: Setup of FluoTime 200 fluorescence lifetime spectrometer [160].

The optical setup of the FluoTime 200 system is shown in Fig. 9.19. The light source is a diode laser emitting at the wavelength of 485 nm and with repetition rate of 40 MHz. In a typical fluorescence measurement, the steering mirror is used to adjust the laser beam to directly impinge on the fluorescent molecules deposited on the sample. Then the fluorescent photons are collected by a high numerical aperture collecting lens, and guided to the photon detector equipped with a monochromator, after passing through a long-pass edge filter (Chroma HQ510LP). The photon detector then syncs the arrival time of the fluorescent photon to the precision time electronics board installed on the computer. The computer registers the arriving time of 10000 photons and produces the histogram for the fluorescence decay. Via fitting the histogram with exponential functions, the fluorescence lifetime can be obtained. In classical chemical kinetics, the fluorescence decay is a simple exponential function given by

$$F(t) = F_0 e^{-\frac{t}{\tau}} \tag{9.6}$$

where F_0 is the light intensity at $t = 0$, and τ is the fluorescence lifetime. This is an idealised fluorescence decay when the excitation light is infinitely narrow. However, in practice the laser source has a finite temporal width of 50 picoseconds, and the photon detector also has a temporal response function. So the measured fluorescence decay is the convolution of the idealised decay curve, the excitation light profile and the response function of the detecting system. The influence of the latter two factors can be obtained by measure the scattering decay curve of the pulsed laser at the excitation wavelength. This decay curve is defined as the instrument response function (IRF) and the measured decay curve can be expressed as [158]

$$I(t) = \int_{-\infty}^{t} F(t-t')IRF(t')dt' \tag{9.7}$$

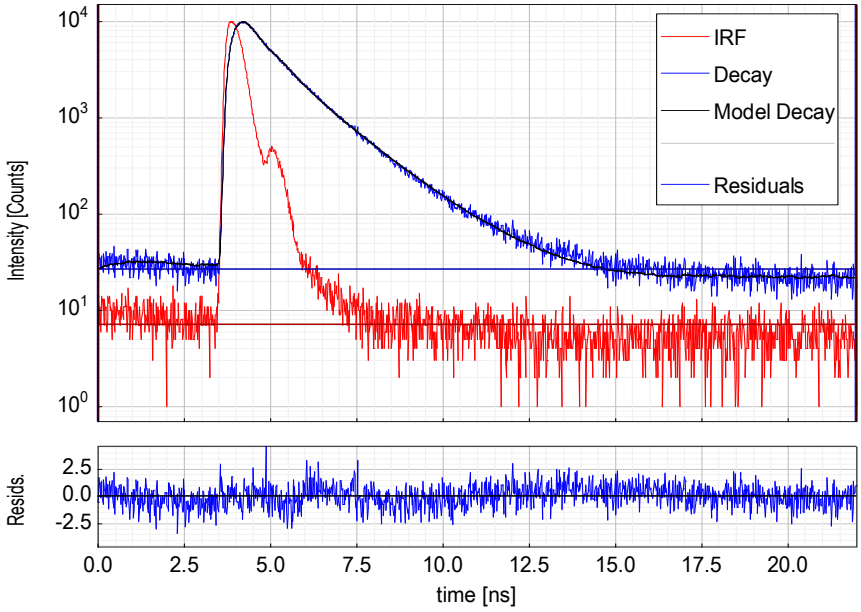

Figure 9.20: Typical measured fluorescence decay and IRF curves.

Figure 9.20 shows typical results of measured fluorescence decay and IRF curves for a bilayer of DiI molecules deposited on the surface of a silicon substrate. The bottom figure shows the residues, which indicates the degree of mismatch between the measured decay and the model given by Eq. (9.7). We found that the best fit can be obtained if the decay curve is given by the sum of two exponential functions for the DiI molecules we used

$$F(t) = A_1 e^{-\frac{t}{\tau_1}} + A_2 e^{-\frac{t}{\tau_2}} \tag{9.8}$$

where $A_i, i = 1,2$ are the amplitudes at $t = 0$, $\tau_i, i = 1,2$ the two lifetimes. Addition of a third lifetime component in Eq. (9.8) resulted in no improvement of the fitting. However, here two lifetimes do not indicate that there were two emitting species in the LB films. This phenomenon for DiI molecules has also been observed in [161], and the possible reason were complex chemical processes such as energy-level heterogeneities and excited state reactions. As suggested by [161], this work uses the intensity averaged lifetime which is given by [158]

$$\langle \tau \rangle = \frac{\int_0^\infty t\left(A_1 e^{-\frac{t}{\tau_1}} + A_2 e^{-\frac{t}{\tau_2}}\right) dt}{\int_0^\infty \left(A_1 e^{-\frac{t}{\tau_1}} + A_2 e^{-\frac{t}{\tau_2}}\right) dt} = \frac{A_1\tau_1^2 + A_2\tau_2^2}{A_1\tau_1 + A_2\tau_2} \tag{9.9}$$

9.4.2 Time resolved emission spectrum

The time resolved emission spectrum (TRES) was also measured by the FluoTime 200 system. The system first recorded the fluorescence decay curves at different wavelength (540-700 nm

with a 2 nm step), but over an identical time interval (3 seconds) which is much longer than the fluorescence lifetime. Then the TRES was constructed by summing up all the photons detected at the respected wavelength. Such fluorescence spectrum is equivalent to steady state fluorescence spectrum [126], [127].

9.5 Results and discussion

DiI molecules were deposited at different distance to the surface of glass (used as reference), copper, bulk silicon and ultrathin silicon film to study the dependence of fluorescence near various surfaces. This section summarise the experimental results and comparison with modelling results.

9.5.1 Sputtered copper substrates

Figure 9.21 (a) shows the structure of the samples deposited on copper substrate, while Fig. 9.21 (b) shows that for the glass substrate. For all the samples, the DiI doped bilayer was cover with a pure bilayer of SA. The refractive index of the glass substrate is close to that of the LB films, so the optical environment of the DiI molecules deposited on the glass substrate can be approximated to be homogeneous and the measured lifetime is used as the unquenched lifetime τ_0. Note that the top air-SA interface only has a limited influence to the fluorescence lifetime especially for the molecules emitting as HEDs [118]. The DiI molecules were found out to be emitting as HEDs and the top air-SA interface was not considered in the modelling. Another assumption in modelling is that the DiI molecules are emitting in the middle of the bilayer.

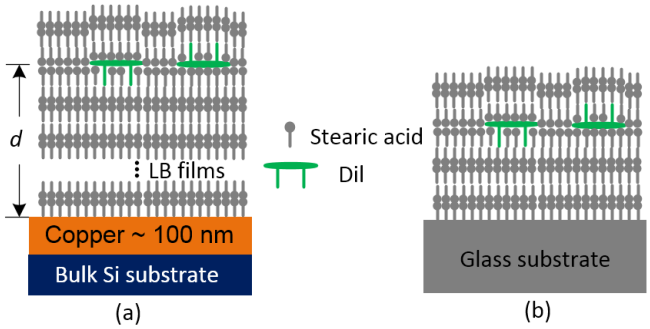

Figure 9.21: Structure of copper sample and glass sample.

The dependence of the measured lifetimes of DiI bilayer on the distance to the copper surface were fitted with the CPS model (Eq. (7.4) and Eq. (7.5)) for different orientation of dipole configurations shown in Fig. 9.22. Upon fitting the fluorescence lifetime in the absence of the copper substrate τ_0 and the quantum yield q can be obtained. It is shown in Fig. 9.22 that the measured lifetimes can fit with the modelling results for either an isotropic (ISO) orientation

configuration of dipole or a HED for the DiI-copper distance beyond 20 nm. But the attempt to fit with the modelling results for a VED was failed.

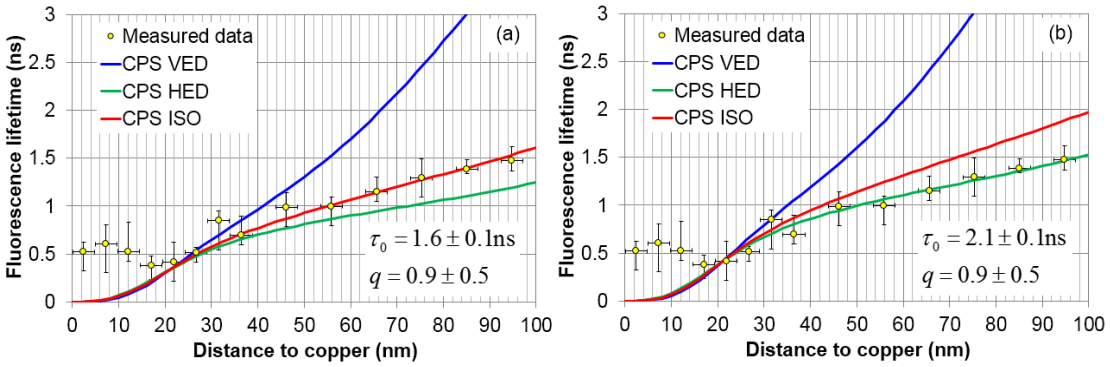

Figure 9.22: Comparison of measured lifetime and modelling data of (a) an isotropic and (b) a horizontal dipole.

However, the result of τ_0 given by the HED fitting is closer to the measured lifetime from the samples using glass as substrates. Identical values for τ_0 and q were also obtained by fitting the measured data from the bulk silicon samples with the related modelling results for a HED. These results indicate that the excited DiI molecules are damping as HEDs and all the following modelling results are for a HED orientation.

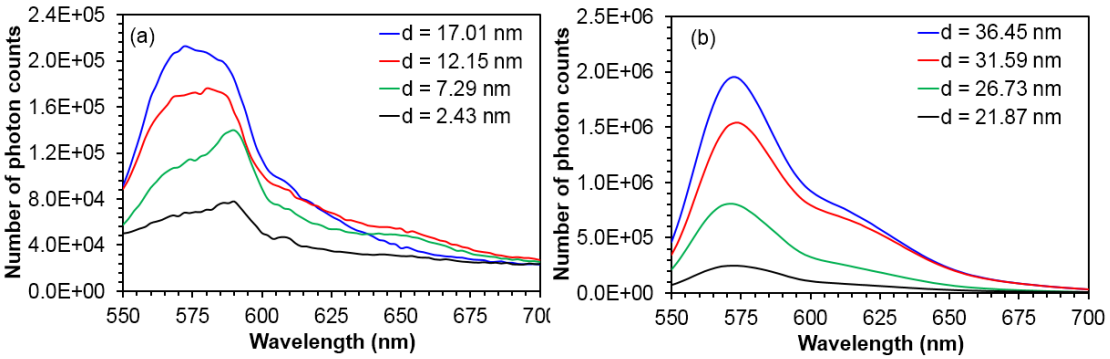

Figure 9.23: TRES measured from copper samples.

The TRES spectra were also recorded and selected results are shown in Fig. 9.23. It is seen that the number of photon counts, or fluoresence intensity, decreases as the distance to the copper mirror reduces, which signifies larger probability of energy transfer to the copper mirror. In comparison with the spectra shown in Fig. 9.23 (b) which resemble the steady state spectrum of DiI in chroloform shown in Fig. 9.9, the spectra shown in Fig. 9.23 (a) are partly distorted. This is possibly because of the strong interaction between the excited DiI molecules and the surface plasmons supported by the copper substrate at close distance range [162]. This interaction might be the reason for the discrepancy between the measured fluorescence lifetime results and the modelling results for DiI-copper distance below 20 nm shown in Fig. 9.22. Note that the

experimental resutls obtained by Drexhage also did not show enough data points below 20 nm [114]. More work is needed to understand the interactions at this close distance range.

9.5.2 Bulk silicon substrates

DiI bilayers were also deposited at different distance to the surface of bulk silicon substrates. For short distance pure SA LB films were used as spacer, while for large distance SiO_2 films deposited by PECVD were used as spacer. The reason for not using SA LB film for large distance is that the surface area of the LB trough used in experiments is small and a long time is needed to deposit thick LB films. The structure of these two kinds of samples are shown in Fig. 9.24.

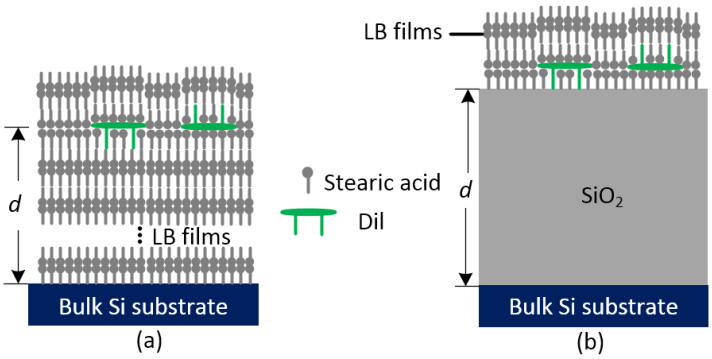

Figure 9.24: Structure of bulk silicon samples with (a) SA as spacer and (b) SiO_2 as spacer.

The power dissipated by the excited molecules near a bulk silicon substrate can be distinguished into three channels: fluorescence in the far field ($k_\rho < k_{SA}$), photon tunnelling into silicon ($k_{SA} < k_\rho < k_{Si}$), and light harvesting in the near field ($k_\rho > k_{Si}$). By integrating the power spectrum given by Eq. (7.9) in related wavenumber intervals, the damping rates in these power dissipation channels can be obtained and the result for a HED damping at different distance to a bulk silicon substrate is shown in Fig. 9.25.

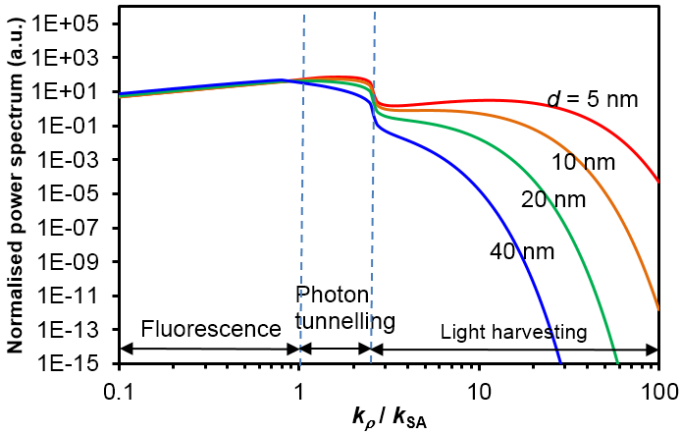

Figure 9.25: Power spectrum of a HED emitting near a bulk silicon substrate.

It is shown in Fig. 9.25 that the power dissipated via light harvesting changes significantly as the distance decreases. However, as shown in Fig. 7.8 the contribution of power dissipated in this channel is limited when the distance of DiI-silicon increase: for distance larger than 10 nm, the contribution of light harvesting is less than 7%. So in the following analysis light harvesting is neglected.

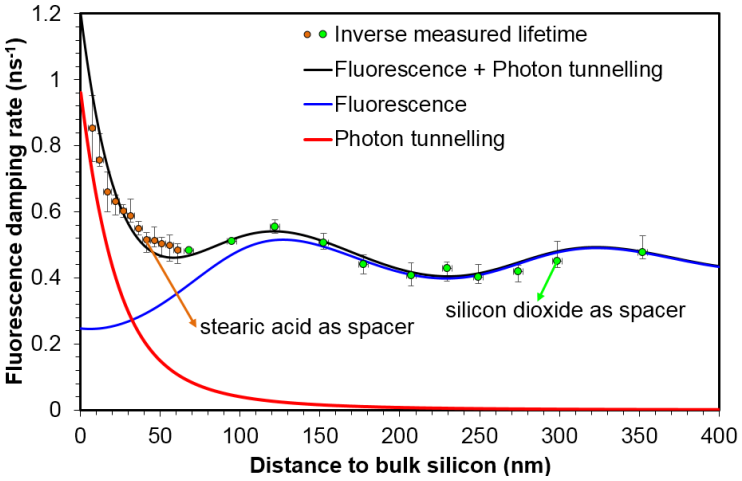

Figure 9.26: Fluorescence damping rate near the bulk silicon substrate.

Figure 9.26 compares the measured fluorescence lifetime from the bulk silicon samples with the modelling results, which is the sum of the effects of fluorescence and photon tunnelling. It is seen that for the distance beyond 200 nm, the effect of fluorescence is sufficient to describe the behaviour of the measured lifetime data. While below this distance, photon tunnelling becomes dominated and the sum of these two effects fits well with the experimental data. Note that at very short distance below 20 nm, the measured lifetime results have large error bars. Possibly, this is due to the surface roughness of the substrates. In addition to fluorescence lifetime, TRES spectra from the bulk silicon samples were also recorded and shown in Fig. 9.27.

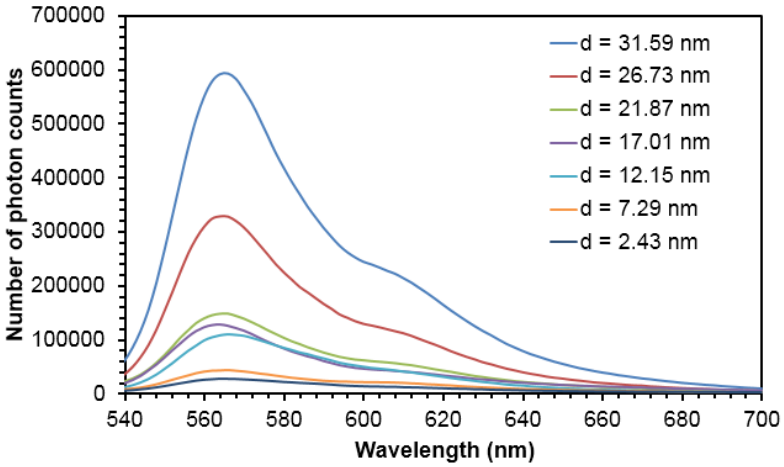

Figure 9.27: TRES measured from bulk silicon samples.

This is due to that at such distance range, the dominent power dissipation channel is photon tunnelling. As indicated by the modelling results shown in Fig. 7.8, the photon tunnelling rate increases as the distance reduces. This result signifies energy transfer to the silicon substrates via photon tunnelling. Spectra distortion at close distance, which were observed for the copper samples, were not observed for the silicon samples. Similar TRES results has also been measured from the ultrathin silicon samples.

9.5.3 Ultrathin silicon substrates

The structure of the LB films deposited on the SOI based ultrathin silicon films is shown in Fig. 9.27. All the spacer layers were pure SA LB films.

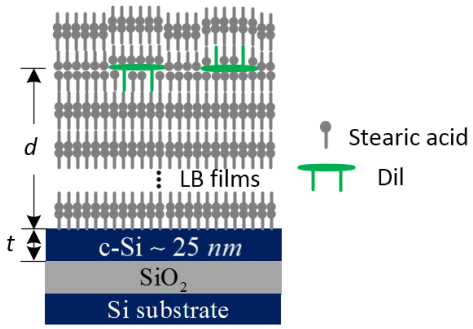

Figure 9.28: Structure of the ultrathin silicon samples.

For the 25 nm thick active silicon layer, only a single TE waveguide mode can be supported at the wavelength of 565 nm. The power spectrum of a HED emitting at this wavelength at the distance of 20 nm to the thin silicon film is shown in Fig. 9.29. It is shown that in the wavenumber range, which corresponds to photon tunnelling, a distinct peak exist. We found that this peak corresponds to the resonance frequency of the single TE mode supported by the thin silicon film. Here the distance of 20 nm is chosen randomly and at other distance the power spectrum also has a single peak at identical location in the photon tunnelling region.

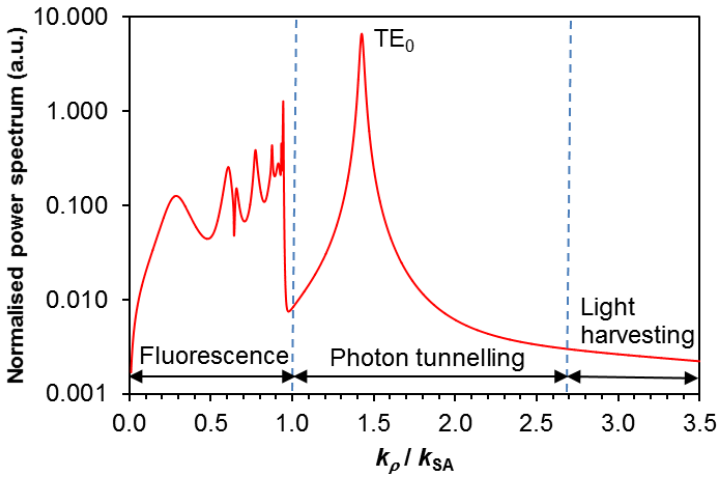

Figure 9.29: Power spectrum of a HED emitting near the 25 nm thick silicon film.

The photon tunnelling rate into such a thin silicon film can be simplified from Eq. (8.22) and given by a single exponential function in the form of

$$\gamma_t \approx \frac{3\pi}{2k_1}\frac{|k_{1x}|\left(k_2^2-k_1^2-|k_{1xm}|^2\right)}{\left(k_2^2-k_1^2\right)\left(t|k_{1x}|+2\right)}\exp(-2|k_{1x}|d) \tag{9.10}$$

where k_1 and k_2 are the wavenumber of photon in SA and silicon, respectively, k_{1x} the vertical wavenumber component related to the single TE waveguide mode and t the thickness of the active silicon layer. The numerical value of this photon tunnelling rate was calculated and combined with the contribution of fluorescence to compare with the measured lifetime results in Fig. 9.30.

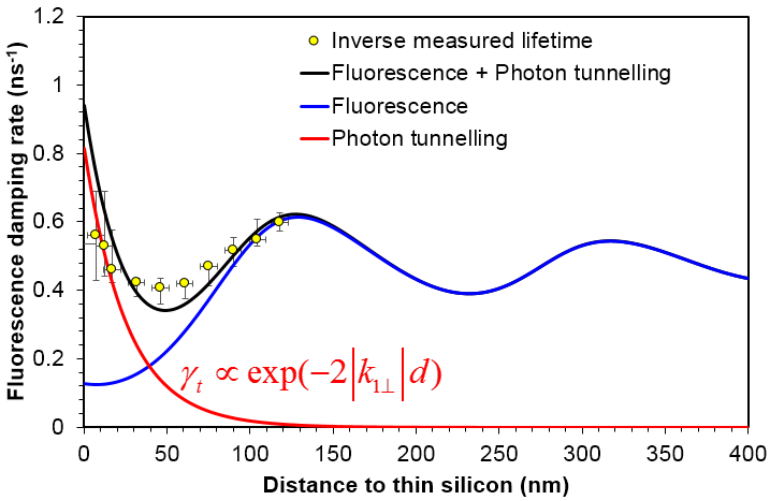

Figure 9.30: Fluorescence damping rate near the 25 nm thick silicon film.

It is seen from Fig. 9.30 that the measured lifetimes fit well with the modelling results which combines the effect of fluorescence and photon tunnelling. The mismatch at close distance below 20 nm is possibly due to the relative large uncertainty (25±5 nm) of the thickness of the active silicon layer. To study the effect of the uncertainty of the thickness of the ultrathin silicon film, the measured lifetime results were compared to the modelling results (fluorescence plus photon tunnelling) for three different thicknesses of silicon film in Fig. 9.31.

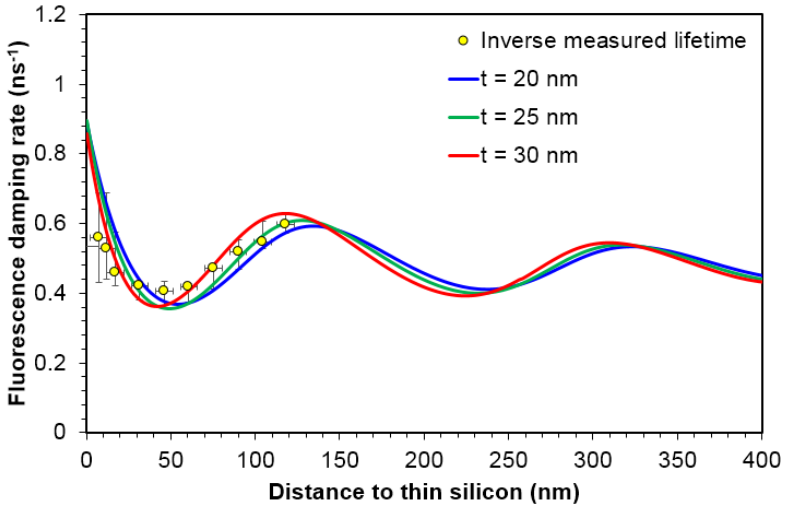

Figure 9.31: Fluorescence damping rate dependence on ultrathin silicon film thickness.

It is seen from Fig. 9.31 that the measured results locate within the modelling results for a 20 nm and a 30 nm thick thin silicon film. This indicates good match between the model and experiments. For the distance below 20 nm, the measured results have large error bars, similar to the results obtained from bulk silicon samples. The possible reason for this is again the surface roughness of the thin silicon film.

9.6 Conclusion

This chapter summarises the experimental procedures and results of studying fluorescence and energy transfer of excited dye molecules near glass, metal, bulk silicon and ultrathin silicon films via the techniques of Langmuir-Blodgettry, variable angle spectroscopic ellipsometry and time-correlated single photon counting. The measured fluorescence lifetime results were compared to the photon tunnelling model described in Chapter 8, which shows good agreement. These results show that the excited fluorescent molecules were effectively damping as HEDs and energy transfer to ultrathin silicon films were by injection of waveguide modes. It is shown that light absorption in thin silicon solar cells could be enhanced by proximal fluorescent molecules via coupling solar radiation to the trapped waveguide modes in the solar cell which works as a waveguide.

Chapter 10 Conclusion and Future Work

10.1 Conclusions

The principal aim of this work is to use fluorescent molecules to harness photon transport in planar solar converters to enhance the photoexcitation rate in crystalline silicon solar cells. Solar radiation absorbed by fluorescent molecules can be coupled to the trapped waveguide modes either by the far field radiation of the excited molecules in fluorescent solar collectors, or by direct energy transfer to a proximal silicon solar cell via the evanescent waves in the near field. These two approaches use either smaller area or thinner silicon solar cells and bear substantial potential for low cost and high efficiency photovoltaic applications.

Chapter 2 has reviewed the key optical concepts for this work: evanescent waves, photon tunnelling and waveguide modes. It has been shown that energy transfer from excited fluorescent molecules to a proximal thin silicon solar cell is analogous to photon tunnelling through an air gap between two prisms at an incident angle greater than the critical angle for total internal reflection. And the tunnelled photons are trapped in the thin silicon solar cell as waveguide modes. Thus fluorescent molecules are good candidates to enhance light absorption in thin silicon solar cells.

Chapter 3 has reviewed light source for solar cells, i.e. solar radiation and molecular fluorescence. The typical structure and the theoretical efficiency limits of idealised single junction solar cells have also been reviewed. An analytical model for the internal quantum efficiency of an abrupt junction silicon solar cell has been reviewed and it shows good agreement with the industry software PC1D. Simulation results show that several hundreds of micrometres thick of silicon material is needed for a commercial bulk crystalline silicon solar cell to achieve an efficiency over 15%. Thus reducing the usage of silicon materials is an effective approach to bring down the cost of crystalline silicon solar cells.

The development of FSCs has been reviewed in Chapter 4, including modern versions based on zeolites, dye alignment and photonic structures. Several models for FSC have been reviewed, including the models by Weber and Lambe, Batchelder and Zewail, Markvart and Chatten. The spectral reabsorption probability was introduced in the model of Markvart and this quantity was characterised by an analytical expression based on Beer-Lambert's law in Chapter 5. This model was able to predict the spectra of edge fluorescence emission of fluorescent solar collectors and the modelling results have shown good agreement with experiments. In the limit of high reabsorption, this model has given a useful simple expression for the reabsorption probability

limit, which only depends on the étendue of the emitted photon flux, the absorption coefficient of the dye molecules, and the refractive index of the matrix of the collector.

Chapter 6 has demonstrated the analysis to link the abnormal quantum efficiency of a 200 nm thick crystalline silicon solar cell to the waveguide modes supported by this solar cell. This analysis has studied the poles of the solar cell absorbance in the complex plane of wavenumber. And we have found that the peaks of the quantum efficiency of the solar cell lie close to the resonance frequency of the waveguide modes propagating near the critical angles for total internal reflection. The normally inaccessible feature of the waveguide modes to external observation can thus be detected in external quantum response, in terms of the poles of the absorbance of the thin silicon solar cell, in the complex wavenumber plane.

Chapter 7 has reviewed fluorescence and energy transfer near metal, dielectric and semiconducting interfaces and their application to the enhancement of solar cell performance. It has been shown that molecular fluorescence near various metals have been studied intensively and the experimental results fit well with the pure classical model developed by CPS. While less work has been done for semiconductors and much emphasis was on the Förster-type resonance energy transfer process, which is the dominate effect for molecular-semiconductor distance below 20 nm. It has been shown that the reported experimental results in literature divert from the CPS model at this short distance range.

For the distance in the order of the wavelength of light, energy transfer by photon tunnelling has been demonstrated firstly by metal nanoparticle enhanced solar cells. However, due to the parasitic absorption loss and expensive fabrication processes of the metal nanoparticles, this approach still needs further improvements.

Preliminary theoretical calculation results have shown that fluorescent molecules are good candidates to replace metal nanoparticles. Practical problems such as intermolecular energy transfer have been discussed and novel systems such as zeolites have been suggested to combine with fluorescent molecules to enhance light absorption in silicon solar cells.

Chapter 8 has shown the derivation processes of the photon tunnelling rate from a vertical or horizontal electric dipole to a nearby thin waveguide via a complex variable analysis. The analytical expression for the photon tunnelling rate is given by a summation of a few exponential functions, and each of them corresponds to one of the waveguide modes supported by the underlying thin waveguide. It has been shown that this expression fits well with the exact model given by CPS and represents a useful tool to study the dependence of energy transfer probability on the thickness of thin silicon films. Numerical calculation of this expression has shown that

this energy transfer process is efficient: the energy transfer probability is larger than 70% even when the underlying crystalline silicon film is merely 25 nm thick.

Chapter 9 has summarised the experimental details and results of studying fluorescence and energy transfer of a carbocyanine dye near glass, metal, bulk silicon and 25 nm thick silicon films via the techniques of Langmuir-Blodgettry, variable angle spectroscopic ellipsometry and time-correlated single photon counting. The measured fluorescence lifetime results have been compared with the photon tunnelling model described in Chapter 8, which shows good agreement. These results has shown that the excited carbocyanine dye molecules were effectively damping as horizontal electric dipoles and efficient energy transfer to the 25 nm thick silicon film was by photon tunnelling to the single transverse electric waveguide mode supported by the thin silicon film.

10.2 Future work

Future work for this project would be combining the effects of light harvesting in the near field and photon tunnelling via the evanescent waves to build a high efficiency ultrathin crystalline silicon solar cell.

This would involve the investigation of molecular fluorescence at close distance, i.e. below 10 nm, to the surface of thin crystalline silicon films. At this distance range, light harvesting via the near field of the molecular dipole radiation dominates the power damped by the molecular dipoles. This non-radiative energy transfer process bears the promise to promote interband electronic transitions without strict momentum conservation in indirect bandgap materials such as crystalline silicon and has attracted significant interests in photovoltaic applications recently [163]–[167].

Quantum mechanical calculation in [163], [165] shows that the absorption rate of the near filed of the molecular dipole radiation is proportional to $(\hbar\omega - E_g)^{1/2}$, where $\hbar\omega$ is the photon energy and E_g the bandgap energy of crystalline silicon. While the result in [164] indicates that this rate is proportional to $(\hbar\omega - E_g)$. However, all these work are theoretical results and have not verified by experiments.

Future experimental work could be studying the dependence of energy transfer rate on the distance to crystalline silicon using the atomic layer deposition technique [168]. The advantage of using this technique is that atomic level thickness, i.e. a few angstroms, of ultrathin films such as silicon dioxide can be deposited as spacer layers between the fluorescent molecules and crystalline silicon. Thus more data points of fluorescent lifetimes can be obtained at close

distance range. Via comparing with the CPS model the complex dielectric constant of crystalline silicon, which characterise the response to the near field radiation of the molecular dipoles at close distance range, can be obtained [131] and the results could be used to verify the theoretical models described in [163]–[165].

List of References

[1] W. H. Weber and J. Lambe, “Luminescent greenhouse collector for solar radiation,” *Appl. Opt.*, vol. 15, no. 10, pp. 2299–2300, 1976.

[2] W. G. Van Sark, K. W. Barnham, L. H. Slooff, A. J. Chatten, A. Büchtemann, A. Meyer, S. J. Mc.Cormack, R. Koole, D. J. Farrell, R. Bose, E. E. Bende, A. R. Burgers, T. Budel, J. Quilitz, M. Kennedy, T. Meyer, S. H. Wadman, G. P. van Klink, G. van Koten, A. Meijerink, and D. Vanmaekelbergh, “Luminescent Solar Concentrators - a review of recent results,” *Opt. Express*, vol. 16, no. 26, pp. 21773–21792, 2008.

[3] M. G. Debije and P. P. C. Verbunt, “Thirty years of luminescent solar concentrator research: solar energy for the built Environment,” *Adv. Energy Mater.*, vol. 2, no. 1, pp. 12–35, 2012.

[4] T. Markvart, L. Danos, L. Fang, T. Parel, and N. Soleimani, “Photon frequency management for trapping & concentration of sunlight,” *RSC Adv.*, vol. 2, no. 8, pp. 3173–3179, 2012.

[5] B. S. Richards, A. Shalav, and R. P. Corkish, “A low escape-cone-loss luminescent solar concentrator,” in *Proc. of 19th Eur. Photovolt. Sol. Energy Conf.*, p. 113, 2004.

[6] T. Markvart, “Detailed balance method for ideal single-stage fluorescent collectors,” *J. Appl. Phys.*, vol. 99, no. 2, p. 26101, 2006.

[7] N. Alderman, L. Danos, L. Fang, T. Parel, and T. Markvart, “Enhancing light capture by silicon - with the help of molecules,” in *Proc. 40th IEEE Photovolt. Spec. Conf.*, 2014.

[8] J. C. Bose, “On the influence of the thickness of air-space on total reflection of electric radiation,” *Proc. R. Soc. London*, vol. 62, no. 1, pp. 300–310, 1897.

[9] B. J. Soller, H. R. Stuart, and D. G. Hall, “Energy transfer at optical frequencies to silicon-on-insulator structures,” *Opt. Lett.*, vol. 26, no. 18, p. 1421, 2001.

[10] B. J. Soller and D. G. Hall, “Energy transfer at optical frequencies to silicon-based waveguiding structures.,” *J. Opt. Soc. Am. A*, vol. 18, no. 10, pp. 2577–84, 2001.

[11] M. Born and E. Wolf, *Principles of Optics: Electromagnetic Theory of Propagation, Interference and Diffraction of Light*. Cambridge University Press, 2000.

[12] P. Yeh, *Optical Waves in Layered Media*. Wiley, 2005.

[13] W. L. Barnes, “Fluorescence near interfaces: The role of photonic mode density,” *J. Mod. Opt.*, vol. 45, no. 4, pp. 661–699, 1998.

[14] J. A. Kong, *Electromagnetic Wave Theory*. Cambridge, Massachusetts, USA: EMW Publishing, 2008.

[15] A. Sommerfeld, *Partial Differential Equations in Physics.* New York: Academic Press, 1949.

[16] M. A. Green, "Self-consistent optical parameters of intrinsic silicon at 300K including temperature coefficients," *Sol. Energy Mater. Sol. Cells*, vol. 92, no. 11, pp. 1305–1310, 2008.

[17] R. Zhu, S., Yu, A. W., Hawley, D., Roy, "Frustrated total internal reflection: a demonstration and review," *Am. J. Phys.*, vol. 54, no. 7, p. 601, 1986.

[18] R. Eisberg and R. Resnick, *Quantum Physics of Atoms, Molecules, Solids, Nuclei, and Particles*. New York: Wiley, 1974.

[19] T. Markvart and L. Castaner, Eds., *Practical Handbook of Photovoltics: Fundamentals and Applications*. Elsevier, 2003.

[20] M. J. Adams, *An Introduction to Optical Waveguides*. New York: Wiley, 1981.

[21] R. T. Ross, "Some thermodynamics of photochemical systems," *J. Chem. Phys.*, vol. 46, no. 12, p. 4590, 1967.

[22] P. Würfel and W. Ruppel, "Upper limit of thermophotovoltaic solar energy conversion," *IEEE Trans. Electron Devices*, vol. 27, no. 4, pp. 745–750, 1980.

[23] T. J. J. Meyer and T. Markvart, "The chemical potential of light in fluorescent solar collectors," *J. Appl. Phys.*, vol. 105, no. 6, p. 63110, 2009.

[24] T. Markvart, *Solar Electricity*. Wiley, 2000.

[25] "AM0 Solar Spectrum." [Online]. Available: http://rredc.nrel.gov/solar/spectra/am0/.

[26] "AM1.5 Solar Spectrum." [Online]. Available: http://rredc.nrel.gov/solar/spectra/am1.5/.

[27] M. A. Green, *Solar Cells: Operating Principles, Technology, and System Applications*. Prentice-Hall, 1982.

[28] A. Goetzberger and V. Wittwer, "Fluorescent planar collector-concentrators: a review," *Sol. Cells*, vol. 4, no. 1, pp. 3–23, 1981.

[29] B. Valeur, *Molecular Fluorescence: Principles and Applications*. WILEY-VCH Verlag GmbH, 2001.

[30] M. Cohen and T. Bergstresser, "Band structures and pseudopotential form factors for fourteen semiconductors of the diamond and zinc-blende structures," *Phys. Rev.*, vol. 141, no. 2, pp. 789–796, 1966.

[31] M. A. Green and M. J. Keevers, "Optical properties of intrinsic silicon at 300 K," *Prog. Photovoltaics Res. Appl.*, vol. 3, no. 3, pp. 189–192, 1995.

[32] D. Trivich and P. A. Flinn, "Maximum efficiency of solar energy conversion by quantum processes," in *Solar Energy Research*, F. Daniels and J. Duffie, Eds. London: Thames and Hudson, pp. 143–147., 1955.

[33] W. Shockley and H. J. Queisser, “Detailed balance limit of efficiency of p-n junction solar cells,” *J. Appl. Phys.*, vol. 32, no. 3, pp. 510–519, 1961.

[34] W. Ruppel and P. Würfel, “Upper limit for the conversion of solar energy,” *Electron Devices, IEEE Trans.*, vol. 27, no. 4, pp. 877–882, 1980.

[35] M. A. Green, K. Emery, Y. Hishikawa, W. Warta, and E. D. Dunlop, “Solar cell efficiency tables (version 43),” *Prog. Photovolt. Res. Appl.*, vol. 22, no. 1, pp. 1–9, 2014.

[36] A. De Vos, “Detailed balance limit of the efficiency of tandem solar cells,” *J. Phys. D. Appl. Phys.*, vol. 13, no. 5, p. 839, 1980.

[37] S. M. Sze and K. K. Ng, *Physics of Semiconductor Devices*. John Wiley & Sons, 2006.

[38] P. Kittidachachan, T. Markvart, D. M. Bagnall, R. Greef, and G. J. Ensell, “A detailed study of p–n junction solar cells by means of collection efficiency,” *Sol. Energy Mater. Sol. Cells*, vol. 91, no. 2–3, pp. 160–166, 2007.

[39] “Monocrystalline silicon solar cell module STP265S-20/Wd.” [Online]. Available: http://www.suntech-power.com/menu/monocrystalline.html.

[40] “Solar PV cost data.” [Online]. Available: https://www.gov.uk/government/publications/solar-pv-cost-data.

[41] “Annual domestic energy bills.” [Online]. Available: https://www.gov.uk/government/statistical-data-sets/annual-domestic-energy-price-statistics.

[42] J. A. Levitt and W. H. Weber, “Materials for luminescent greenhouse solar collectors,” *Appl. Opt.*, vol. 16, no. 10, pp. 2684–2689, 1977.

[43] L. H. Slooff, E. E. Bende, A. R. Burgers, T. Budel, M. Pravettoni, R. P. Kenny, E. D. Dunlop, and A. Büchtemann, “A luminescent solar concentrator with 7.1% power conversion efficiency,” *Phys. status solidi – Rapid Res. Lett.*, vol. 2, no. 6, pp. 257–259, 2008.

[44] J. Goldschmidt, M. Peters, A. Bosch, H. Helmers, F. Dimroth, S. Glunz, and G. Willeke, “Increasing the efficiency of fluorescent concentrator systems,” *Sol. Energy Mater. Sol. Cells*, vol. 93, no. 2, pp. 176–182, 2009.

[45] L. Desmet, A. J. M. Ras, D. K. G. de Boer, and M. G. Debije, “Monocrystalline silicon photovoltaic luminescent solar concentrator with 4.2% power conversion efficiency,” *Opt. Lett.*, vol. 37, no. 15, pp. 3087–3089, 2012.

[46] T. S. Parel, L. Danos, and T. Markvart, “Photon transport in fluorescent solar concentrators,” in *Proc. of 39th Photovolt. Spec. Conf.*, pp. 1761–1765, 2013.

[47] A. M. Hermann, “Luminescent solar concentrators - a review,” *Sol. Energy*, vol. 29, no. 4, pp. 323–329, 1982.

[48] A. H. Zewail and J. S. Batchelder, “Luminescent solar concentrators: an overview,” in *Polymers in Solar Energy Utilization*, vol. 220, American Chemical Society, pp. 331–352, 1983.

[49] G. Seybold and G. Wagenblast, “New perylene and violanthrone dyestuffs for fluorescent collectors,” *Dye. Pigment.*, vol. 11, no. 4, pp. 303–317, 1989.

[50] J. Bomm, A. Büchtemann, A. J. Chatten, R. Bose, D. J. Farrell, N. L. A. Chan, Y. Xiao, L. H. Slooff, T. Meyer, A. Meyer, W. G. J. H. M. van Sark, and R. Koole, “Fabrication and full characterization of state-of-the-art quantum dot luminescent solar concentrators,” *Sol. Energy Mater. Sol. Cells*, vol. 95, no. 8, pp. 2087–2094, 2011.

[51] G. Katsagounos, E. Stathatos, N. B. Arabatzis, A. D. Keramidas, and P. Lianos, “Enhanced photon harvesting in silicon multicrystalline solar cells by new lanthanide complexes as light concentrators,” *J. Lumin.*, vol. 131, no. 8, pp. 1776–1781, 2011.

[52] M. Peters, J. C. Goldschmidt, P. Löper, B. Groß, J. Üpping, F. Dimroth, R. Wehrspohn, and B. Bläsi, “Spectrally-selective photonic structures for PV applications,” *Energies*, vol. 3, no. 2, pp. 171–193, 2010.

[53] P. P. C. Verbunt, C. W. M. Bastiaansen, D. J. Broer, and M. G. Debije, “The effect of dyes aligned by liquid crystals on luminescent solar concentrator performance,” in *Proc. of 24th Eur. Photovolt. Sol. Energy Conf.*, pp. 381–384, 2009.

[54] G. Calzaferri, “Nanochannels: hosts for the supramolecular organization of molecules and complexes,” *Langmuir*, vol. 28, no. 15, pp. 6216–6231, 2012.

[55] P. Kittidachachan, L. Danos, T. J. J. Meyer, N. Alderman, and T. Markvart, “Photon collection efficiency of fluorescent solar collectors,” *Chim.*, vol. 61, no. 12, pp. 780–786, 2007.

[56] B. A. Swartz, T. Cole, and A. H. Zewail, “Photon trapping and energy transfer in multiple-dye plastic matrices: an efficient solar-energy concentrator,” *Opt. Lett.*, vol. 1, no. 2, pp. 73–75, 1977.

[57] W. R. L. Thomas, J. M. Drake, and M. L. Lesiecki, “Light transport in planar luminescent solar concentrators: the role of matrix losses,” *Appl. Opt.*, vol. 22, no. 21, pp. 3440–3450, 1983.

[58] L. Fang, T. S. Parel, L. Danos, and T. Markvart, “Photon reabsorption in fluorescent solar collectors,” *J. Appl. Phys.*, vol. 111, no. 7, pp. 76103–76104, 2012.

[59] V. M. Granchak, T. V Sakhno, and S. Y. Kuchmy, “Light-emitting materials – active components of luminescent solar concentrators,” *Theor. Exp. Chem.*, vol. 50, no. 1, pp. 1–20, 2014.

[60] R. Kinderman, L. H. Slooff, A. R. Burgers, N. J. Bakker, A. Buchtemann, R. Danz, and J. A. M. van Roosmalen, “I-V performance and stability study of dyes for luminescent plate concentrators,” *J. Sol. Energy Eng.*, vol. 129, no. 3, pp. 277–282, 2007.

[61] L. H. Slooff, N. J. Bakker, P. M. Sommeling, A. Büchtemann, A. Wedel, and W. G. J. H. M. van Sark, "Long-term optical stability of fluorescent solar concentrator plates," *Phys. status solidi A*, vol. 211, no. 5, pp. 1150–1154, 2014.

[62] L. J. Andrews, B. C. McCollum, and A. Lempicki, "Luminescent solar collectors based on fluorescent glasses," *J. Lumin.*, vol. 24–25, no. 2, pp. 877–880, 1981.

[63] R. Reisfeld and Y. Kalisky, "Nd^{3+} and Yb^{3+} germanate and tellurite glasses for fluorescent solar energy collectors," *Chem. Phys. Lett.*, vol. 80, no. 1, pp. 178–183, 1981.

[64] R. Reisfeld, "Future technological applications of rare-earth-doped materials," *J. Less Common Met.*, vol. 93, no. 2, pp. 243–251, 1983.

[65] R. F. Kubin and A. N. Fletcher, "Fluorescence quantum yields of some rhodamine dyes," *J. Lumin.*, vol. 27, no. 4, pp. 455–462, 1982.

[66] J. M. Drake, M. L. Lesiecki, J. Sansregret, and W. R. L. Thomas, "Organic dyes in PMMA in a planar luminescent solar collector: a performance evaluation," *Appl. Opt.*, vol. 21, no. 16, pp. 2945–2952, 1982.

[67] M. L. Lesiecki and J. M. Drake, "Use of the thermal lens technique to measure the luminescent quantum yields of dyes in PMMA for luminescent solar concentrators," *Appl. Opt.*, vol. 21, no. 3, pp. 557–560, 1982.

[68] J. S. Batchelder, A. H. Zewail, and T. Cole, "Luminescent solar concentrators. 2: experimental and theoretical analysis of their possible efficiencies," *Appl. Opt.*, vol. 20, no. 21, pp. 3733–3754, 1981.

[69] L. R. Wilson and B. S. Richards, "Measurement method for photoluminescent quantum yields of fluorescent organic dyes in polymethyl methacrylate for luminescent solar concentrators," *Appl. Opt.*, vol. 48, no. 2, pp. 212–220, 2009.

[70] R. Reisfeld and C. Jørgensen, "Luminescent solar concentrators for energy conversion," in *Sol. Energy Mater.*, vol. 49, pp. 1–36, 1982.

[71] E. G. Moore, A. P. S. Samuel, and K. N. Raymond, "From antenna to assay: lessons learned in lanthanide luminescence," *Acc. Chem. Res.*, vol. 42, no. 4, pp. 542–552, 2009.

[72] O. Moudam, B. C. Rowan, M. Alamiry, P. Richardson, B. S. Richards, A. C. Jones, and N. Robertson, "Europium complexes with high total photoluminescence quantum yields in solution and in PMMA," *Chem. Commun.*, no. 43, pp. 6649–6651, 2009.

[73] M. Bredol, T. Jüstel, and S. Gutzov, "Luminescence of sol–gel-derived silica doped with terbium-benzoate complex," *Opt. Mater.*, vol. 18, no. 3, pp. 337–341, 2001.

[74] P. Pizzol, J. Marques-Hueso, N. Robertson, I. Freris, L. Bellotto, T. J. J. Meyer, and B. S. Richards, "Optical properties of lanthanide dyes for spectral conversion encapsulated in porous silica nanoparticles," in *Proc. of SPIE*, vol. 8438, p. 84381C, 2012.

[75] G. V Shcherbatyuk, R. H. Inman, C. Wang, R. Winston, and S. Ghosh, "Viability of using near infrared PbS quantum dots as active materials in luminescent solar concentrators," *Appl. Phys. Lett.*, vol. 96, no. 19, p. 191901, 2010.

[76] A. Chatten, K. Barnham, B. Buxton, N. Ekins-Daukes, and M. Malik, "Quantum dot solar concentrators," *Semiconductors*, vol. 38, no. 8, pp. 909–917, 2004.

[77] A. J. Chatten, K. W. J. Barnham, B. F. Buxton, N. J. Ekins-Daukes, and M. A. Malik, "A new approach to modelling quantum dot concentrators," *Sol. Energy Mater. Sol. Cells*, vol. 75, no. 3–4, pp. 363–371, 2003.

[78] K. Barnham, J. L. Marques, J. Hassard, and P. O'Brien, "Quantum-dot concentrator and thermodynamic model for the global redshift," *Appl. Phys. Lett.*, vol. 76, no. 9, pp. 1197–1199, 2000.

[79] C. S. Erickson, L. R. Bradshaw, S. McDowall, J. D. Gilbertson, D. R. Gamelin, and D. L. Patrick, "Zero-reabsorption doped-nanocrystal luminescent solar concentrators.," *ACS Nano*, vol. 8, no. 4, pp 3461–3467, 2014.

[80] A. Goetzberger, "Fluorescent solar energy collectors: operating conditions with diffuse light," *Appl. Phys. A Mater. Sci. Process.*, vol. 16, no. 4, pp. 399–404, 1978.

[81] C. F. Rapp and N. L. Boling, "Luminescent solar concentrators," in *Proc. of 13th IEEE Photovolt. Spec. Conf.*, pp. 690–693, 1978.

[82] R. Reisfeld, M. Eyal, V. Chernyak, and R. Zusman, "Luminescent solar concentrators based on thin films of polymethylmethacrylate on a polymethylmethacrylate support," *Sol. Energy Mater.*, vol. 17, no. 6, pp. 439–455, 1988.

[83] R. Reisfeld, V. Chernyak, M. Eyal, and C. K. Jorgensen, "Photostable fluorescent glass films for solar concentrators," in *Proc. of SPIE*, vol. 1727, pp. 299–305, 1992.

[84] A. Zastrow, "Physikalische analyse der energievelustmechanismen im fluoreszenzkollektor," PhD thesis, Universität Freiburg, Freiburg, 1981.

[85] R. Bose, D. J. Farrell, A. J. Chatten, M. Pravettoni, A. Büchtemann, and K. W. J. Barnham, "Novel configurations of luminescent solar concentrators," in *Proc. of 22nd Eur. Photovolt. Sol. Energy Conf.*, pp. 210–214, 2007.

[86] S. T. Bailey, G. E. Lokey, M. S. Hanes, J. D. M. Shearer, J. B. McLafferty, G. T. Beaumont, T. T. Baseler, J. M. Layhue, D. R. Broussard, Y.-Z. Zhang, and B. P. Wittmershaus, "Optimized excitation energy transfer in a three-dye luminescent solar concentrator," *Sol. Energy Mater. Sol. Cells*, vol. 91, no. 1, pp. 67–75, 2007.

[87] M. Peters, J. C. Goldschmidt, P. Löper, B. Bläsi, and A. Gombert, "The effect of photonic structures on the light guiding efficiency of fluorescent concentrators," *J. Appl. Phys.*, vol. 105, no. 1, p. 14909, 2009.

[88] J. C. Goldschmidt, M. Peters, J. Gutmann, L. Steidl, R. Zentel, B. Blasi, and M. Hermle, "Increasing fluorescent concentrator light collection efficiency by restricting the angular

emission characteristic of the incorporated luminescent material: the 'Nano-Fluko' concept," in *Proc. of SPIE*, vol. 7725, p. 77250S, 2010.

[89] J. S. Batchelder, A. H. Zewail, and T. Cole, "Luminescent solar concentrators. 1: theory of operation and techniques for performance evaluation," *Appl. Opt.*, vol. 18, no. 18, pp. 3090–3110, 1979.

[90] P. P. C. Verbunt, A. Kaiser, K. Hermans, C. W. M. Bastiaansen, D. J. Broer, and M. G. Debije, "Controlling light emission in luminescent solar concentrators through use of dye colecules aligned in a planar manner by liquid crystals," *Adv. Funct. Mater.*, vol. 19, no. 17, pp. 2714–2719, 2009.

[91] S. McDowall, B. L. Johnson, and D. L. Patrick, "Simulations of luminescent solar concentrators: effects of polarization and fluorophore alignment," *J. Appl. Phys.*, vol. 108, no. 5, p. 53508, 2010.

[92] C. L. Mulder, P. D. Reusswig, A. M. Velázquez, H. Kim, C. Rotschild, and M. A. Baldo, "Dye alignment in luminescent solar concentrators: I. vertical alignment for improved waveguide coupling," *Opt. Express*, vol. 18, no. S1, pp. A79–A90, 2010.

[93] C. L. Mulder, P. D. Reusswig, A. P. Beyler, H. Kim, C. Rotschild, and M. A. Baldo, "Dye alignment in luminescent solar concentrators: II. horizontal alignment for energy harvesting in linear polarizers," *Opt. Express*, vol. 18, no. S1, pp. A91–A99, 2010.

[94] R. W. MacQueen and T. W. Schmidt, "Molecular polarization switching for improved light coupling in luminescent solar concentrators," *J. Phys. Chem. Lett.*, vol. 4, no. 17, pp. 2874–2879, 2013.

[95] A. J. Chatten, D. Farrel, C. Jermyn, P. Thomas, B. F. Buxton, A. Buchtemann, R. Danz, and K. W. Barnham, "Thermodynamic modelling of luminescent solar concentrators," in *Proc. of 31st Photovolt. Spec. Conf.,* pp. 82–85, 2005.

[96] U. Rau, F. Einsele, and G. C. Glaeser, "Efficiency limits of photovoltaic fluorescent collectors," *Appl. Phys. Lett.*, vol. 87, no. 17, p. 171101, 2005.

[97] T. J. J. Meyer, J. Hlavaty, L. Smith, E. R. Freniere, and T. Markvart, "Ray racing techniques applied to the modelling of fluorescent solar collectors," in *Proc. of SPIE*, vol. 7211, p. 72110N, 2009.

[98] A. Kerrouche, D. A. Hardy, D. Ross, and B. S. Richards, "Luminescent solar concentrators: From experimental validation of 3D ray-tracing simulations to coloured stained-glass windows for BIPV," *Sol. Energy Mater. Sol. Cells*, vol. 122, pp. 99–106, 2014.

[99] O. von Roos, "Influence of radiative recombination on the minority-carrier transport in direct band-gap semiconductors," *J. Appl. Phys.*, vol. 54, no. 3, p. 1390, 1983.

[100] Y. B. Gigase, C. S. Harder, M. P. Kesler, H. P. Meier, and B. Van Zeghbroeck, "Threshold reduction through photon recycling in semiconductor lasers," *Appl. Phys. Lett.*, vol. 57, no. 13, p. 1310, 1990.

[101] H. De Neve, J. Blondelle, P. Van Daele, P. Demeester, R. Baets, and G. Borghs, "Recycling of guided mode light emission in planar microcavity light emitting diodes," *Appl. Phys. Lett.*, vol. 70, no. 7, p. 799, 1997.

[102] E. H. Kennard, "On The Thermodynamics of Fluorescence," *Phys. Rev.*, vol. 11, no. 1, p. 29, 1918.

[103] B. I. Stepanov, "A universal relation between the absorption and luminescence spectra of complex molecules," *Sov. Phys. Dokl.*, vol. 2, pp. 81–84, 1957.

[104] W. Van Roosbroeck and W. Shockley, "Photon-radiative recombination of electrons and holes in germanium," *Phys. Rev.*, vol. 94, no. 6, pp. 1558–1560, 1954.

[105] W. H. Weber and C. F. Eagen, "Energy transfer from an excited dye molecule to the surface plasmons of an adjacent metal," *Opt. Lett.*, vol. 4, no. 8, pp. 236–238, 1979.

[106] T. Markvart, "The thermodynamics of optical étendue," *J. Opt. A Pure Appl. Opt.*, vol. 10, no. 1, p. 15008, 2008.

[107] L. Danos, G. Jones, R. Greef, and T. Markvart, "Ultra-thin silicon solar cell: Modelling and characterisation," *Phys. status solidi A*, vol. 5, no. 5, pp. 1407–1410, 2008.

[108] J. Zhao, A. Wang, M. A. Green, and F. Ferrazza, "19.8% efficient 'honeycomb' textured multicrystalline and 24.4% monocrystalline silicon solar cells," *Appl. Phys. Lett.*, vol. 73, no. 14, p. 1991, 1998.

[109] H. R. Stuart and D. G. Hall, "Absorption enhancement in silicon-on-insulator waveguides using metal island films," *Appl. Phys. Lett.*, vol. 69, no. 16, pp. 2327–2329, 1996.

[110] T. Markvart, "Beyond the Yablonovitch limit: trapping light by frequency shift," *Appl. Phys. Lett.*, vol. 98, no. 7, p. 71107, 2011.

[111] M. T. Nimmo, L. M. Caillard, W. De Benedetti, H. M. Nguyen, O. Seitz, Y. N. Gartstein, Y. J. Chabal, and A. V Malko, "Visible to near-infrared sensitization of silicon substrates via energy transfer from proximal nanocrystals: further insights for hybrid photovoltaics.," *ACS Nano*, vol. 7, no. 4, pp. 3236–45, 2013.

[112] M. L. Brongersma, Y. Cui, and S. Fan, "Light management for photovoltaics using high-index nanostructures.," *Nat. Mater.*, vol. 13, no. 5, pp. 451–60, 2014.

[113] H. Kuhn, D. Möbius, and H. Bücher, "Spectroscopy of monolayer assemblies," in *Techniques of Chemistry, Vol. I, Physical Methods of Chemistry*, A. Weissberger and B. W. Rossiter, Eds. Wiley, pp. 577–702, 1972.

[114] K. H. Drexhage, "IV interaction of light with monomolecular dye layers," *Prog. Opt.*, vol. 12, pp. 163–232, 1974.

[115] K. H. Drexhage, "Influence of a dielectric interface on fluorescence decay time," *J. Lumin.*, vol. 1–2, pp. 693–701, 1970.

[116] K. H. Tews, “On the variation of luminescence lifetimes. The approximations of the approximative methods,” *J. Lumin.*, vol. 9, no. 3, pp. 223–239, 1974.

[117] H. Kuhn, “Classical aspects of energy transfer in molecular systems,” *J. Chem. Phys.*, vol. 53, no. 1, pp. 101–108, 1970.

[118] R. R. Chance, A. Prock, and R. Silbey, “Molecular fluorescence and energy transfer near interfaces,” in *Advances in Chemical Physics*, John Wiley & Sons, Inc., pp. 1–65, 1978.

[119] K. Joulain, R. Carminati, J.-P. Mulet, and J.-J. Greffet, “Definition and measurement of the local density of electromagnetic states close to an interface,” *Phys. Rev. B*, vol. 68, no. 24, p. 245405, 2003.

[120] L. Novotny and B. Hecht, *Principles of Nano-optics*. Cambridge University Press, 2006.

[121] G. W. Ford and W. H. Weber, “Electromagnetic interactions of molecules with metal surfaces,” *Phys. Rep.*, vol. 113, no. 4, pp. 195–287, 1984.

[122] W. Lukosz and R. E. Kunz, “Light emission by magnetic and electric dipoles close to a plane interface. I. Total radiated power,” *J. Opt. Soc. Am.*, vol. 67, no. 12, pp. 1607–1615, 1977.

[123] E. D. Palik, *Handbook of Optical Constants for Solids*. New York: Academic Press, 1985.

[124] W. R. Holland and D. G. Hall, “Waveguide mode enhancement of molecular fluorescence,” *Opt. Lett.*, vol. 10, no. 8, pp. 414–416, 1985.

[125] K. G. Sullivan, O. King, C. Sigg, and D. G. Hall, “Directional, enhanced fluorescence from molecules near a periodic surface,” *Appl. Opt.*, vol. 33, no. 13, pp. 2447–2454, 1994.

[126] L. Danos, R. Greef, and T. Markvart, “Efficient fluorescence quenching near crystalline silicon from Langmuir-Blodgett dye films,” *Thin Solid Films*, vol. 516, no. 20, pp. 7251–7255, 2008.

[127] L. Danos and T. Markvart, “Excitation energy transfer rate from Langmuir Blodgett (LB) dye monolayers to silicon: effect of aggregate formation,” *Chem. Phys. Lett.*, vol. 490, no. 4–6, pp. 194–199, 2010.

[128] D. L. Dexter, “Two ideas on energy transfer phenomena: Ion-pair effects involving the OH stretching mode, and sensitization of photovoltaic cells,” *J. Lumin.*, vol. 18–19, pp. 779–784, 1979.

[129] P. M. Whitmore, A. P. Alivisatos, and C. B. Harris, “Distance dependence of electronic energy transfer to semiconductor surfaces: $^{3}n\pi^{*}$ pyrazine/GaAs(110),” *Phys. Rev. Lett.*, vol. 50, no. 14, pp. 1092–1094, 1983.

[130] M. I. Sluch, A. G. Vitukhnovsky, and M. C. Petty, “Anomalous distance dependence of fluorescence lifetime quenched by a semiconductor,” *Phys. Lett. A*, vol. 200, no. 1, pp. 61–64, 1995.

[131] L. Danos and T. Markvart, “Efficient light harvesting with LB films for application in crystalline silicon solar cells,” in *MRS Proc.*, vol. 1120, 2009.

[132] T. Hayashi, T. G. Castner, and R. W. Boyd, "Quenching of molecular fluorescence near the surface of a semiconductor," *Chem. Phys. Lett.*, vol. 94, no. 5, pp. 461–466, 1983.

[133] R. J. Deri, "Interference effects on the photoluminescence intensity of molecules near a dielectric surface," *Chem. Phys. Lett.*, vol. 98, no. 5, pp. 485–490, 1983.

[134] M. Brandstätter, P. Fromherz, and A. Offenhäusser, "Fluorescent dye monolayers on oxidized silicon," *Thin Solid Films*, vol. 160, no. 1–2, pp. 341–346, 1988.

[135] A. Lambacher and P. Fromherz, "Fluorescence interference-contrast microscopy on oxidized silicon using a monomolecular dye layer," *Appl. Phys. A*, vol. 63, no. 3, pp. 207–216, 1996.

[136] A. P. Alivisatos, M. F. Arndt, S. Efrima, D. H. Waldeck, and C. B. Harris, "Electronic energy transfer at semiconductor interfaces. I. Energy transfer from two-dimensional molecular films to Si(111)," *J. Chem. Phys.*, vol. 86, no. 11, pp. 6540–6549, 1987.

[137] P. Andreakou, M. Brossard, M. Bernechea, G. Konstantatos, and P. Lagoudakis, "Resonance energy transfer from PbS colloidal quantum dots to bulk silicon: the road to hybrid photovoltaics," in *Proc. of SPIE*, vol. 8256, p. 82561L, 2012.

[138] H. R. Stuart and D. G. Hall, "Thermodynamic limit to light trapping in thin planar structures," *J. Opt. Soc. Am. A*, vol. 14, no. 11, pp. 3001–3008, 1997.

[139] S. Huber and G. Calzaferri, "Energy transfer from dye-zeolite L antenna crystals to bulk silicon.," *Chemphyschem*, vol. 5, no. 2, pp. 239–42, 2004.

[140] P. Rouard and A. Meessen, "Optical properties of thin metal films," *Prog. Opt.*, vol. 15, pp. 77–137, 1977.

[141] H. R. Stuart and D. G. Hall, "Enhanced dipole-dipole interaction between elementary radiators near a surface," *Phys. Rev. Lett.*, vol. 80, no. 25, pp. 5663–5666, 1998.

[142] D. M. Schaadt, B. Feng, and E. T. Yu, "Enhanced semiconductor optical absorption via surface plasmon excitation in metal nanoparticles," *Appl. Phys. Lett.*, vol. 86, no. 6, p. 063106, 2005.

[143] S. Pillai, K. R. Catchpole, T. Trupke, and M. A. Green, "Surface plasmon enhanced silicon solar cells," *J. Appl. Phys.*, vol. 101, no. 9, p. 093105, 2007.

[144] K. Nakayama, K. Tanabe, and H. A. Atwater, "Plasmonic nanoparticle enhanced light absorption in GaAs solar cells," *Appl. Phys. Lett.*, vol. 93, no. 12, p. 121904, 2008.

[145] N. P. Hylton, X. F. Li, V. Giannini, K.-H. Lee, N. J. Ekins-Daukes, J. Loo, D. Vercruysse, P. Van Dorpe, H. Sodabanlu, M. Sugiyama, and S. A. Maier, "Loss mitigation in plasmonic solar cells: aluminium nanoparticles for broadband photocurrent enhancements in GaAs photodiodes.," *Sci. Rep.*, vol. 3, p. 2874, 2013.

[146] D. Derkacs, S. H. Lim, P. Matheu, W. Mar, and E. T. Yu, "Improved performance of amorphous silicon solar cells via scattering from surface plasmon polaritons in nearby metallic nanoparticles," *Appl. Phys. Lett.*, vol. 89, no. 9, p. 093103, 2006.

[147] A. J. Morfa, K. L. Rowlen, T. H. Reilly, M. J. Romero, and J. van de Lagemaat, "Plasmon-enhanced solar energy conversion in organic bulk heterojunction photovoltaics," *Appl. Phys. Lett.*, vol. 92, no. 1, p. 013504, 2008.

[148] H. R. Stuart and D. G. Hall, "Island size effects in nanoparticle-enhanced photodetectors," *Appl. Phys. Lett.*, vol. 73, no. 26, p. 3815, 1998.

[149] H. A. Atwater and A. Polman, "Plasmonics for improved photovoltaic devices," *Nat. Mater.*, vol. 9, no. 3, pp. 205–213, 2010.

[150] M. A. Green and S. Pillai, "Harnessing plasmonics for solar cells," *Nat. Photonics*, vol. 6, no. 3, pp. 130–132, 2012.

[151] J. Grandidier, D. M. Callahan, J. N. Munday, and H. A. Atwater, "Gallium arsenide solar cell absorption enhancement using whispering gallery modes of dielectric nanospheres," *IEEE J. Photovolt.*, vol. 2, no. 2, pp. 123–128, 2012.

[152] J. Grandidier, R. A. Weitekamp, M. G. Deceglie, D. M. Callahan, C. Battaglia, C. R. Bukowsky, C. Ballif, R. H. Grubbs, and H. A. Atwater, "Solar cell efficiency enhancement via light trapping in printable resonant dielectric nanosphere arrays," *Phys. status solidi A*, vol. 210, no. 2, pp. 255–260, 2013.

[153] A. B. Matsko and V. S. Ilchenko, "Optical resonators with whispering-gallery modes-part I: basics," *IEEE J. Sel. Top. Quantum Electron.*, vol. 12, no. 1, pp. 3–14, 2006.

[154] H. M. Nguyen, O. Seitz, W. Peng, Y. N. Gartstein, Y. J. Chabal, and A. V Malko, "Efficient radiative and nonradiative energy transfer from proximal CdSe/ZnS nanocrystals into silicon nanomembranes," *ACS Nano*, vol. 6, no. 6, pp. 5574–5582, 2012.

[155] L. Fang, L. Danos, and T. Markvart, "Solar cell as a waveguide: quantum efficiency of an ultrathin crystalline silicon solar cell," in *Proc. of 28th Eur. Photovolt. Sol. Energy Conf.*, pp. 31–33, 2013.

[156] S. J. Riley, K.F., Hobson, P. and Bence, *Mathematical Methods for Physics and Engineering: A Comprehensive Guide*. Cambridge University Press, 2006.

[157] M. C. Petty, *Langmuir-Blodgett Films: An Introduction*. Cambridge University Press, 1996.

[158] J. R. Lakowicz, *Principles of Fluorescence Spectroscopy*. Springer, 2010.

[159] H. Fujiwara, *Spectroscopic Ellipsometry: Principles and Applications*. Wiley, 2007.

[160] "PicoQuant FluoTime 200 Modular Fluorescence Lifetime Spectrometer." [Online]. Available: http://www.picoquant.com/products/category/fluorescence-spectrometers/fluotime-200-modular-fluorescence-lifetime-spectrometer.

[161] B. S. Packard and D. E. Wolf, "Fluorescence lifetimes of carbocyanine lipid analogs in phospholipid bilayers," *Biochemistry*, vol. 24, no. 19, pp. 5176–5181, 1985.

[162] W. Holland and D. Hall, "Frequency shifts of an electric-dipole resonance near a conducting surface," *Phys. Rev. Lett.*, vol. 52, no. 12, pp. 1041–1044, 1984.

[163] M. Kirkengen, J. Bergli, and Y. M. Galperin, "Direct generation of charge carriers in c-Si solar cells due to embedded nanoparticles," *J. Appl. Phys.*, vol. 102, no. 9, p. 093713, 2007.

[164] J. Jacak, J. Krasnyj, W. Jacak, R. Gonczarek, A. Chepok, and L. Jacak, "Surface and volume plasmons in metallic nanospheres in a semiclassical RPA-type approach: near-field coupling of surface plasmons with the semiconductor substrate," *Phys. Rev. B*, vol. 82, no. 3, p. 035418, 2010.

[165] J. Jung, M. L. Trolle, K. Pedersen, and T. G. Pedersen, "Indirect near-field absorption mediated by localized surface plasmons," *Phys. Rev. B*, vol. 84, no. 16, p. 165447, 2011.

[166] M. L. Trolle and T. G. Pedersen, "Indirect optical absorption in silicon via thin-film surface plasmon," *J. Appl. Phys.*, vol. 112, no. 4, p. 043103, 2012.

[167] W. Jacak, A. Henrykowski, and K. Marszalski, "Plasmon enhanced photovoltaic effect in metallically nanomodified photocells," *Sol. Energy Mater. Sol. Cells*, vol. 117, pp. 663–666, 2013.

[168] S. M. George, "Atomic layer deposition: an overview.," *Chem. Rev.*, vol. 110, no. 1, pp. 111–31, 2010.